UNCLASSIFIED

SECURITY CLASSIFICATION OF THIS PAGE

REPORT DOCUMENTATION PAGE

1a. REPORT SECURITY CLASSIFICATION UNCLASSIFIED	1b. RESTRICTIVE MARKINGS
2a. SECURITY CLASSIFICATION AUTHORITY	3. DISTRIBUTION/AVAILABILITY OF REPORT Approved for Public Release; Distribution Unlimited
2b. DECLASSIFICATION/DOWNGRADING SCHEDULE	
4. PERFORMING ORGANIZATION REPORT NUMBER(S) R85-926546-20	5. MONITORING ORGANIZATION REPORT NUMBER(S) AFATL-TR-85-37
6a. NAME OF PERFORMING ORGANIZATION United Technologies Research Center 6b. OFFICE SYMBOL (If applicable)	7a. NAME OF MONITORING ORGANIZATION Air Force Armament Laboratory
6c. ADDRESS (City, State, and ZIP Code) Silver Lane East Hartford, Connecticut 06108	7b. ADDRESS (City, State, and ZIP Code) Eglin Air Force Base Florida, 32542-
8a. NAME OF FUNDING/SPONSORING ORGANIZATION Aeromechanics Division 8b. OFFICE SYMBOL (If applicable) AFATL/DLCM	9. PROCUREMENT INSTRUMENT IDENTIFICATION NUMBER F08635-83-C-0287
8c. ADDRESS (City, State, and ZIP Code) AFATL/DLCM Eglin AFB, FL	10. SOURCE OF FUNDING NUMBERS PROGRAM ELEMENT NO. 61101F; PROJECT NO. ILIR; TASK NO. 83; WORK UNIT ACCESSION NO 04

11. TITLE (Include Security Classification)

Composite Integral Response Sensing

12. PERSONAL AUTHOR(S)

J. R. Dunphy, G. Meltz and R. M. Elkow

13a. TYPE OF REPORT	13b. TIME COVERED	14. DATE OF REPORT (Year, Month, Day)	15. PAGE COUNT
Final Report	FROM Aug 82 TO Mar 85	September 1985	114

16. SUPPLEMENTARY NOTATION

Availability of this report is specified on verso of front cover.

17. COSATI CODES

FIELD	GROUP	SUB-GROUP
11	04	
13	13	

18. SUBJECT TERMS (Continue on reverse if necessary and identify by block number)

Fiber Optic Strain Gage,
Flight Control Systems
Distributed Strain Sensing

19. ABSTRACT (Continue on reverse if necessary and identify by block number)

This document describes the investigation of a new concept for measurement of distributed strain. Implementation of the technique utilizes a fiber optic device with twin, coupled cores, a single input and a single output. Multiple wavelength operation of the sensor yields a diagnosis of the waveguide coupling perturbations imposed by mechanical disturbances. A general theory for the device has been derived in the form of an integral equation that relates the sensor core contrast to an arbitrary bending strain or curvature. In many cases of interest the curvature is small and slowly varying. For these conditions theory shows that the core crosstalk spectrum is directly related to the Fourier

20. DISTRIBUTION/AVAILABILITY OF ABSTRACT ☒ UNCLASSIFIED/UNLIMITED ☒ SAME AS RPT. ☐ DTIC USERS	21. ABSTRACT SECURITY CLASSIFICATION UNCLASSIFIED
22a. NAME OF RESPONSIBLE INDIVIDUAL J. R. Cloutier	22b. TELEPHONE (Include Area Code) (904) 882-2961 — 22c. OFFICE SYMBOL AFATL/DLCM

DD FORM 1473, 84 MAR — 83 APR edition may be used until exhausted. All other editions are obsolete.

SECURITY CLASSIFICATION OF THIS PAGE

UNCLASSIFIED

19. ABSTRACT (Concluded)

transform of the strain distribution on a cantilevered beam. This result pertains to a wing with gradual bends (radius of curvature large compared to arc length) while stipulating very practical requirements on potential sensor parameters (radius of curvature large compared to device beatlength). Two computer models were developed from the theory. One model provides a rudimentary simulation of a wing with arbitrary loading (cantilevered beam). It was used to prove that the Fourier transformation of the simulated sensor output matched the bending moment distribution. The second model was developed to calculate the sensor response for comparison with the demonstration experiments. Fiber optic devices were designed and fabricated for laboratory-scale tests. Sensor performance was diagnosed by techniques established in direct support of these demonstrations. Verification experiments performed with simple bending perturbations in the laboratory apparatus confirmed the general form of the sensor spectra predicted by the model.

AFATL-TR-85-37

Composite Integral Response Sensing

J R Dunphy
G Meltz
R M Elkow

UNITED TECHNOLOGIES RESEARCH CENTER
SILVER LANE
EAST HARTFORD, CONNECTICUT 06108

SEPTEMBER 1985

FINAL REPORT FOR PERIOD AUGUST 1982 - MARCH 1985

Approved for public release; distribution unlimited

Air Force Armament Laboratory

AIR FORCE SYSTEMS COMMAND ★ UNITED STATES AIR FORCE ★ EGLIN AIR FORCE BASE, FLORIDA

NOTICE

When the Government drawings, specifications, or other data are used for any purpose other than in connection with a definitely related Government procurement operation, the United States Government thereby incurs no responsibility nor any obligation whatsoever; and the fact that the Government may have formulated, furnished, or in any way supplied the said drawings, specifications, or other data, is not to be regarded by implication or otherwise as in any manner licensing the holder or any other person or corporation, or conveying any rights or permission to manufacture, use, or sell any patented invention that may in any way be related thereto.

This report has been reviewed by the Public Affairs Office (PA) and is releasable to the National Technical Information Service (NTIS). At NTIS, it will be available to the general public, including foreign nations.

This technical report has been reviewed and is approved for publication.

FOR THE COMMANDER

Donald C Daniel
DONALD C. DANIEL
Chief, Aeromechanics Division

Even though this report may contain special release rights held by the controlling office, please do not request copies from the Air Force Armament Laboratory. If you qualify as a recipient, release approval will be obtained from the originating activity by DTIC. Address your request for additional copies to:

Defense Technical Information Center
Cameron Station
Alexandria, Virginia 22314

If your address has changed, if you wish to be removed from our mailing list, or if the addressee is no longer employed by your organization, please notify AFATL/DLCM, Eglin AFB FL 32542.

Copies of this report should not be returned unless return is required by security considerations, contractual obligations, or notice on a specific document.

PREFACE

This program was conducted by the United Technologies Research Center, Silver Lane, East Hartford Connecticut, 06108 under Contract F08635-83-C-0287 with the Air Force Armament Laboratory, Eglin Air Force Base, Florida 32542. James R. Cloutier (DLCM) managed the program for the Armament Laboratory. The program was conducted during the period from August 1982 to March 1985.

The Public Affairs Office has reviewed this report, and it is releasable to the National Technical Information Service (NTIS), where it will be available to the general public, including foreign nationals.

TABLE OF CONTENTS

LIST OF FIGURES

LIST OF FIGURES (CONTINUED)

LIST OF FIGURES (CONTINUED)

LIST OF FIGURES (CONCLUDED)

LIST OF TABLES

EXECUTIVE SUMMARY

This document describes the investigation of a new concept for measurement of distributed strain. Implementation of the technique utilizes a fiber optic device with twin, coupled cores, a single input and a single output. Multiple wavelength operation of the sensor yields a diagnosis of the waveguide coupling perturbations imposed by mechanical disturbances. A general theory for the device has been derived in the form of an integral equation that relates the sensor core contrast to an arbitrary bending strain or curvature. In many cases of interest the curvature is small and slowly varying. For these conditions theory shows that the core crosstalk spectrum is directly related to the Fourier transform of the strain distribution on a cantilevered beam. This result pertains to a wing with gradual bends (radius of curvature large compared to arc length) while stipulating very practical requirements on potential sensor parameters (radius of curvature large compared to device beatlength). Two computer models were developed from the theory. One model provides a rudimentary simulation of a wing with arbitrary loading (cantilevered beam). It was used to prove that the Fourier transformation of the simulated sensor output matched the bending moment distribution. The second model was developed to calculate the sensor response for comparison with the demonstration experiments. Fiber optic devices were designed and fabricated for laboratory-scale tests. Sensor performance was diagnosed by techniques established in direct support of these demonstrations. Verification experiments performed with simple bending perturbations in the laboratory apparatus confirmed the general form of the sensor spectra predicted by the model.

Both the theory and the experiments indicate that the twin-core device is highly sensitive to its mechanical environment and its operating conditions. This fiber optic sensor concept requires additional investigation and development to optimize device parameters for application to distributed strain diagnostics for airframe structures.

SECTION I

INTRODUCTION

This report describes a new type of fiber optic sensor for the measurement of distributed loads on composite components. Since the sensor ideally measures the bending moment distribution of the structure to which it is attached or embedded, a detailed decomposition of the load distribution could be potentially derived to yield the location and magnitude of isolated mechanical disturbances positioned at arbitrary points along its length.

The device consists of a single fiber optic filament containing two closely-spaced, crosstalking waveguides. An optical source with multiple wavelengths illuminates the single sensor input and a processing unit analyzes the signal from a detector unit that corresponds to the light emitted from the end of the sensor. This report identifies the processed sensor output as the Fourier Transform of the shear distribution imposed by the structural loading. When the sensor output is interpreted with knowledge of the structure's elastic properties, important parameters such as distributed strain or deflection become available.

The material and geometry of this new sensor are compatible with critical applications within composites. It can be as small as 0.002 inches in diameter and meters long, making it suitable for embedding in graphite/epoxy composite skins for large structures. Its small transverse dimension assures negligible void generation within the matrix material, while the high temperature constituents eliminate sensitivity to curing procedures. Finally, its dielectric characteristics promise to immunize the diagnostic function against electromagnetically induced noise.

Potential advantages to be derived from application of this new sensor are significant. For instance, such a sensor might be embedded within the wing of an aircraft with varying numbers and weights of stores (Figure 1). During operation, the flight dynamics of the aircraft may be altered by the load distribution on the wings. An automatic compensation scheme could be configured to place the aircraft's control surfaces in feedback loops that use the fiber sensor measurements, as well as other critical flight data, to derive correction factors for their adjustments. Realization of such an approach (Figure 2) would relieve the pilot of the need to correct for variable flight characteristics as stores are released or changed. Long term records of the fiber sensor measurements would also provide basic data on long term fatigue parameters relevant to the wings' structural strength. Finally, we anticipate a major advantage to result from the instrumented wings' ability to self-diagnose its response to new types of stores, providing allowable specification ranges for the modified requirements.

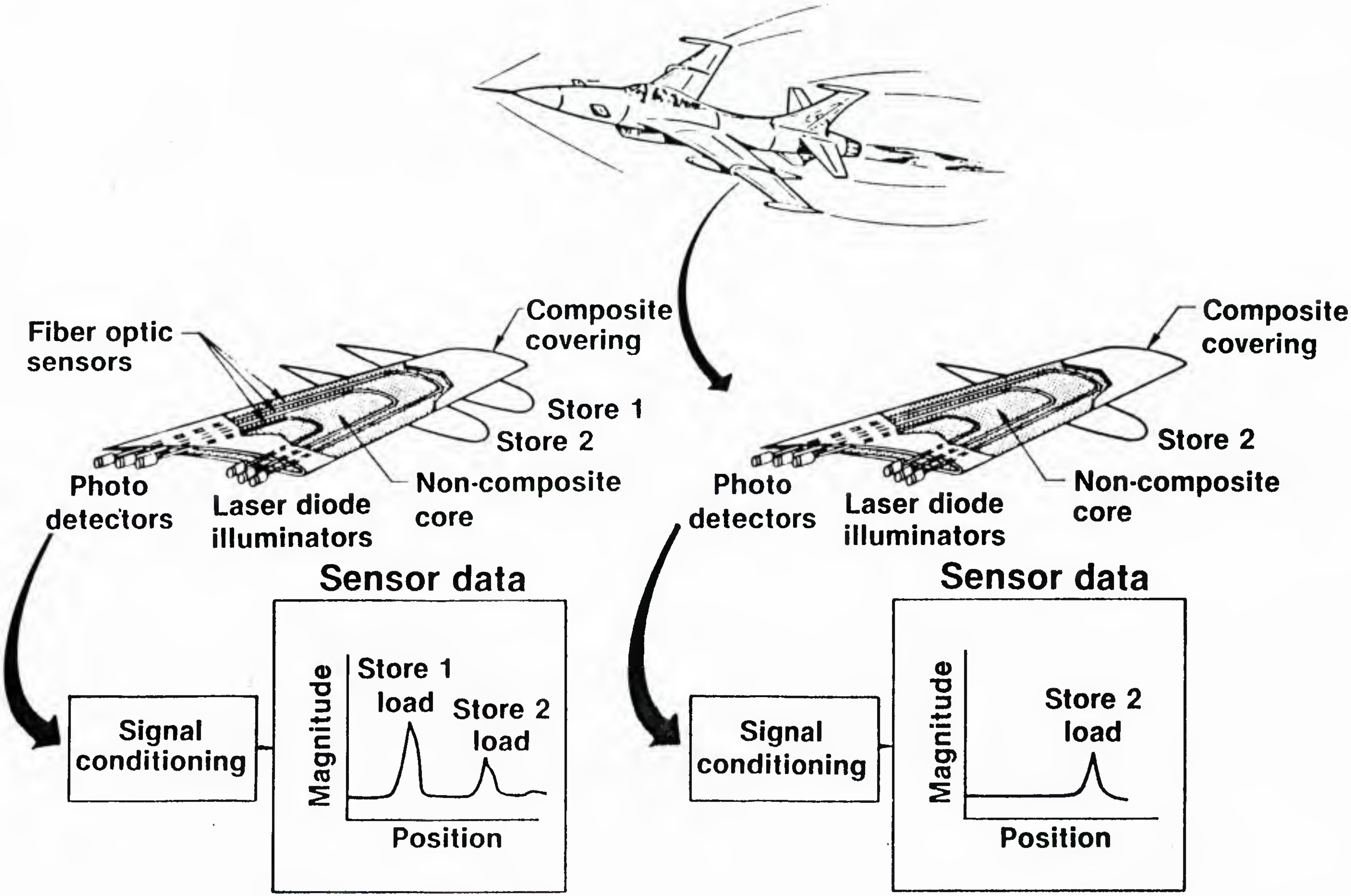

Figure 1. Wing Load Monitor

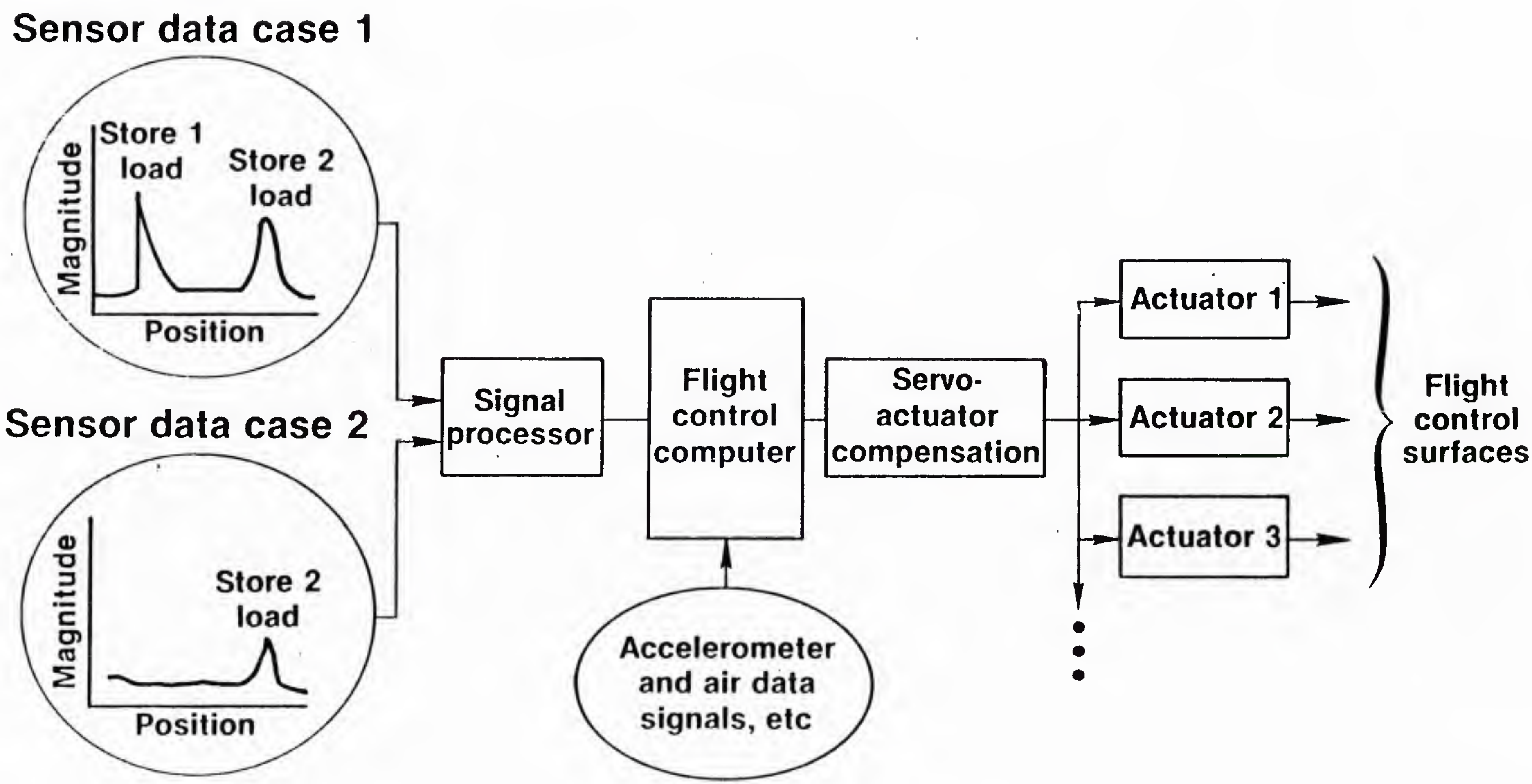

Figure 2. Wing Load Compensation

This report summarizes our investigations to model and to demonstrate the basic response of this promising device. The modelling proceeds from basic sensor/bend interaction to complex predictions for the entire output spectrum of the device attached to a cantilevered beam representation of a wing. On the other hand, the experimental work focuses on evaluation of sensor characteristics in simple and complex configurations implemented on small-scale laboratory bench apparatus. The goal of the measurements was to provide verification of the fundamental theoretical model. In our experiments the general form of the predicted spectra was confirmed. One important physical effect, polarization sensitivity, has not been included in the formulation and is suspected as the cause of complications during the benchmark experiments. Each issue and accomplishment is reviewed in the following text.

SECTION II

THEORETICAL DEVELOPMENT

1. INTRODUCTION

An optical waveguide formed from a pair of closely spaced, light-trapping cores in a common cladding (Figure 3) exhibits a phenomena known as crosstalk when the optical field in one core is coupled to the adjacent core (References 1, 2). This occurs because light energy is not totally confined within a core but extends to a small degree into the cladding and the adjacent core. When one core is illuminated, light couples back and forth between the cores as it propagates along the fiber. Complete energy exchange from the illuminated to the unilluminated core and back takes place in a beat length λ_b. The variation in intensity in each core with length L is a simple periodic function of the beat phase $\phi \equiv \pi L/\lambda_b$ (Figure 4). The beat phase will be a sensitive function of wavelength λ, varying nearly exponentially as the wavelength is changed. A crosstalk spectrum is generated by scanning the wavelength of the incident illumination and monitoring the light in either core.

The exchange of energy between cores in the twin-core fiber can be analyzed in terms of modal interference. To a very good approximation, the twin-core normal modes are linear combinations of the lowest order HE_{11} single core excitations. A normal mode, in this context, is that field distribution which retains its cross-sectional intensity pattern along the axis. There are four possible normal modes for this structure (Figure 5): two orthogonally polarized, symmetric and anti-symmetric pairs of HE_{11} modes. In this notation, HE_{11} is the lowest-order, fundamental-mode solution to the scalar wave equation for optical propagation in the twin-core geometry. Illumination of a single core is equivalent to the excitation of a pair of normal modes--a symmetric and anti-symmetric combination with the same polarization. Crosstalk is just the interference pattern between a pair of normal modes.

A curve or bend in the fiber in a plane containing the cores will couple the normal modes. Thus, a localized bending strain or deformation will generate crosstalk if both cores are illuminated by in-phase, equal amplitude light. In effect, the symmetric normal mode that is launched in the twin-core fiber is partly scattered by the bend into an antisymmetric combination with the same polarization. Crosstalk ensues beyond the bent section because the normal modes travel at slightly different velocities, leading to an interference pattern along the fiber or an apparent exchange of light from one core to the other. A change in wavelength slightly alters the propagation velocities of the modes, giving rise to a crosstalk spectrum in the core contrast.

Consider a twin-core fiber that is bent in a plane containing the cores. A bend in the orthogonal plane will not generate crosstalk. Let R be the radius of curvature of the midplane between the cores and ℓ the arclength along the center

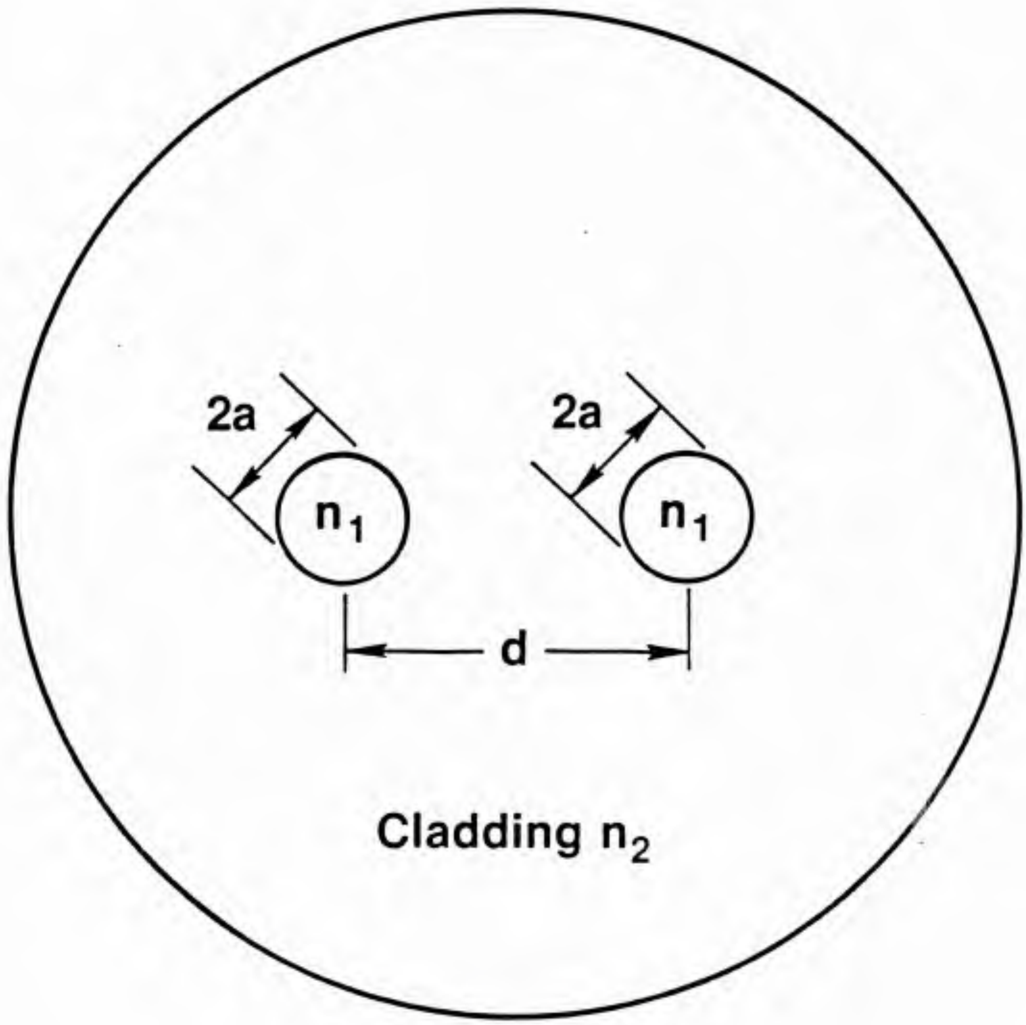

Figure 3. Cross Section of a Twin-Core Fiber-Optic Distributed Strain Sensor

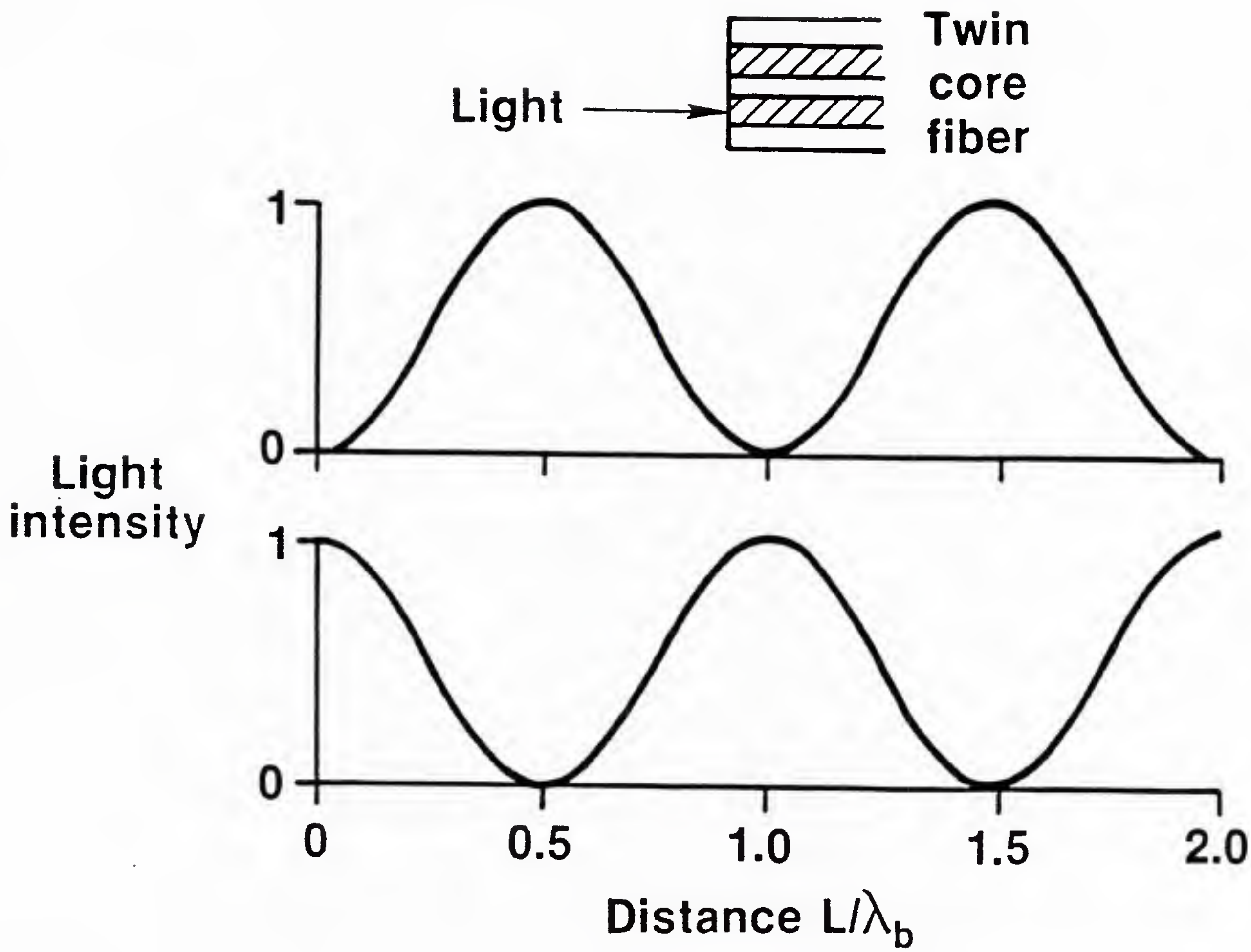

Figure 4. Crosstalk in a Twin-Core Fiber

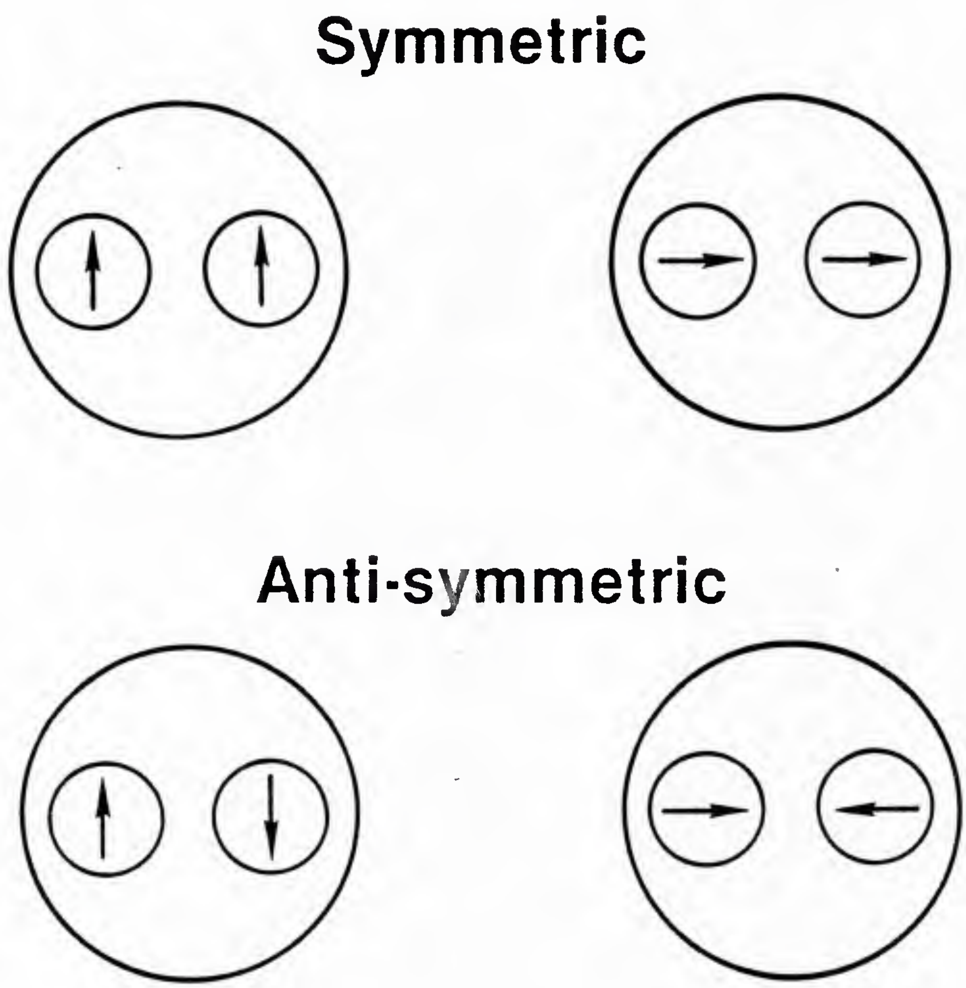

Figure 5. Lowest-Order Modes in a Twin-Core Fiber

line (see Figure 6). The fields in the fiber can be approximated (References 1, 3, 4) by a linear combination of the isolated, unperturbed HE_{11} modes in a straight fiber:

$$E = a_1(\ell)E_1 + a_2(\ell)E_2 \tag{1}$$

The amplitudes, a_1 and a_2, obey the following pair of coupled mode equations:

$$\frac{da_1}{d\ell} = -j(1-d/2R)(\pi/\lambda_b)a_2 - j\beta_o(1-d/2R)a_1 \tag{2}$$

$$\frac{da_2}{d\ell} = -j(1+d/2R)(\pi/\lambda_b)a_1 - j\beta_o(1+d/2R)a_2 \tag{3}$$

If we assume $d/2R \ll 1$, as is always the case, then the coupling coefficients $(1 \pm d/2R)\pi/\lambda_b$ become equal and power is conserved in the forward traveling modes. In the case of pure bending, that is if R is constant, the solution to Equations (8) and (9) can be expressed in the following matrix form (Reference 4):

$$\begin{pmatrix} a_1(\ell) \\ a_2(\ell) \end{pmatrix} = \begin{pmatrix} X & -jY \\ -jY & X^* \end{pmatrix} \begin{pmatrix} a_1(0) \\ a_2(0) \end{pmatrix} \tag{4}$$

where

$$X = \cos(K\ell) + j(\delta/K)\sin(K\ell) \tag{5}$$

$$Y = (\pi/\lambda_b)/K \sin(K\ell) \tag{6}$$

with

$$K = \sqrt{(\pi/\lambda_b)^2 + \delta^2} \tag{7}$$

and

$$\delta = \frac{2\pi}{\lambda} n_1(d/2R) \tag{8}$$

The transfer matrix for a series of pure bends and straight sections is obtained directly from Equation (4) by matrix multiplication.

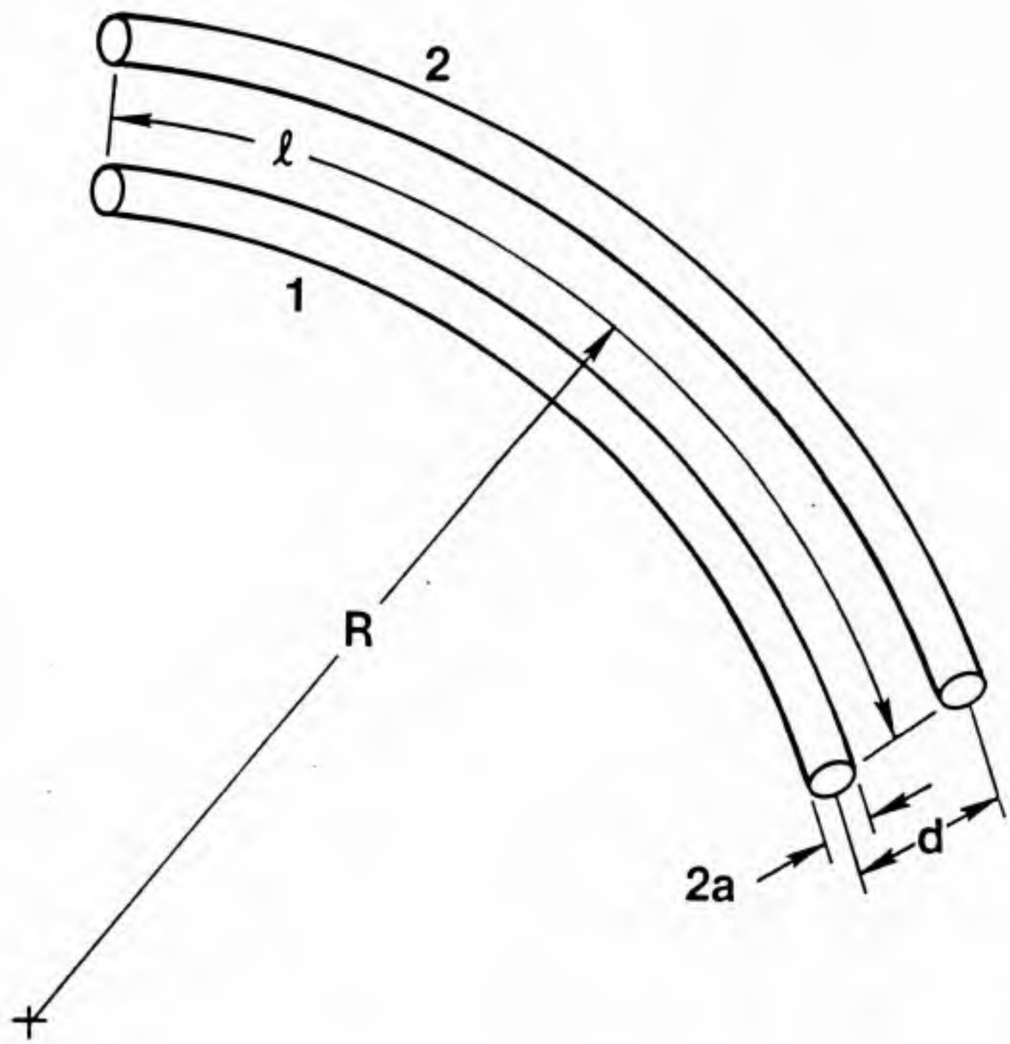

Figure 6. Curved Section of a Bent Twin-Core Fiber

In many cases of interest $\delta \ll \pi/\lambda_b$ and the transfer matrix T of a uniform bend reduces to

$$T = \begin{bmatrix} \cos(K\ell) & -j\sin(K\ell) \\ -j\sin(K\ell) & \cos(K\ell) \end{bmatrix} + j(\lambda_b/R_e)\sin(K\ell)\begin{bmatrix} 1 & 0 \\ 0 & -1 \end{bmatrix} \tag{9}$$

where R_e is an effective radius of curvature given by $R_e = R(\lambda/n_1 d)$. From Equation (9), we can analyze the effect of a bend on a normal mode. It can be seen that

$$T \cdot \begin{pmatrix} 1 \\ 1 \end{pmatrix} = e^{-j(K\ell)}\begin{pmatrix} 1 \\ 1 \end{pmatrix} + j(\lambda_b/R_e)\sin(K\ell)\begin{pmatrix} 1 \\ -1 \end{pmatrix} \tag{10}$$

that is, a bend of effective radius R_e delays the symmetric mode by the arc length of the bend and generates a phase quadrature asymmetric normal mode having a strength proportional to the ratio of the beat length and the effective curvature $1/R_e$. The two modes give rise to small oscillating components in each core as λ_b and therefore K is swept by varying the wavelength. In a like manner, an asymmetric mode is advanced in phase by the bend and generates a phase quadrature symmetric mode. If the arc is followed by a straight section of fiber of length ℓ_o, each mode acquires an additional phase advance or delay, as can be seen from Equation (9) in the limit $1/R_e \to 0$. The net result is a core contrast Q(K) formed by the ratio of the difference in light intensities in the cores to the total power transmitted by the fiber that is proportional to the curvature of the arc and consists of two harmonic components related to the distance of the arc from the end of the fiber and its total length:

$$Q(K) \equiv \frac{a_1 a_1^* - a_2 a_2^*}{a_1 a_1^* + a_2 a_2^*} = \frac{1}{2}(\delta/K)\left\{\cos\left[2K(\ell_o + \ell)\right] - \cos(2K\ell_o)\right\} \tag{11}$$

Thus, the mode coupling due to the bend produces harmonic components in the spectrum of Q. If the wavelength is scanned over a narrow band then π/λ_b is approximately a linear function of λ and the spectral lines at $(\ell_o + \ell)$ and ℓ_o have the characteristic sinc function shapes of the Fourier transform of a pulse-modulated wave.

The effective radius R_e can be directly related to the bending strain or moment in a beam. If the fiber sensor is a distance C above the neutral axis of the beam then

$$1/(R-C) = M/EI \tag{12}$$

where M is the bending moment, E is Young's Modulus and I is the moment of inertia. The bending strain

$$\varepsilon = C/(R-C) \simeq C/R \tag{13}$$

To summarize, a bend in the sensor caused by a localized strain disturbance generates a harmonic component in the core contrast with a frequency determined by the length and location of the bend from the detector and with a spectral amplitude proportional to the bending strain.

The preceeding analysis can be generalized to the case of nonuniform bends by approximating the deflection curve by a spline function; that is by a piecewise continuous set of cubic functions. The principle results will be stated in the next section which also gives some specific examples of the crosstalk spectrum for various disturbances.

2. GENERAL MODEL OF A TWIN-CORE DISTRIBUTED STRAIN SENSOR

The relationship between the core contrast spectrum and the bending strain or the curvature of the fiber is in the form of an integral equation in the most general case. It is derived from the matrizant solution of a linear system of first order differential equations (Reference 5). The two coupled mode Equations (2) and (3) for the amplitudes of the fields in the cores are an example of such a system. If the mode conversion due to the varying curvature is weak, that is, if $\lambda_b/R_e \ll 1$ throughout the length of the sensor, then the integral equation, which is generally in the form of a convergent series of product integrals (Reference 6), reduces to a simple Fourier integral that can be solved by well known transform methods. An alternate approach to solving the integral equation is to model the bending curve by spline functions; that is by a set of piecewise smooth cubics whose coefficients are determined by the crosstalk spectrum. This is possible because the coupled mode equations have an analytical solution if the curvature is a linear function of the fiber length (Reference 7). There are some other isolated cases where the connection between the bending strain and the spectrum can also be obtained in closed form; however, the curvature must match one of the known solutions of the Ricatti equation (Reference 8).

The first step in developing a general model for the effect of variable fiber curvature on the core contrast spectrum is to introduce a local normal mode transformation. At every point along the fiber we can reexpress the HE_{11} mode individual core amplitudes a_1 and a_2 in terms of new variables A_1 and A_2 that are the amplitudes of the local two-core fiber modes. This is accomplished by means of an orthogonal transformation

$$T_N(\ell) = \begin{bmatrix} \cos(\xi/s) & \sin(\xi/2) \\ -\sin(\xi/2) & \cos(\xi/2) \end{bmatrix} \tag{14}$$

applied to the vector $\left(A_1(1),\ A_2(1)\right)^t$ of individual core amplitudes, where

$$\cos^2(\xi/2) = \frac{1}{2}\left[1+\delta/K\right], \tag{15}$$

$$\sin^2(\xi/2) = \frac{1}{2}\left[1-\delta/K\right], \tag{16}$$

and

$$\delta/K = 1\Big/\sqrt{1 + (R_e/\lambda_b)^2} \tag{17}$$

A new set of coupled-mode equations for A_1 and A_2 follows from Equations (2) and (3) by using

$$\begin{pmatrix} a_1 \\ a_2 \end{pmatrix} = T_N^{-1} \cdot \begin{pmatrix} A_1 \\ A_2 \end{pmatrix} \tag{18}$$

where

$$T_N^{-1} = \begin{bmatrix} \cos(\xi/2) & -\sin(\xi/2) \\ \sin(\xi/2) & \cos(\xi/s) \end{bmatrix} \tag{19}$$

The take the form

$$\begin{pmatrix} A_1'(\ell) \\ A_2'(\ell) \end{pmatrix} = \begin{bmatrix} -j(\beta_o+K) & 1/2\ \xi' \\ -1/2\ \xi' & -j(\beta_o-K) \end{bmatrix} \cdot \begin{pmatrix} A_1(\ell) \\ A_2(\ell) \end{pmatrix} \tag{20}$$

where the mode coupling parameter ξ', which is derived by differentiating Equations (15) and (16), is

$$\xi' \equiv \frac{d\xi}{d\ell} = 2(\delta/K)'/[1-(\delta/K)]^2 \tag{21}$$

Along a straight section of fiber or an arc of constant curvature $\xi' = 0$ and no mode conversion takes place. In this case the solution of Equation (20) is

$$\begin{pmatrix} A_1(\ell) \\ \\ A_2(\ell) \end{pmatrix} = \begin{pmatrix} A_1(0)e^{-j(\beta_o+K)\ell} \\ \\ A_2(0)e^{-j(\beta_o-K)\ell} \end{pmatrix} \tag{22}$$

Note, however, that along an arc the normal modes differ from those of a straight section. If $(\lambda_b/R_e) \to 0$, then

$$\begin{pmatrix} A_1(\ell) \\ \\ A_2(\ell) \end{pmatrix} = 1/\sqrt{2}\; e^{-j\beta_o\ell} \begin{pmatrix} (a_1(0)+a_2(0))e^{-j\pi\ell/\lambda_b} \\ \\ (a_2(0)-a_1(0))e^{j\pi\ell/\lambda_b} \end{pmatrix} \tag{23}$$

and to lowest order in (λ_b/R_e)

$$\begin{pmatrix} A_1 \\ \\ A_2 \end{pmatrix} = 1/\sqrt{2}\; e^{-j\beta_o\ell} \begin{pmatrix} [a_1(0)+a_2(0)]e^{-j\pi\ell/\lambda_b} + \frac{1}{2}(\lambda_b/R_e)[a_1(0)-a_2(0)]e^{-j\pi\ell/\lambda_b} \\ \\ [a_2(0)-a_1(0)]e^{j\pi\ell/\lambda_b} - \frac{1}{2}(\lambda_b/R_e)[a_1(0)+a_2(0)]e^{j\pi\ell/\lambda_b} \end{pmatrix} \tag{24}$$

Thus, the normal modes in a section of constant curvature, an arc, are linear combinations of the symmetric and asymmetric modes of a straight section – a result obtained in a somewhat different way in the preceeding section (see Equations (9) and (10).

The local normal mode equations can be simplified further by applying phase transformations to each of the mode amplitudes. Let

$$B_{1,2}(\ell) = A_{1,2}(\ell)\cdot e^{j\int_0^{\ell} (\beta_o \pm K)dz} \qquad (25)$$

and

$$u = 2\int_0^{\ell} K\,dz \qquad (26)$$

This reduces Equation (20) to

$$\begin{pmatrix} \frac{dB_1}{du} \\ \frac{dB_2}{du} \end{pmatrix} = \begin{bmatrix} 0 & \frac{1}{2}\frac{d\xi}{du} e^{ju} \\ -\frac{1}{2}\frac{d\xi}{du} e^{-ju} & \end{bmatrix} \cdot \begin{pmatrix} B_1(u) \\ B_2(u) \end{pmatrix} \qquad (27)$$

The mode conversion parameter $\gamma \equiv -1/2\ d\xi/du$ can be written in terms of the curvature, its rate of change along the fiber, and the cross-talk beat length. The required relationship is given by substituting Equations (7) and (8) into Equation (21):

$$\gamma = \frac{\pi^2 n_1 (d/\lambda)/\lambda_b}{4\{[\pi n_1 d/\lambda \cdot (1/R)]^2 + (\pi/\lambda_b)^2\}^{3/2}} \cdot \left[\frac{d}{d\ell}(1/R) - (\lambda_b/R)\frac{d}{d\ell}(1/\lambda_b)\right] \qquad (28)$$

If $\lambda_b << R$ and the beat length is slowly varying -- i.e., at a rate equal or less than the variation in curvature -- then

$$\gamma \simeq (1/4\pi)(n_1 d/\lambda)\ \lambda_b^2\ d/d\ell\ (1/R) \qquad (29)$$

Since the bending strain is proportional to the fiber curvature (see Equation (13)), γ is proportional to the rate of change of bending strain. When γ is piecewise constant then Equation (27) can be solved analytically.

In most cases of interest the radius of curvature is large and gradually varying. For these conditions

$$u \simeq 2\kappa\ell \tag{30}$$

where $\kappa \equiv \pi/\lambda_b$ is the cross-talk spatial frequency, and

$$\gamma \simeq (\pi/4)(d/\lambda)(1/\kappa^2)\frac{d}{d\ell}(1/\kappa) \tag{31}$$

Applying these approximations to Equation (27), we can simplify the reduced normal equations to the following form:

$$\frac{dB}{d\ell} = P(\ell)B \tag{32}$$

$$B \equiv \begin{pmatrix} B_1 \\ B_2 \end{pmatrix} \; ; \; P(\ell) = \begin{bmatrix} 0 & -\varepsilon'(\ell)/\kappa \cdot e^{j2\kappa\ell} \\ \varepsilon'(\ell)/\kappa \cdot e^{-j2\kappa\ell} & 0 \end{bmatrix}$$

where $\varepsilon'(\ell) = 2\kappa\gamma(\ell)$ is apart from a constant factor the rate-of-change of the bending strain along the fiber.

The solution to Equation (32) is given in terms of the matrizant $\Omega_o^\ell(P)$

$$B(\ell) = \Omega_o^\ell \cdot B(0) \tag{33}$$

where

$$\Omega_o^\ell(P) \equiv I + \int_o^\ell P(z_1)dz_1 + \int_o^\ell P(z_2)\int_o^{z_2} P(z_1)dz_1 dz_2 + \ldots \tag{34}$$

is an absolutely and uniformly convergent infinite series of matrices with the identity matrix I as the leading term. Each term is derived from a successive approximation to the solution of Equation (33). The solution can be thought of as composed of a series of successively higher-order multiple mode conversions. Convergence takes place quickly if $\gamma_{max} << 1$; then

$$\Omega_o^\ell(P) \simeq I + \begin{bmatrix} 0 & -\int_o^\ell \varepsilon'(z)/\kappa \cdot e^{j2\kappa z}dz \\ \int_o^\ell \varepsilon'(z)/\kappa \cdot e^{-j2\kappa z}dz & 0 \end{bmatrix} + \mathcal{O}(\gamma_{max}^2) \tag{35}$$

The amplitudes of the individual core modes at the end of a fiber of length L can be written in terms of the truncated matrizant Equation (35) and the incident illumination expressed as a linear combination of local normal modes by using Equations (25) and (18):

$$\begin{pmatrix} a_1(L) \\ \\ a_2(L) \end{pmatrix} \simeq 1/\sqrt{2}\, e^{-j(\beta_o+\kappa)L} \begin{bmatrix} 1 & -e^{j2\kappa L} \\ \\ 1 & e^{j2\kappa L} \end{bmatrix} \cdot \Omega_o^{\ell} \cdot B(0) \tag{36}$$

To illustrate the form of the integral equation relating $\varepsilon(\ell)$ to the cross talk spectrum, consider the case of equal and in-phase illumination of both cores. In this example only the symmetric mode is launched and Equation (36) reduces to

$$\begin{pmatrix} a_1(L) \\ \\ a_2(L) \end{pmatrix} = 1/\sqrt{2}\, e^{-j(\beta_o+\kappa)L} \begin{pmatrix} 1 - \int_o^L \varepsilon'(z)/\kappa\, e^{j2\kappa(L-z)}\, dz \\ \\ 1 + \int_o^L \varepsilon'(z)/\kappa\, e^{j2\kappa(L-z)}\, dz \end{pmatrix} \tag{37}$$

The core contrast is given by

$$\begin{aligned} Q(\kappa) &= (a_2 a_2^* - a_1 a_1^*)/(a_1 a_1^* + a_2 a_2^*) \\ &= 2 \int_o^L \varepsilon'(z)/\kappa \cdot \cos[2\kappa(L-z)]\, dz \end{aligned} \tag{38}$$

The final result is obtained by integrating Equation (38) by parts:

$$\begin{aligned} Q(\kappa) &= (2/\kappa)\, [\varepsilon(L) - \varepsilon(0) \cos 2\kappa L] \\ &\quad - 4 \int_o^L \varepsilon(z) \sin[2\kappa(L-z)]\, dz \end{aligned} \tag{39}$$

If the strain (curvature) is zero at the ends of the sensor, then Equation (39) shows that the cross talk spectrum -- i.e., the core contrast considered a function of the wavelength through the spatial frequency κ -- is directly related to a folded Fourier sine transform of the unknown strain distribution $\varepsilon(z)$. Thus, we have solved the general form of the integral Equation (36) by reducing it to a Fourier transform pair.

When a small fraction f of the antisymmetric mode is also launched $B(0) = (1,f)^t$ and Equation (36) becomes

$$\begin{pmatrix} a_1(L) \\ \\ a_2(L) \end{pmatrix} = 1/\sqrt{2}\; e^{-j(\beta_o+\kappa)L} \begin{pmatrix} 1-f\int_o^L \varepsilon'/\kappa e^{j2\kappa z}dz - e^{j2\kappa L}\left(f+\int_o^L \varepsilon'/\kappa e^{-j2\kappa z}dz\right) \\ \\ 1-f\int_o^L \varepsilon'/\kappa e^{j2\kappa z}dz + e^{j2\kappa L}\left(f+\int_o^L \varepsilon'/\kappa e^{-j2\kappa z}dz\right) \end{pmatrix} \quad (40)$$

The corresponding expression for core contrast is

$$Q(\kappa) = \frac{2}{(1+f^2)} \cdot \mathrm{Re}\left\{(1-f^2)\int_o^L \varepsilon'(z)/\kappa e^{j2\kappa(L-z)}dz \right.$$

$$\left. + f\left[e^{j2\kappa L} - e^{-j2\kappa L}\left(\int_o^L \varepsilon'(z)/\kappa e^{j2\kappa(L-z)}dz\right)^2\right]\right\} \quad (41)$$

Equation (41) can be solved iteratively if $f \ll 1$ by using the solution to Equation (39) as a first approximation. When f is not small, i.e., of order one, then Equation (41) must be solved numerically. It is a nonlinear equation relating the real and imaginary parts of the Fourier transform of the bending strain $\varepsilon(\ell)$ to $Q(\kappa)$. In order to solve it the Hilbert transform relationship must be used to eliminate the real or imaginary part of the transform from the equation. In most instances this is not necessary since the incident illumination can be selected to have nearly equal amplitudes in each core, insuring $f \ll 1$.

3. CROSS-TALK SPECTRA OF PURE BENDS

Any disturbance composed of pure bends or arcs of constant curvature joined by straight sections of fiber can be analyzed by multiplying the crosstalk transfer matrices of each section, forming the core contrast function from the output core amplitudes and Fourier transforming the result to obtain the cross-talk spectrum. In this section we develop and carryout these computations for several specific examples selected to model the experimental geometries and predict the measured crosstalk spectra.

a. Model of Right Angle Bend

Consider a twin-core fiber of total length L bent by a circular disk of radius r located between straight sections of fiber of lengths ℓ_1, and ℓ_2 (see Figure 7). The incident illumination can be decomposed into a sum of normal modes

$$\begin{pmatrix} a_1(0) \\ a_2(0) \end{pmatrix} = \begin{pmatrix} 1 \\ 1 \end{pmatrix} + f \begin{pmatrix} 1 \\ -1 \end{pmatrix} \tag{42}$$

A straight section of fiber delays and advances the normal modes by the cross-talk beat phase $\phi_1 = \pi/\lambda_b \cdot \ell_1$ of the length ℓ_1. The curved section is illuminated by

$$\begin{pmatrix} a_1(\ell_1) \\ a_2(\ell_1) \end{pmatrix} = e^{-j\phi_1} \begin{pmatrix} 1 \\ 1 \end{pmatrix} + fe^{j\phi_1} \begin{pmatrix} 1 \\ -1 \end{pmatrix} \tag{43}$$

A circular arc has a transfer matrix of the form

$$T = \begin{bmatrix} \cos \phi_2 & -j(\kappa/K)\sin \phi_2 \\ -j(\kappa/K)\sin \phi_2 & \cos \phi_2 \end{bmatrix}$$

$$+ j(\delta/K)\sin \phi_2 \begin{bmatrix} 1 & 0 \\ 0 & -1 \end{bmatrix} \tag{44}$$

where

$$\phi_2 = Krs \qquad , \quad K = \sqrt{\kappa^2+\delta^2}$$

$$\delta = (\pi/\lambda)(n_1 d/r) \quad , \quad \kappa = \pi/\lambda_b$$

At the end of the curved section

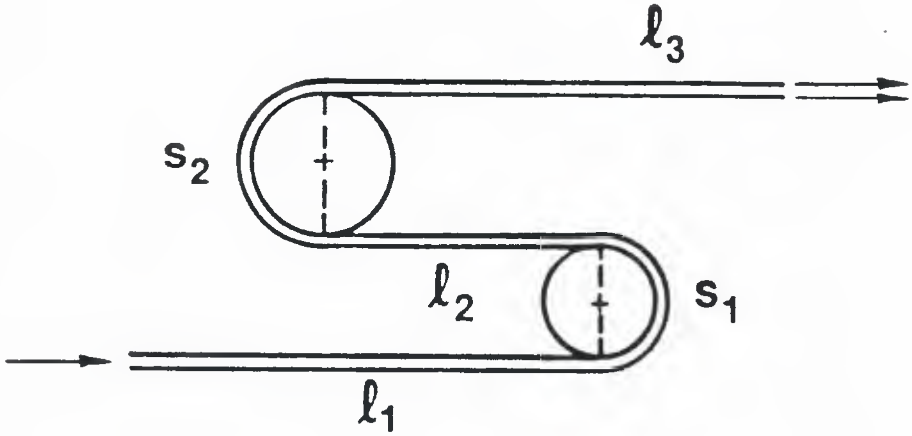

Figure 7. Geometry of Twin-Core Sensor Bent by Two Circular Disks

$$\begin{pmatrix} a_1 \\ a_2 \end{pmatrix} = \left\{[\cos\phi_2 - j(\kappa/K)\sin\phi_2]e^{-j\phi_1} + jfe^{j\phi_1}(\delta/K)\sin\phi_2\right\}\cdot\begin{pmatrix} 1 \\ 1 \end{pmatrix}$$

$$+ \left\{f[\cos\phi_2 + j(\kappa/K)\sin\phi_2]e^{j\phi_1} + je^{-j\phi_1}(\delta/K)\sin\phi_2\right\}\cdot\begin{pmatrix} 1 \\ -1 \end{pmatrix} \tag{45}$$

The remaining straight section introduces an additional phase change $\phi_3 = \pi/\lambda_b \cdot \ell_3$ (similar to the first section of fiber) but no further mode conversion. Thus at the end of the fiber

$$\begin{pmatrix} a_1(L) \\ a_2(L) \end{pmatrix} = \left\{[\cos\phi_2 - j(\kappa/K)\sin\phi_2]e^{-j(\phi_1+\phi_3)} + jfe^{-j(\phi_3-\phi_1)}(\delta/K)\sin\phi_2\right\}\cdot\begin{pmatrix} 1 \\ 1 \end{pmatrix}$$

$$+ \left\{f[\cos\phi_2 + j(\kappa/K)\sin\phi_2]e^{j(\phi_1+\phi_3)} + je^{-j(\phi_1-\phi_3)}(\delta/K)\sin\phi_2\right\}\cdot\begin{pmatrix} 1 \\ -1 \end{pmatrix} \tag{46}$$

A general expression for $Q(\kappa)$ can be derived from Equation (46) in a straightforward way but it is lengthy and complicated when no assumptions are made about the relative size of the geometrical and fiber parameters and the nature of the incident illumination. It is more useful to exhibit a few limiting cases that are tractable and which give rise to easily understood, recognizable spectral features. More general results are easily obtained by direct matrix multiplication of the appropriate chain of transfer functions and numerical computation of the spectrum using an FFT algorithm.

If the radius of curvature is large, then $\delta/K \ll 1$ and $K \simeq \kappa$. In this limit, to lowest order in λ_b/r

$$Q(K) = f\cos(2\kappa L) + 1/2(\delta/\kappa)(1-f^2) \cdot\{\cos[2\kappa(s+\ell_2)] - \cos(2\kappa\ell_2)\} \tag{47}$$

Generally, there will be three spectral components in the transform of the core contrast function located at distance from the origin proportional to the total fiber length L, to the length ℓ_2 of the second straight segment and at a distance directly related to the sum of the arc s and ℓ_2. The type of incident illumination, characterized by the fraction of the antisymmetric mode launched at the input face of the fiber, influences the heights of the spectral lines but not their location. If the fractional bandwidth of the wavelength scan $\Delta\lambda/\lambda$ is narrow then the fractional variation in κ, $(\Delta\kappa/\kappa)$, will also be small and the coefficient (δ/κ) will be slowly varying compared to the cosine factors. It follows that the line shapes will be sinc functions having half-power widths and side lobe structures set by $\Delta\kappa$.

Before presenting some specific results to illustrate the variation in the spectral features with fiber bending strain distribution, a brief review of the discrete Fourier transform (DFT) scaling relationships and the Nyquist sampling requirement in the present context is needed. Referring to Figure 8, the crosstalk spectrum $\tilde{Q}(\ell)$ is computed from the core contrast $Q(\kappa)$, for the moment considered a function of $\kappa = \pi/\lambda_b$, by sampling in intervals $\delta\kappa$ between the initial and final values of the beat wavenumber, κ_o and κ_f, respectively. The Fourier variable conjugate to κ is a length ℓ. The scale of the spectrum as computed by the usual FFT algorithm is (ℓ/π). For example, if the most rapidly varying component in the core contrast, is $\sin(\kappa 2\ell_{max})$ then a peak will appear at a frequency $f_{max} = \ell_{max}/\pi$. Thus by rescaling the frequency axis by π, the spectrum becomes a direct function of the fiber length. The sampling interval in κ or equivalently in λ must be small enough to insure that the longest length in the spectrum is less than $\pi/(2\delta\kappa)$. As shown in Figure 8 if the sampling frequency f_s is written m/π then $m > 2\ell_{max}$ to insure the spectrum will not be aliased. The resolution or the minimum detectable length feature is determined by the bandwidth of the κ scan (or equivalently $\Delta\lambda = \lambda_f - \lambda_i$).

Experimentally, Q is a function of λ and not κ. The two variables are related though through a crosstalk coupling factor which can be computed or measured. If $\Delta\lambda/\lambda_f \ll 1$, κ is nearly a linear increasing function of λ. A linear transformation $\lambda(\kappa)$ will leave the shape of the spectrum unaltered. Only the "frequency axis" is rescaled by the slope of the $\lambda(\kappa)$ relationship. If the fiber is long enough, nonlinear terms in the power series expansion (or spline fit) of $\lambda(\kappa)$ will cause "chirping" and distort the shape of the spectral lines.

The various forms of the crosstalk spectral features generated by a single bend (Figure 7) are shown in Figures 9 through 15. In each case the total fiber length is held the same. The location of the bend, or the radius of curvature or the illumination is varied. In the first three figures of the series, Figures 9 through 11, the illumination is held constant and the position and curvature of the bend are changed. Three spectral features are expected since $\delta/\kappa < 1$ and $f = 0.1$. As predicted by Equation (47) they are located at 4", approximately the

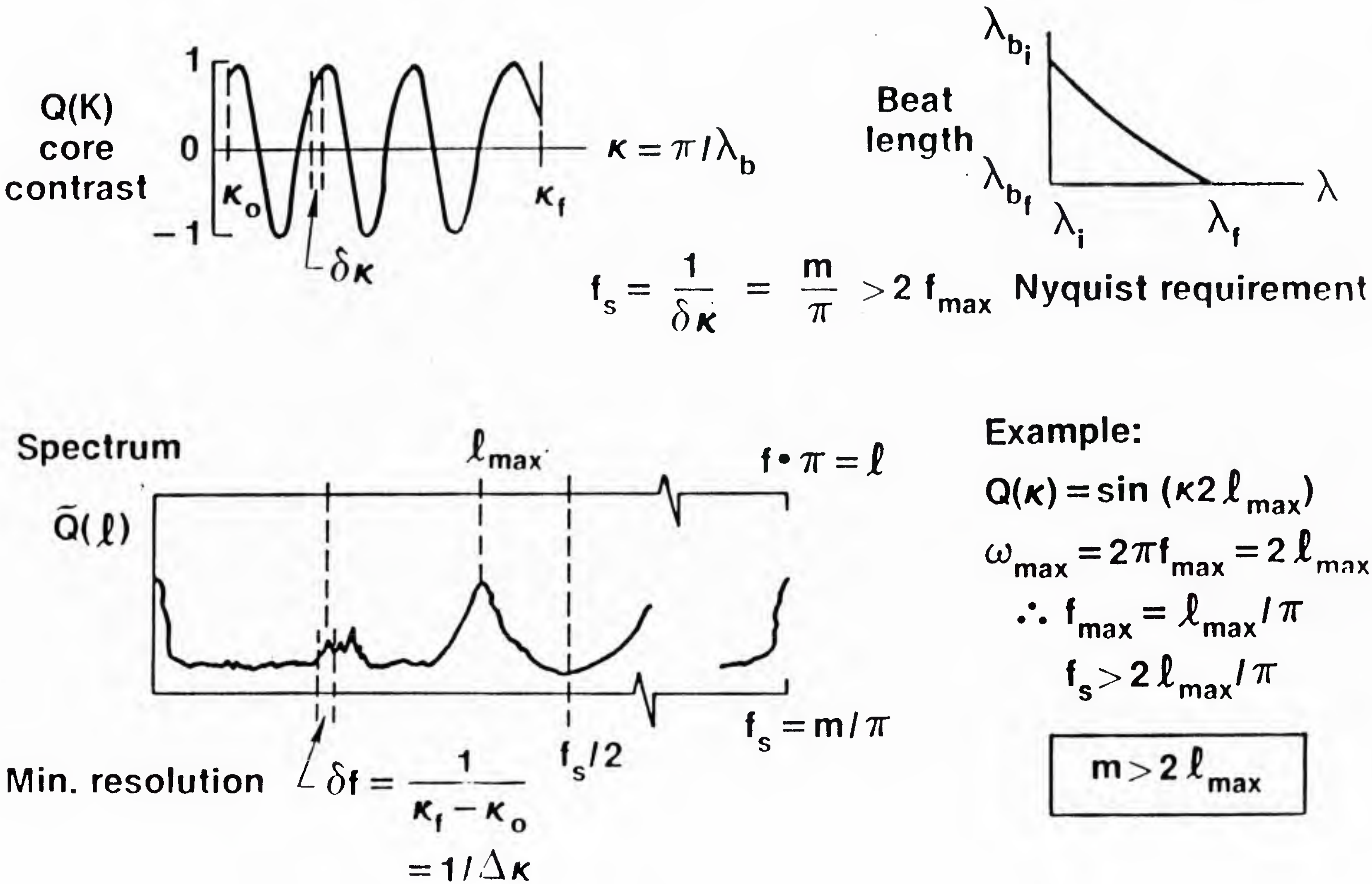

Figure 8. Crosstalk Spectral Analysis

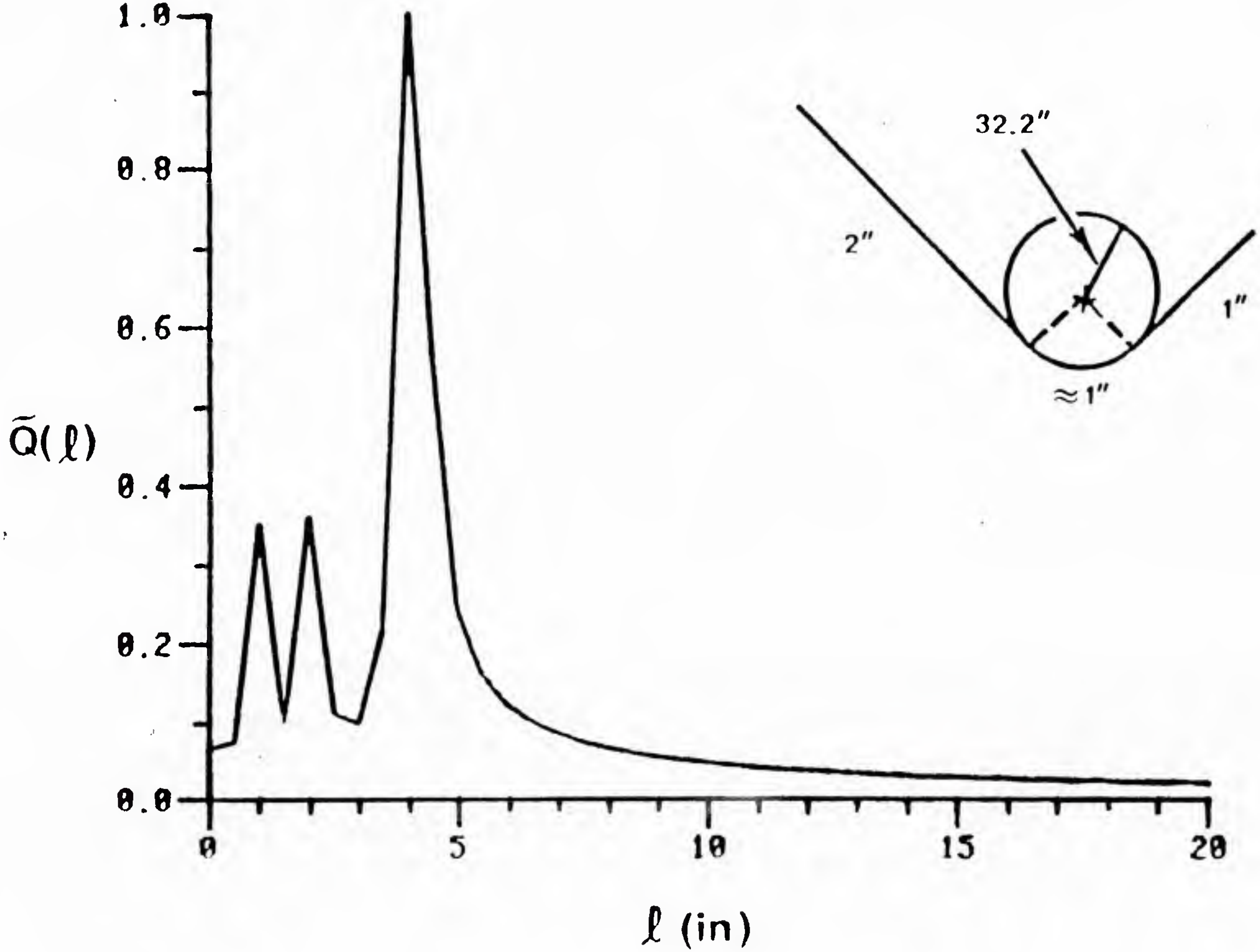

Figure 9. Spectrum of a Single Bend With a Large Radius of Curvature

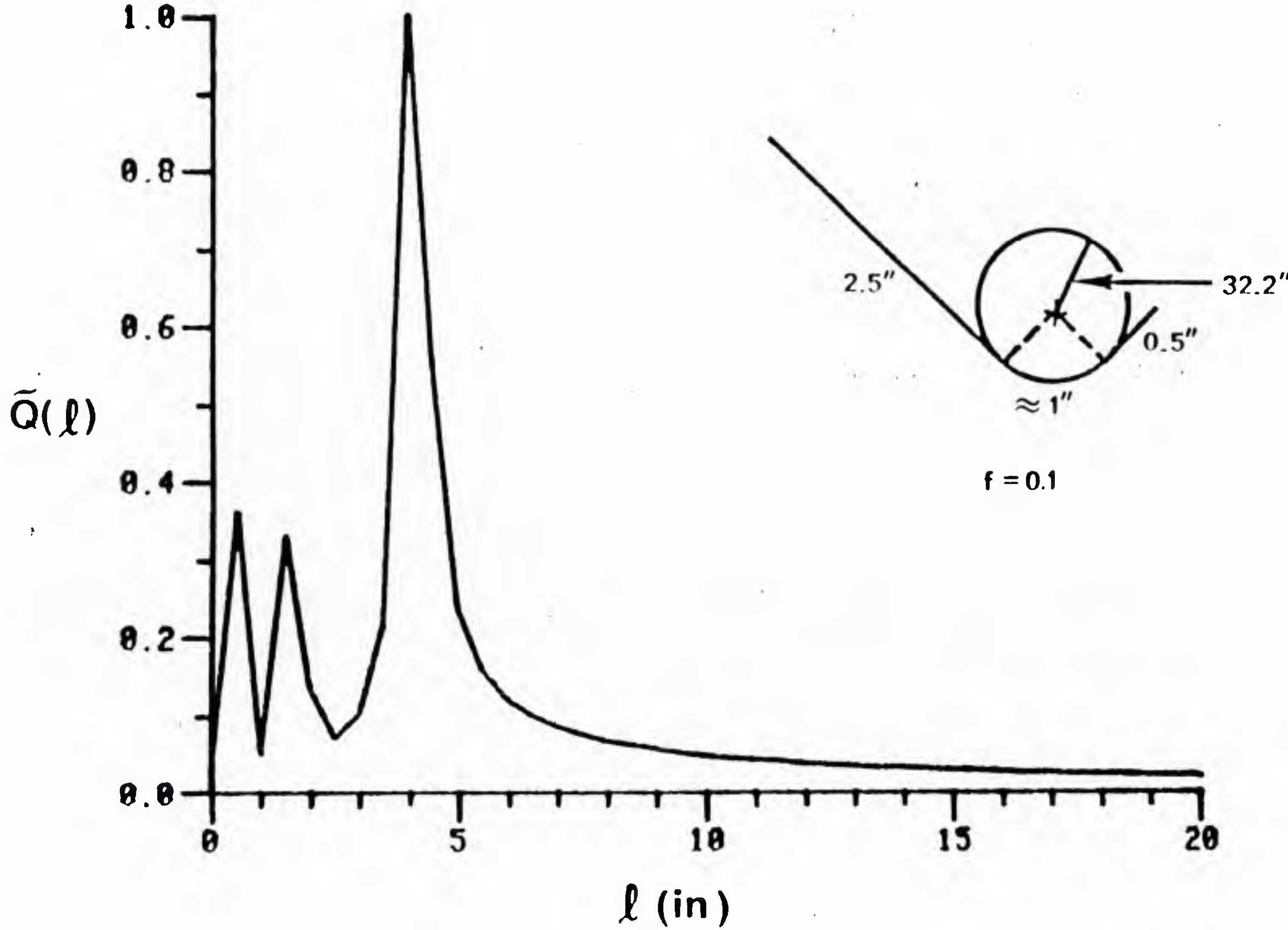

Figure 10. Spectrum of a Single Bend

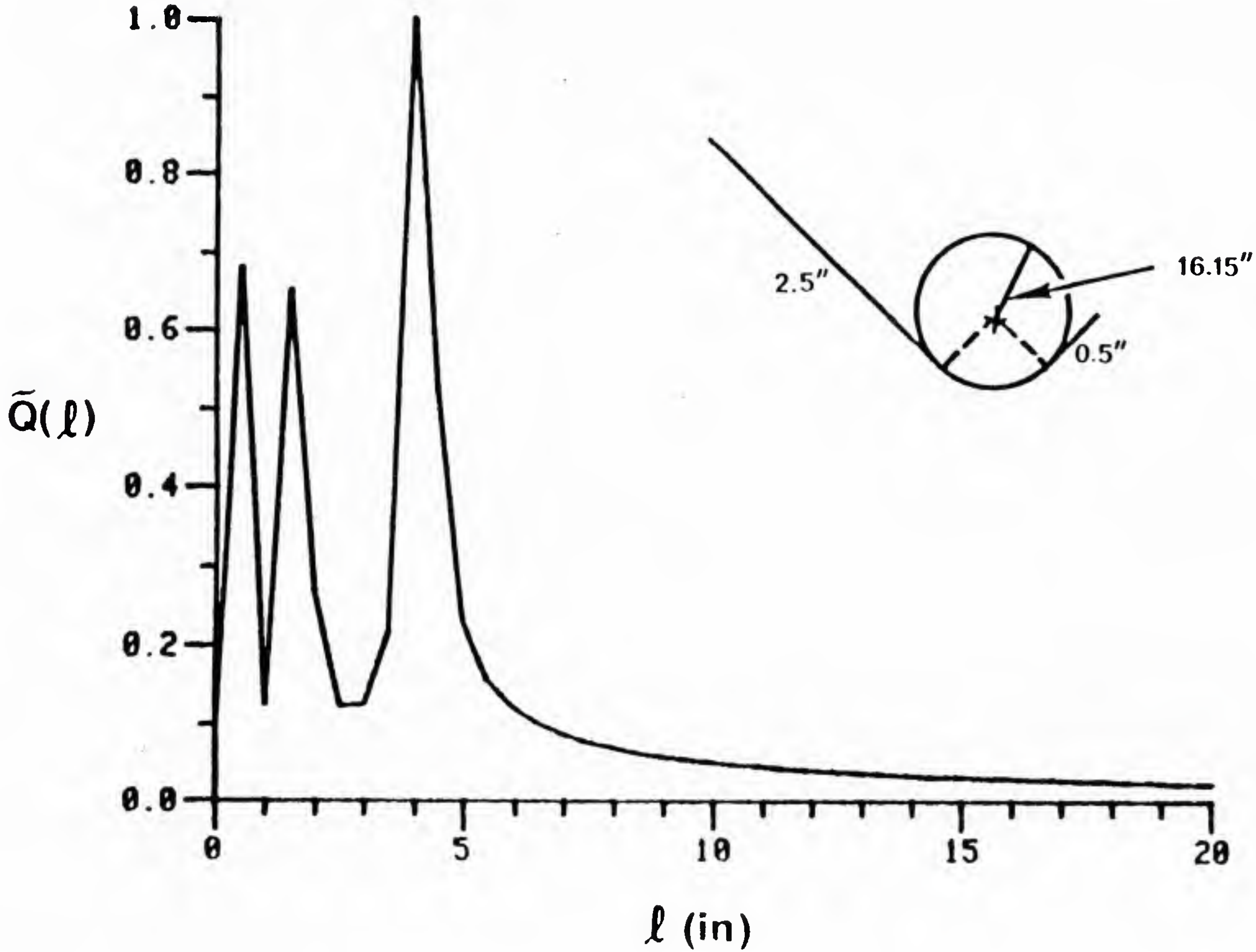

Figure 11. Spectrum of a Single Bend

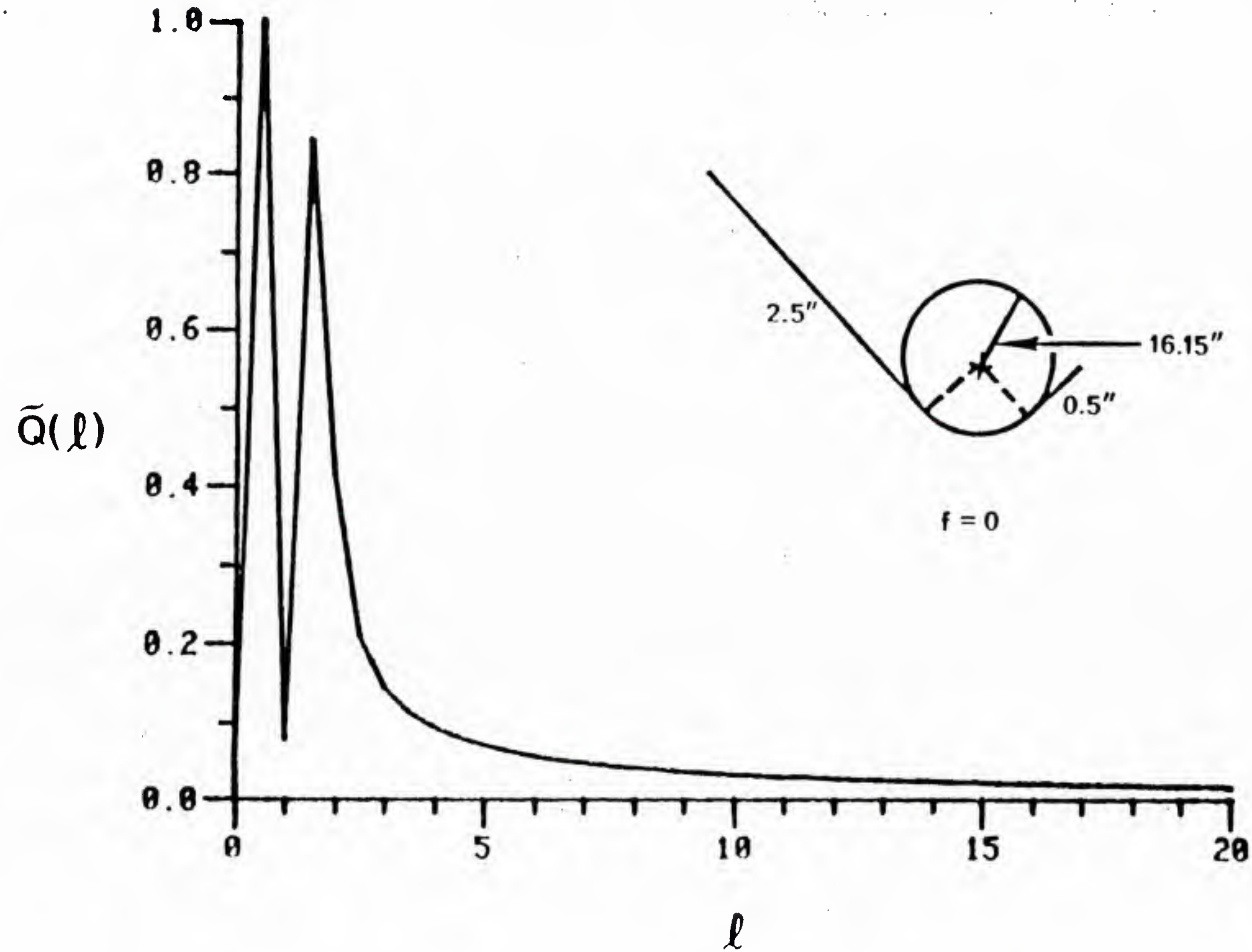

Figure 12. Spectrum of a Single Bend. Both Cores Illuminated Equally

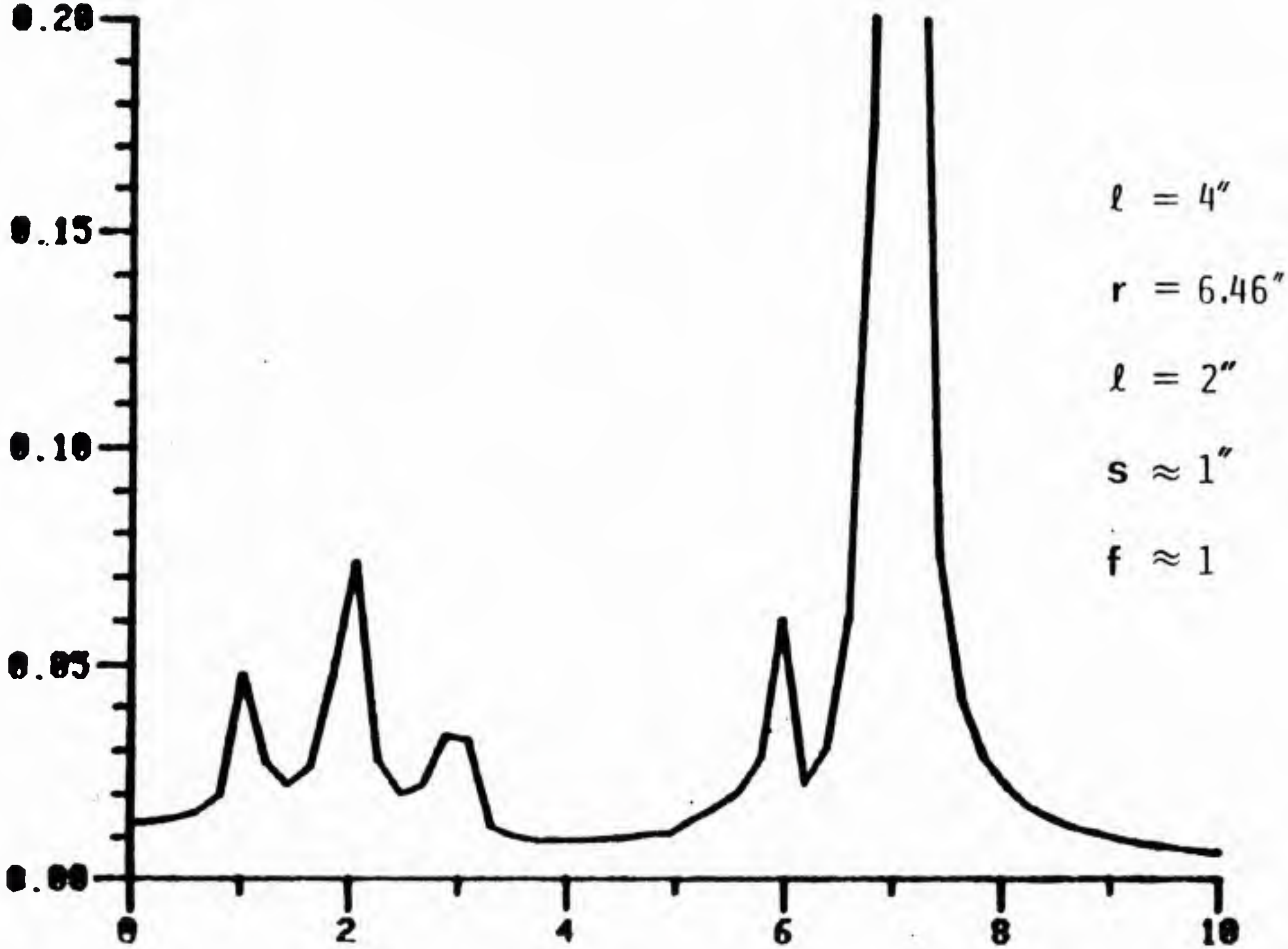

Figure 13. Spectrum of a Single Bend. One Core Illuminated

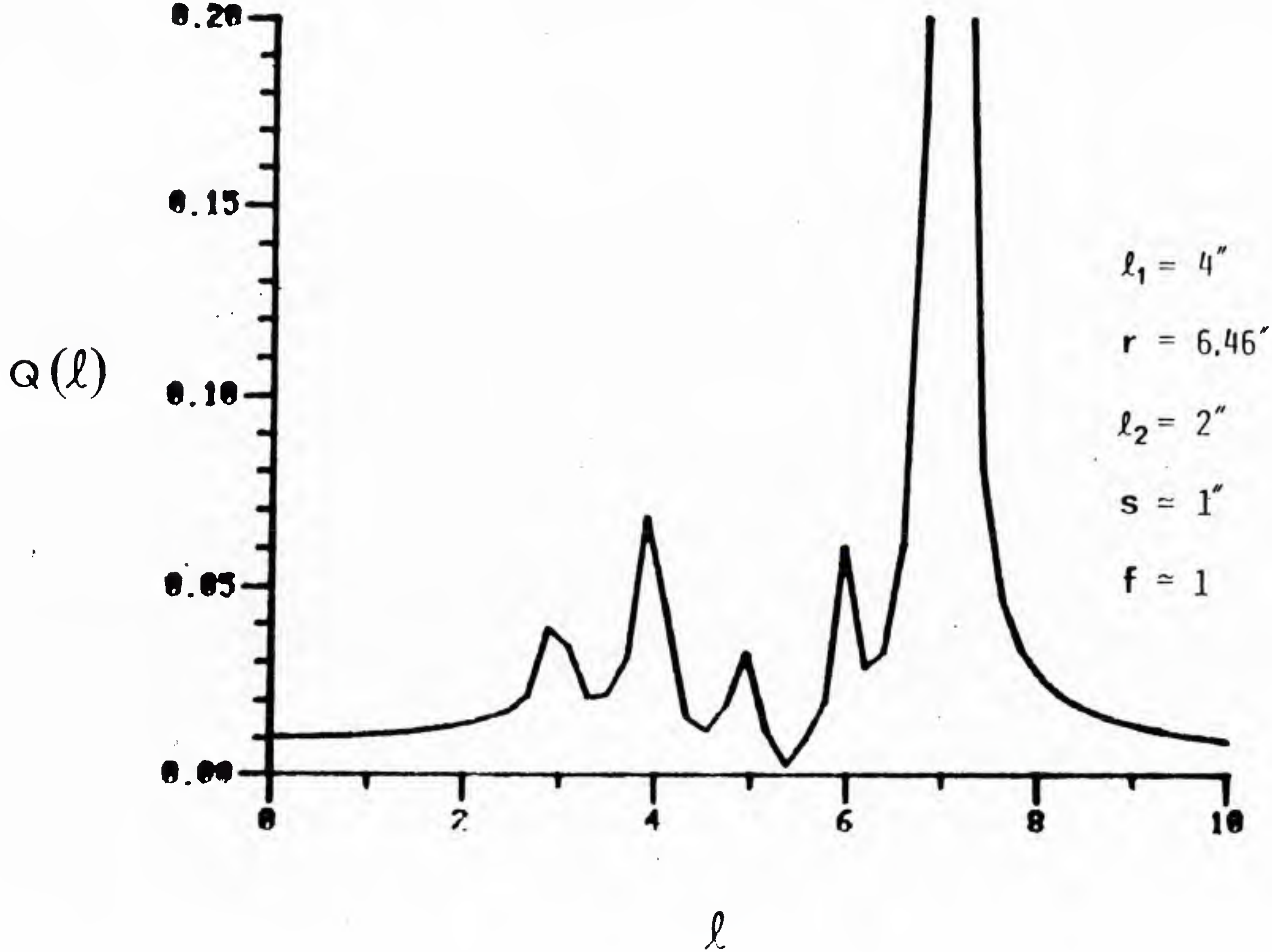

Figure 14. Spectrum of a Single Bend. One Core Illuminated (f=1)

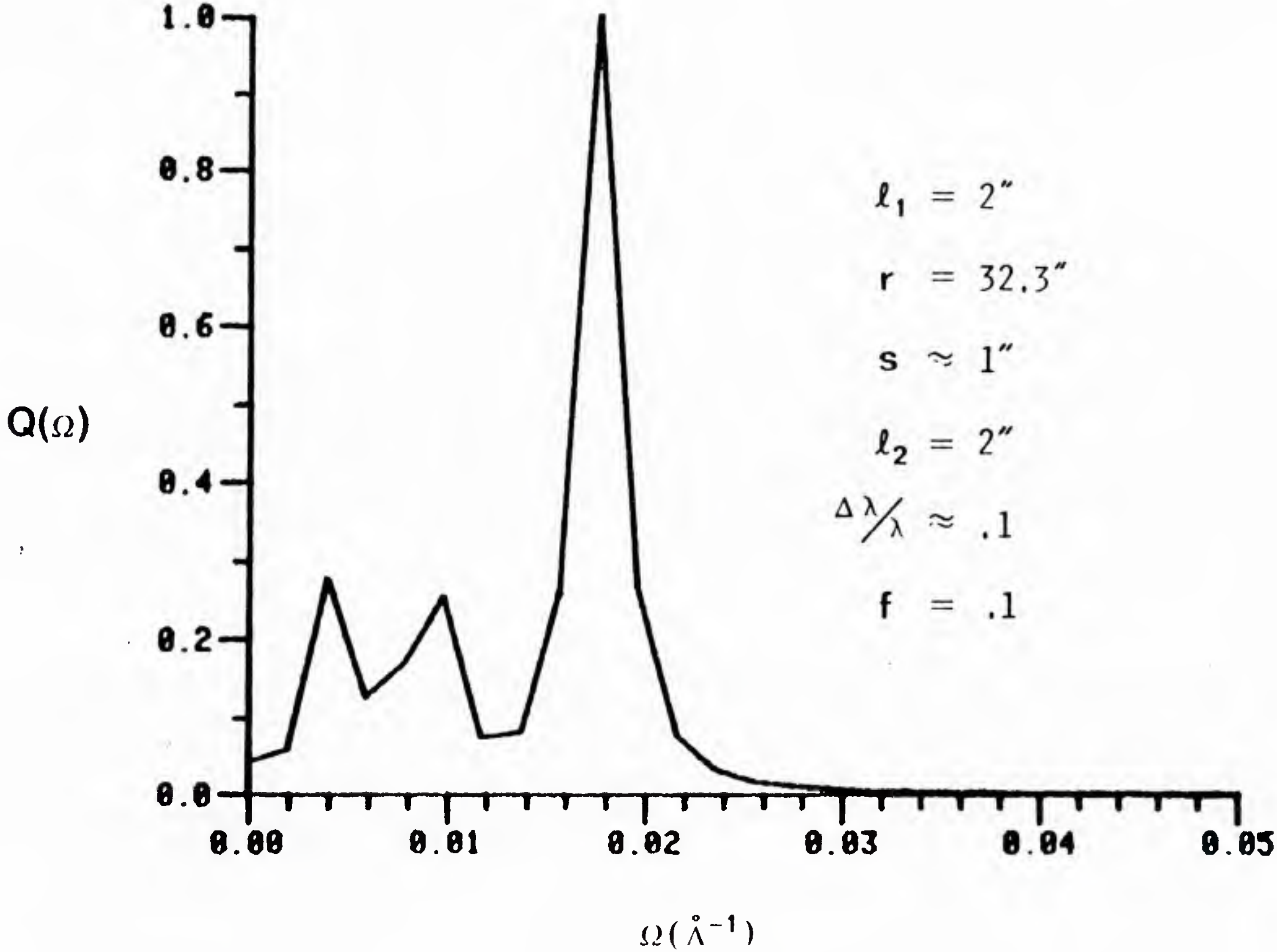

Figure 15. Spectrum of Single Bend. Core Contrast Transformed Into a Function of Wavelength

total length of the fiber, at the distance of the arc from the end of the fiber, 1 inch, and at 2 inches, the sum of the arc length and the second straight section. The location of the spectral lines are determined by the location of the bend along the fiber. The strain or radius of curvature is given by the height of the two small peaks. The resolution in this example is somewhat coarse since $1/\Delta K = 0.25$ mm implying $\delta f \simeq 0.5$ in. As a result, the heights of the peaks are underestimated because of the large sampling interval. In Figure 10, the position of the arc is moved closer to the end of the fiber, all other parameters are held constant. The pair of smaller amplitude lines shift to the appropriate location as predicted by Equation (47). In the third figure in this group the radius of curvature is halved. The pair of lines remain at the same point but their amplitude is approximately doubled.

When the illumination of the cores is equal ($f = 0$) then only two peaks appear in the spectrum. Figure 12 is a graph of the spectrum for the same geometry in Figure 11 but $f = 0$. Again the two lines should have the same amplitude but the resolution is not fine enough to sample at or very close to the maxima. If the excitation is balanced, crosstalk occurs only when the fiber is bent.

When only one core is illuminated ($f = 1$) the effect of the bend on the spectrum is second order in δ/κ. In this case

$$Q(\kappa) = \left[1-1/2(\delta/\kappa)^2\right] \cos(2\kappa L) + 1/2(\delta/\kappa)^2\{\cos\left[2\kappa(\ell_1-\ell_2)\right.$$
$$+ \cos\left[2\kappa(L-s)\right] - 1/2\left[\cos\left[2\kappa(\ell_1-\ell_2+s)\right]\right.$$
$$\left.+ \cos\left[2\kappa(\ell_1-\ell_2-s)\right]\right]\}$$

and the spectrum has three minor lines grouped about $\ell = \ell_1-\ell_2$, plus a small component at $\ell = L-s$.

Figure 13 is an example of a typical single bend spectrum when only one core of the fiber is illuminated. Note the triplet of lines clustered about the point $\ell_1-\ell_2 = 2$ inches and the minor peak at $L-s = 6$ inches. Another example is shown in Figure 14. Here ℓ_1 is lengthened to 5 inches and ℓ_2 is shortened by 1 inch to keep the total length constant; the triplet is displaced by 2 inches from its position in Figure 13 and the other two lines remain in the same place, all in accord with Equation (48).

The spectral features become more complicated if the contrast is considered to be a function of wavelength. Consider a typical term of the form cos $(2\kappa L)$. If the fractional spectral width of the wavelength scan is small, γ can be expanded is a power series in λ:

$$\kappa(\lambda) = \kappa_o + C_1 \frac{(\lambda - \lambda_o)}{\lambda_o} + C_2 \left[\frac{(\lambda - \lambda_o)}{\lambda}\right]^2 \quad (49)$$

The line shape is the same as the spectrum of a frequency chirped pulse (see Reference 11 for a discussion of the linear FM signal spectrum). A ripple develops in each of the lines due to the quadratic term in Equation (49). Even though the quadratic variation in $\kappa(\lambda)$ may be small, if the fiber is long enough $C_2L\ (\Delta\lambda/\lambda)^2$ may be significant. Figures 15 and 16 illustrate this effect. In the second figure the length has been increased by a factor of 5. Note the double peak shape of the principal spectral line in Figure 16. The minor peaks will not exhibit this ripple until the length is further increased or the bend becomes very long since it is the product of the characteristics length associated with a particular spectral feature and the chirp coefficient C_2 that controls the line shape distribution.

b. Crosstalk Spectra of Distributed Nonuniform Bends

A clamped cantilever beam with a uniformly distributed load is a rudimentary model of a wing spar. This example provides an illustration of the approximate Fourier transform relationship between the fiber deflection curve (or the elastic curve of a structural member) and the observed crosstalk core constant.

A twin-core fiber is embedded in or attached to prismatic beam and illuminated by a tunable wavelength source (Figure 17). Both cores are assumed to be illuminated equally and in phase. Core contrast is recorded at the end of fiber by an appropriate detector or pair of detectors. The moment distribution and bending strain are shown in Figures 18 and 19. The rate-of-change of the curvature - here approximated by a set of constant segments (Figure 20) is related to the distribution of shear forces in the beam. It and the relative size of λ_b/R_{min} determine the variation in the mode coupling parameter $\gamma(\ell)$. The magnitude of the coefficients in the reduced normal mode Equation (32) are proportional to $2K\gamma(\ell)$ which is plotted in Figure 21. Note the small difference between the form of coupling parameter and the shear diagram or $\varepsilon'(\ell)$.

The core contrast (Figure 22) here considered to be a function of the beat wavenumber K is calculated by numerically integrating the reduced normal mode equation. The Fourier sine transform of Q(K), windowed by the finite scan in K, is shown in Figure 23. It approximates the imposed strain distribution in the beam. Note that the transform scale is shifted and reversed (see Equation (39)).

An example of a beam with both point and distributed loads is shown in Figure 24. The corresponding shear diagram and the core contrast function are plotted in Figures 25 and 26. Regions of large strain are correctly identified in the rescaled Fourier sine transform shown in Figure 27.

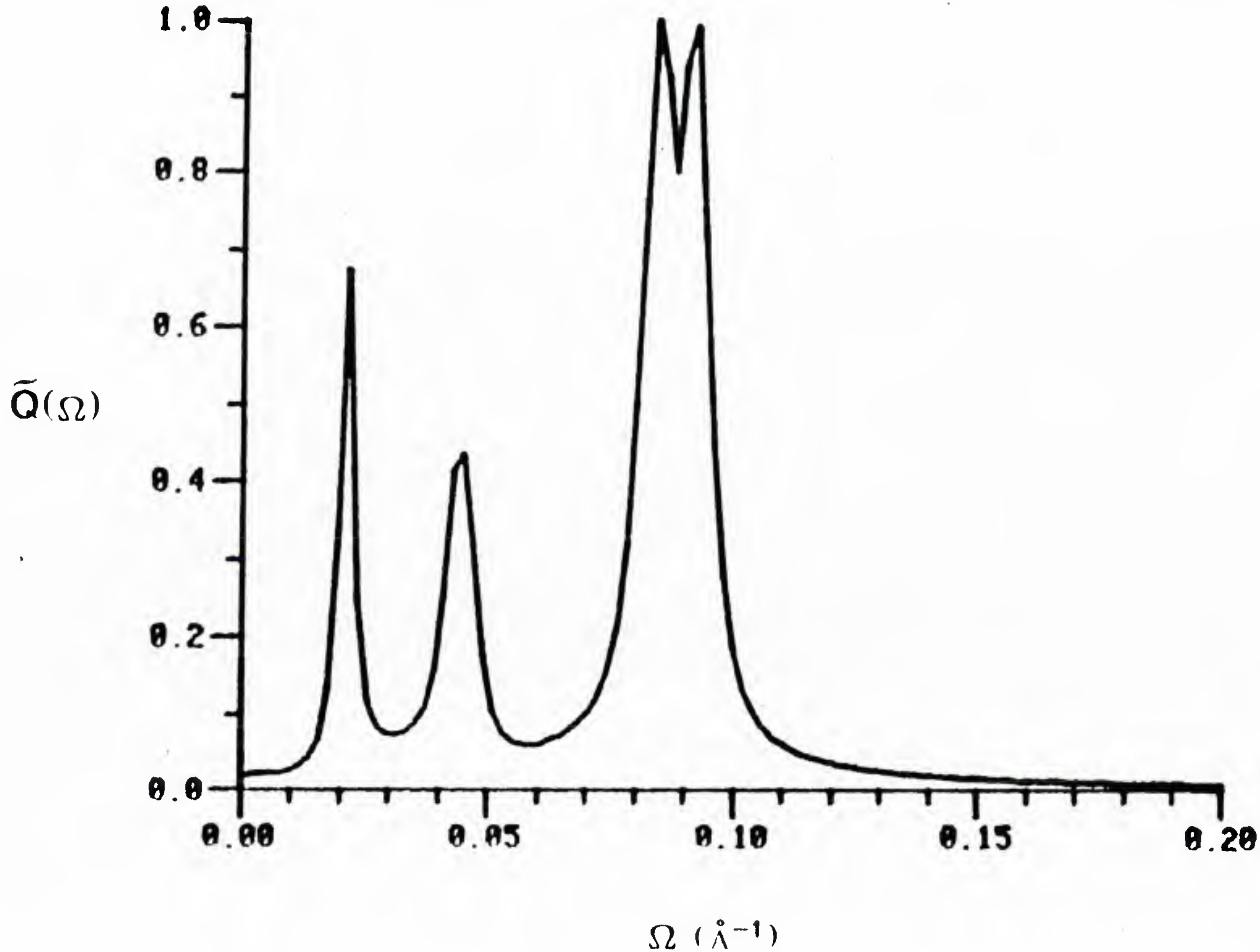

Figure 16. Spectrum of a Single Bend. Core Contrast Quadratic Dispersion Causes Ripple in the Principal Spectrum Feature. Fiber Lengths Increased by a Factor of 5 Over Figure 4

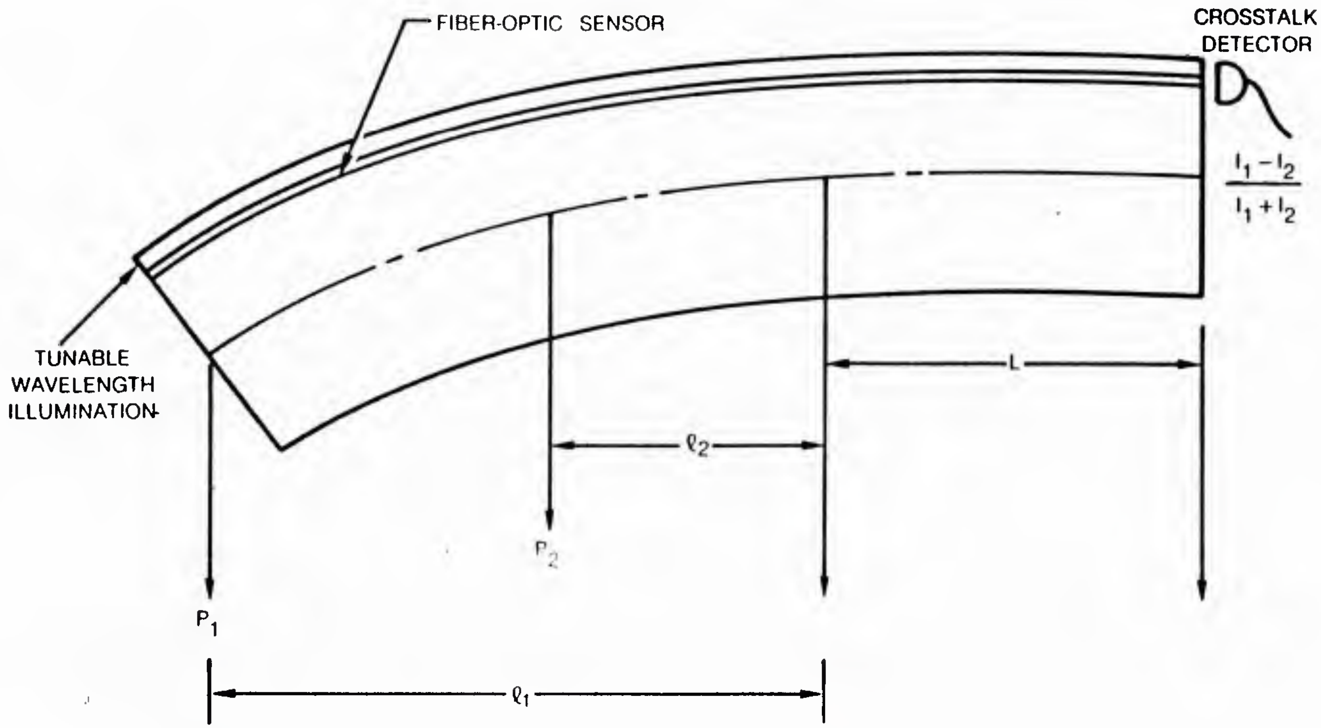

Figure 17. Distributed Strain Sensor Attached to Cantilever Beam

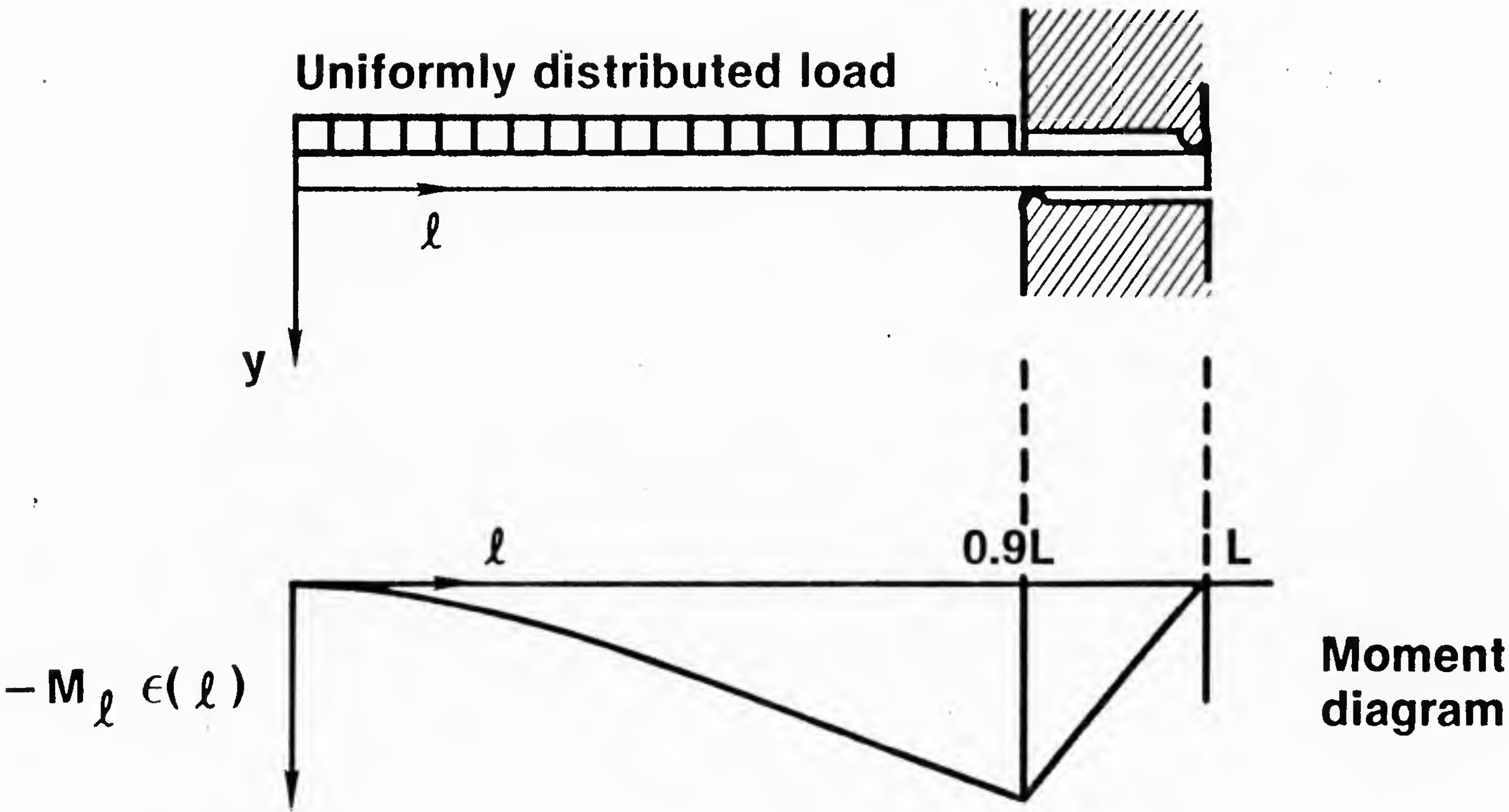

Figure 18. Cantilever Beam Geometry

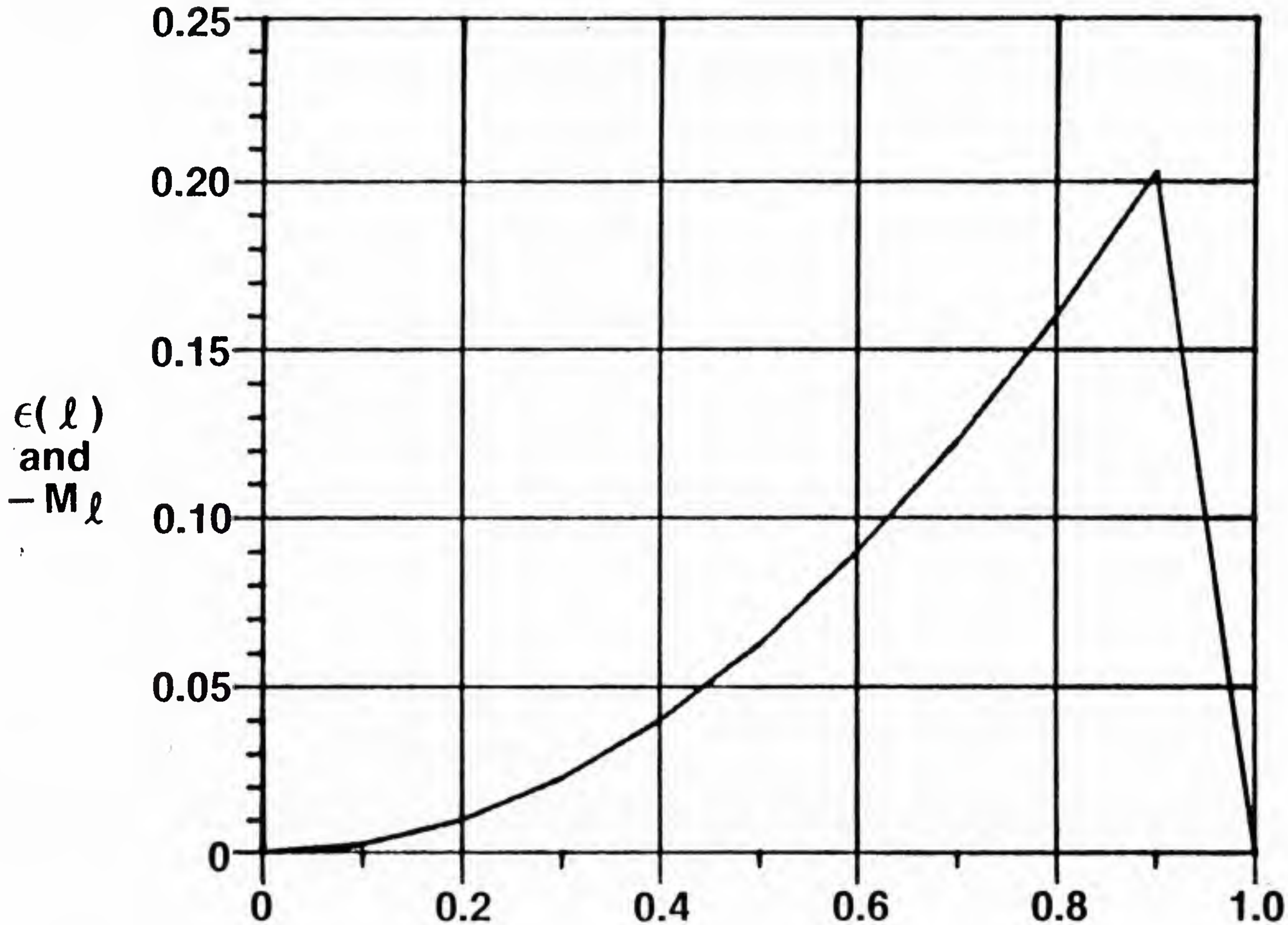

Figure 19. Moment Diagram and Strain Distribution

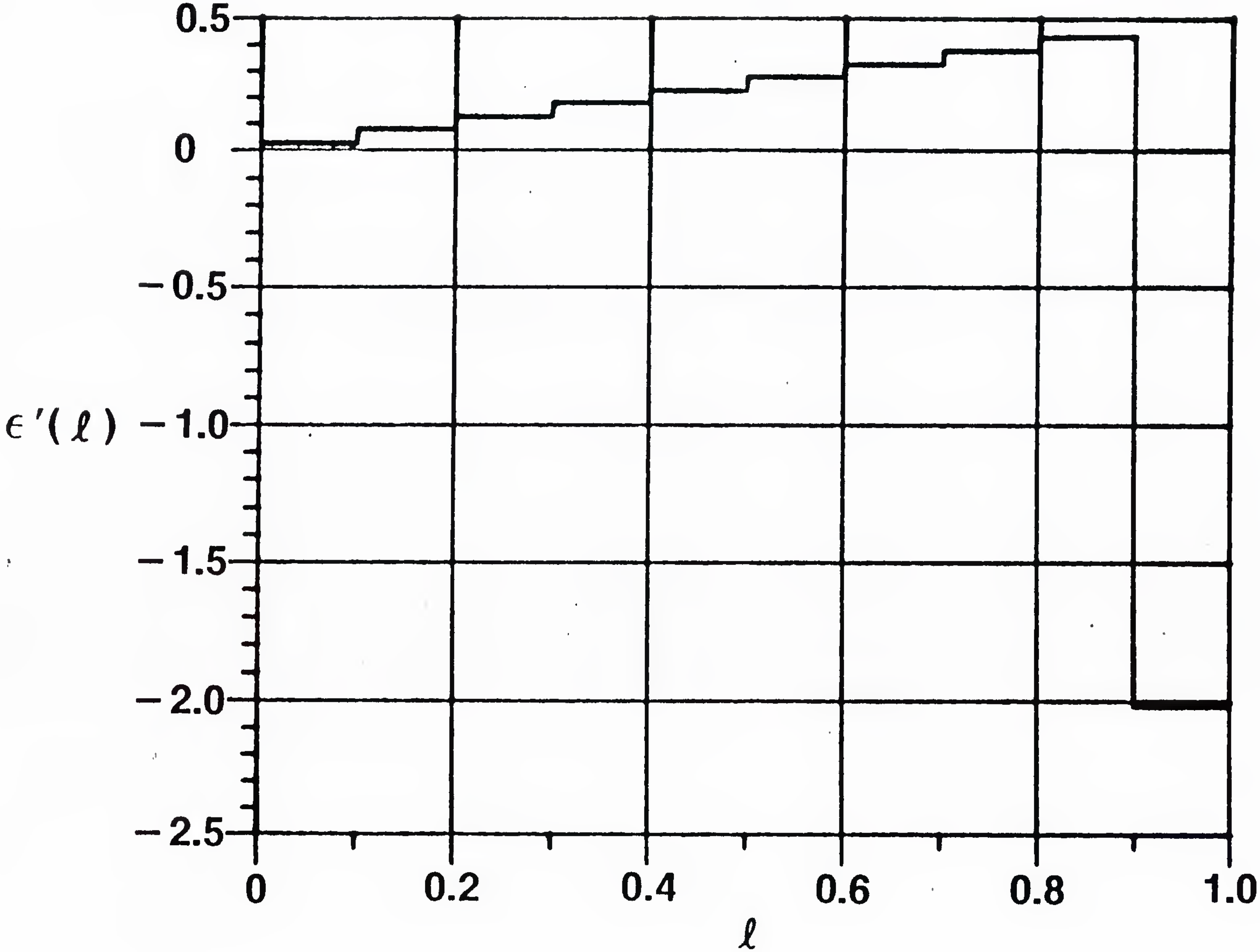

Figure 20. Shear Diagram

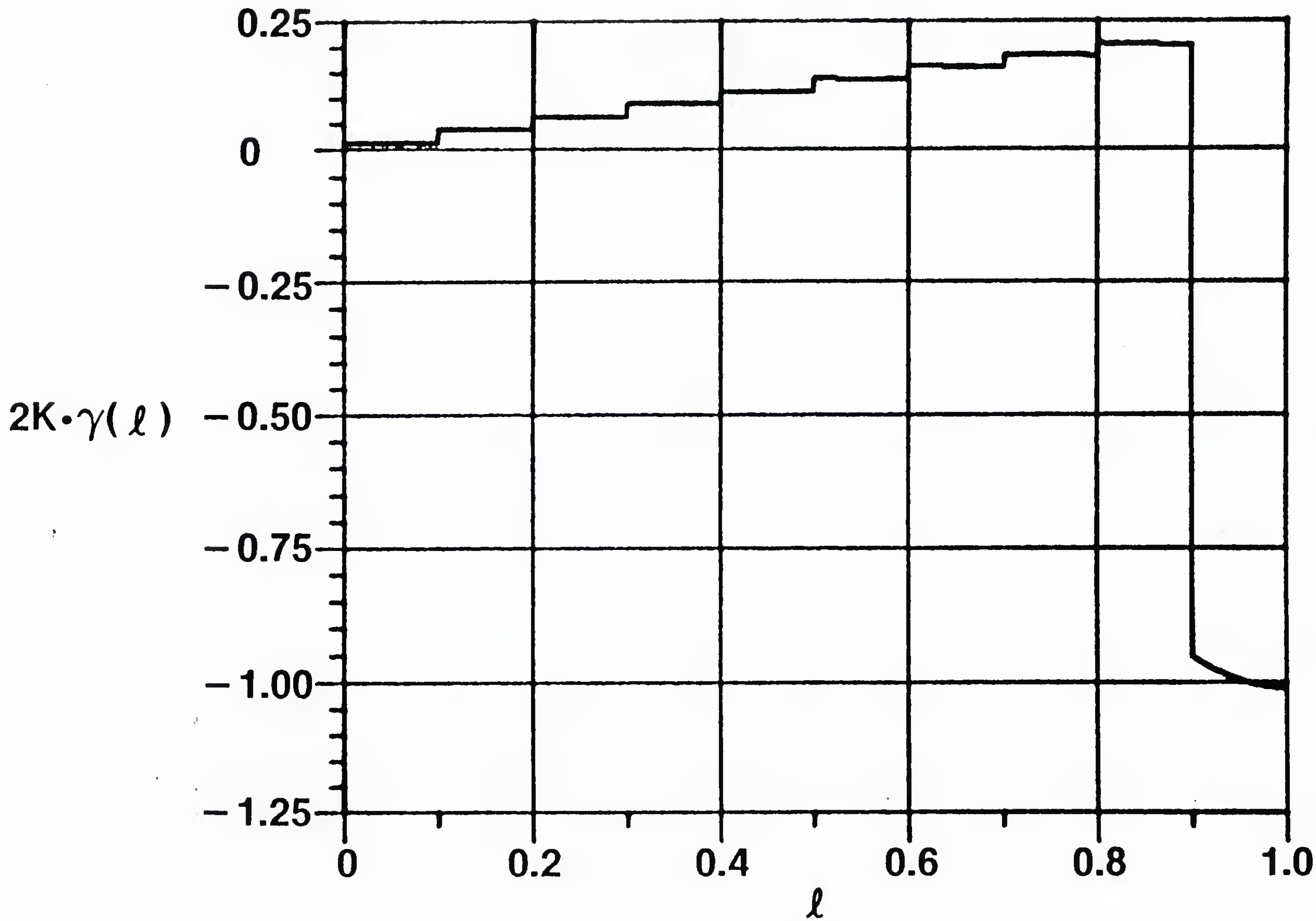

Figure 21. Variation in Mode Coupling Parameter

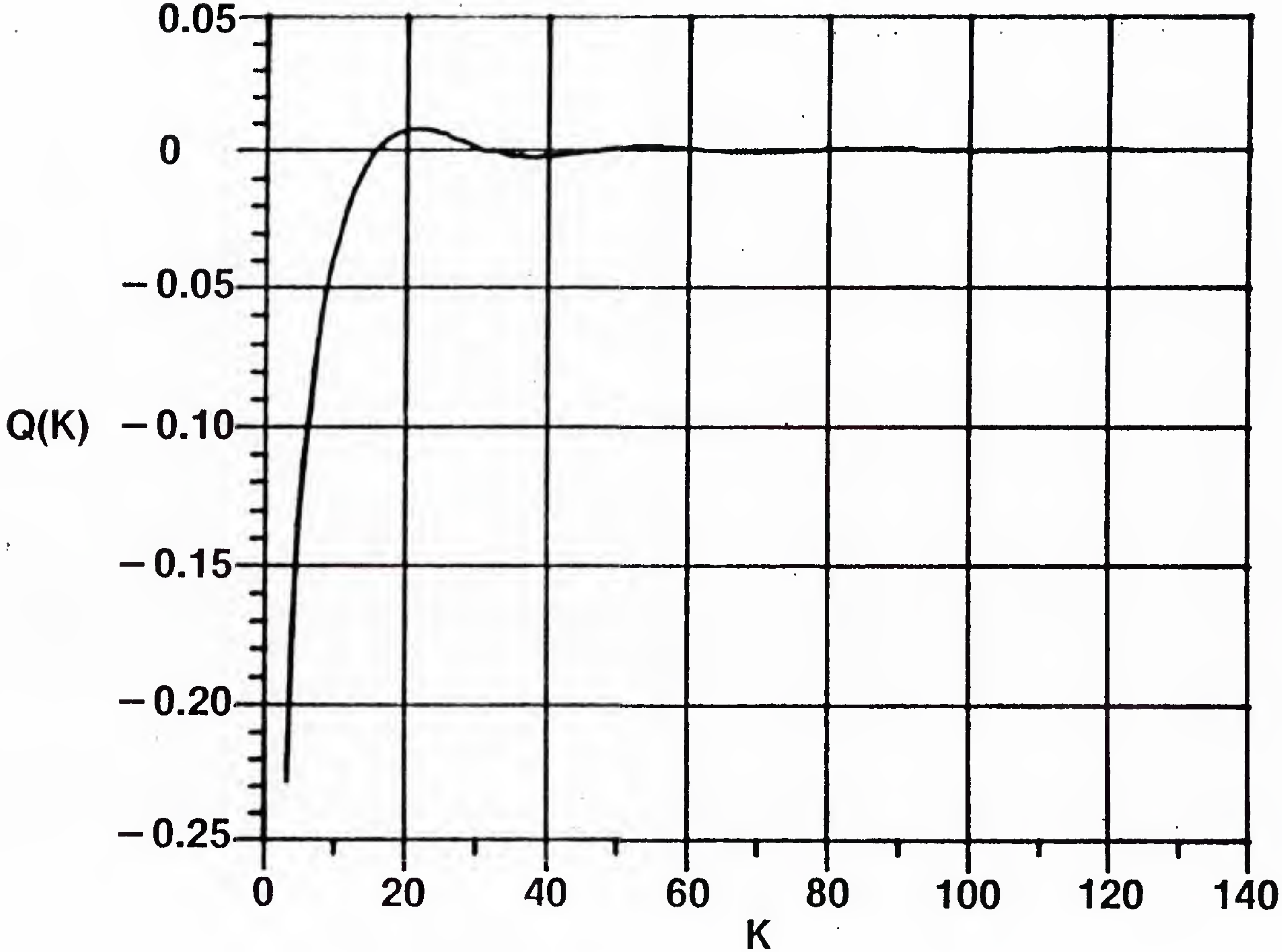

Figure 22. Crosstalk Spectrum of a Uniformly Loaded Cantilever Beam

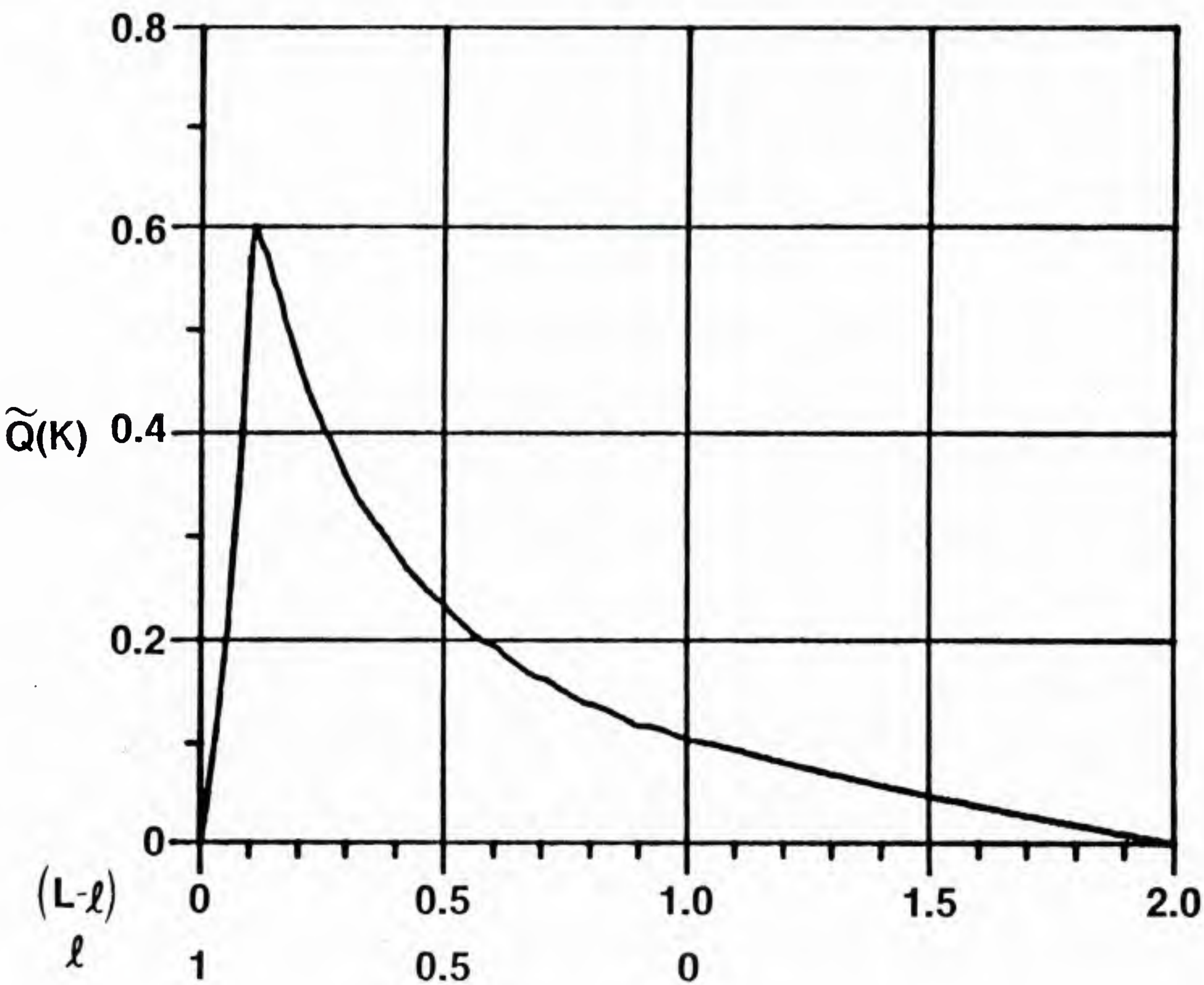

Figure 23. Sine Transform of Q(K)

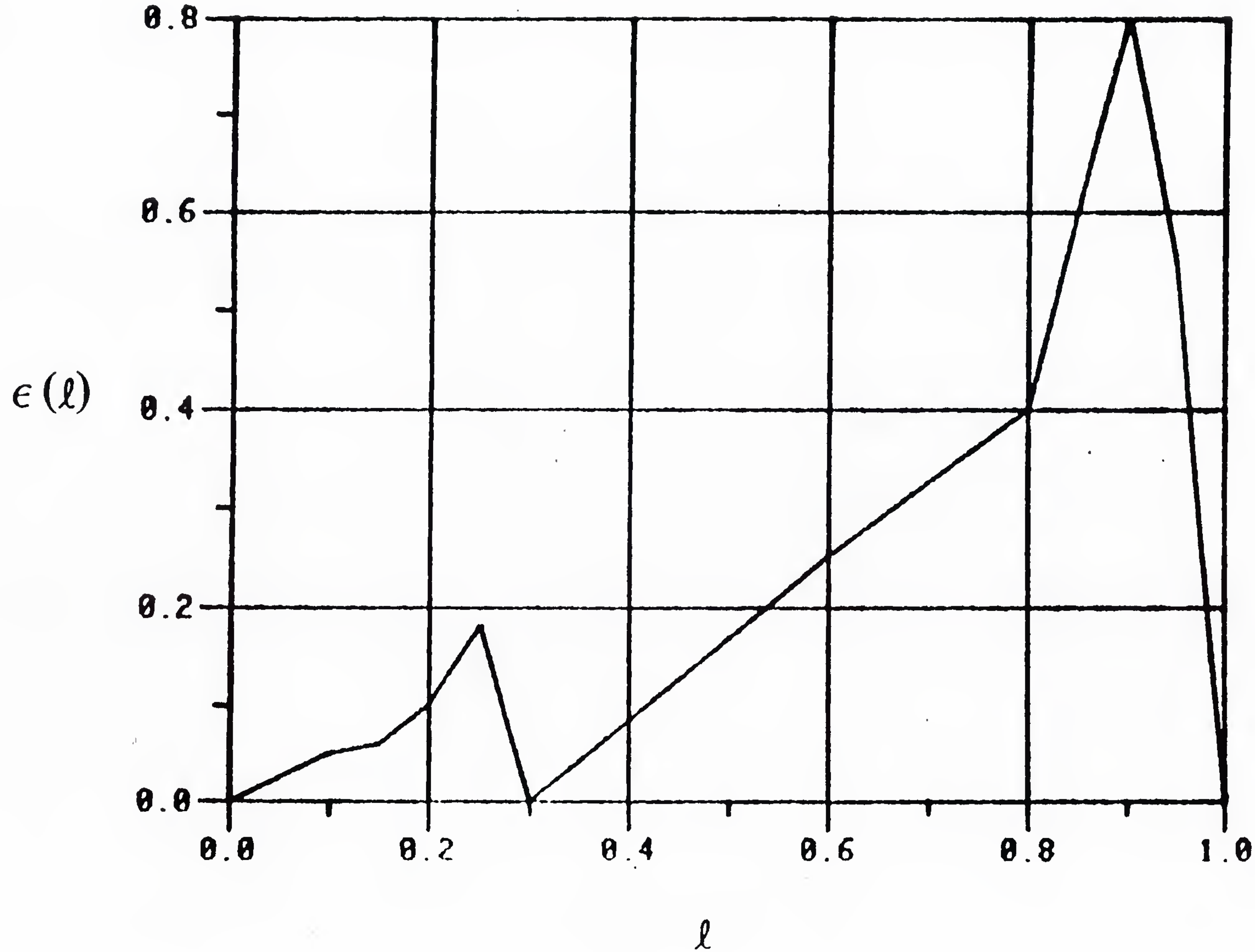

Figure 24. Strain Distribution in a Cantilever Beam With Point and Distributed Loads

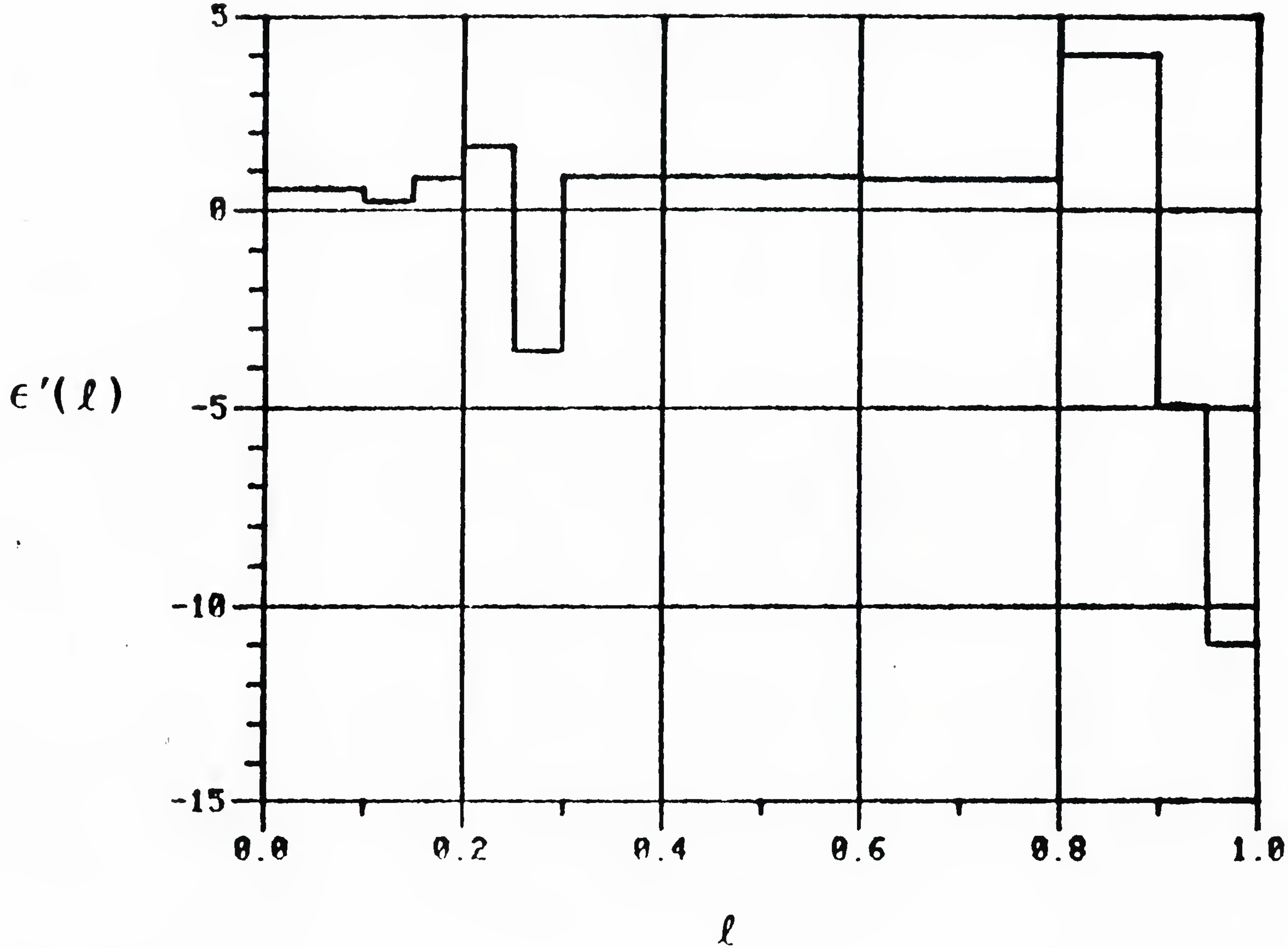

Figure 25. Shear Diagram of Cantilever Beam in Fig. 24

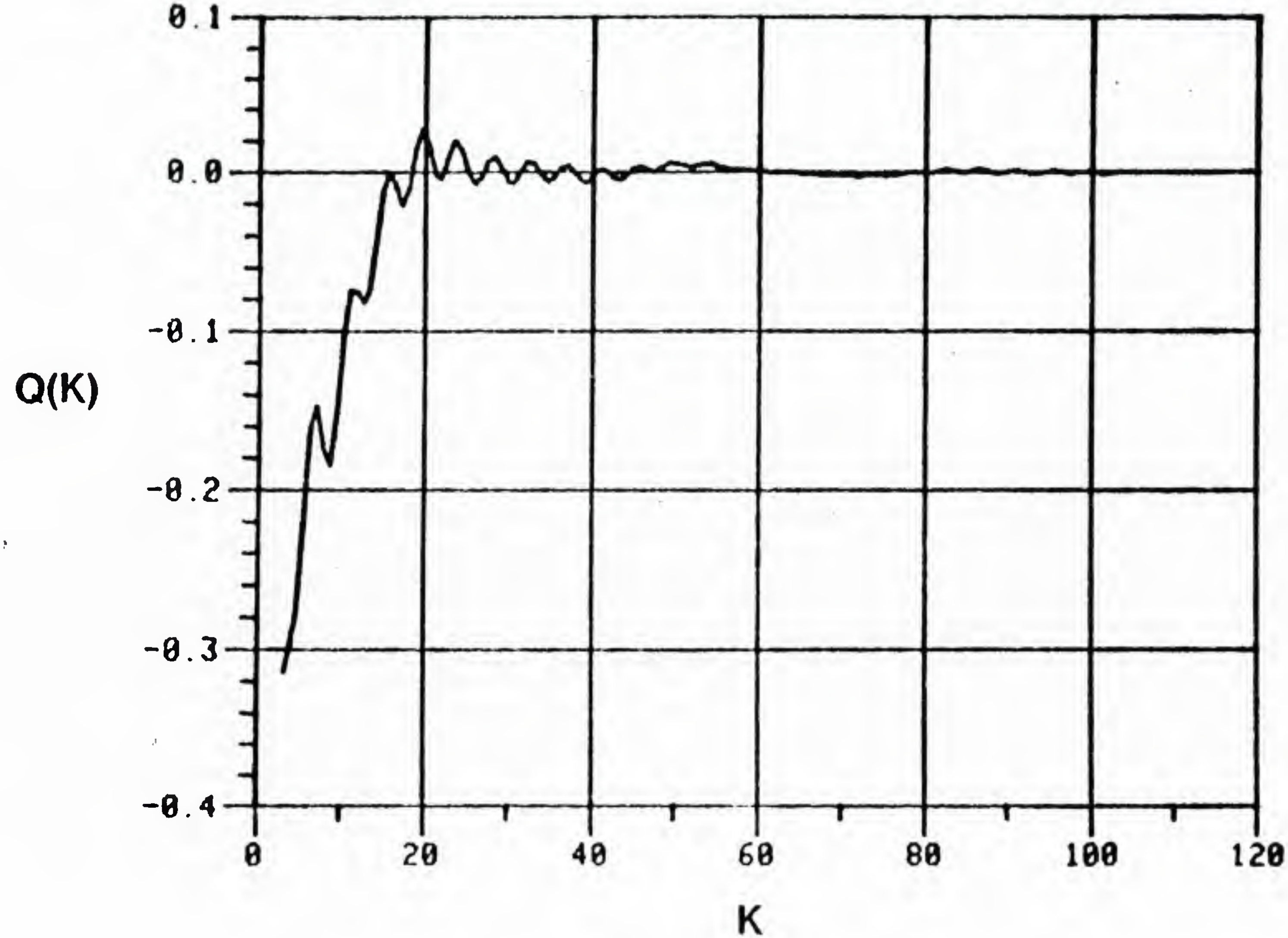

Figure 26. Crosstalk Spectrum of Cantilever Beam with Point and Distributed Loads

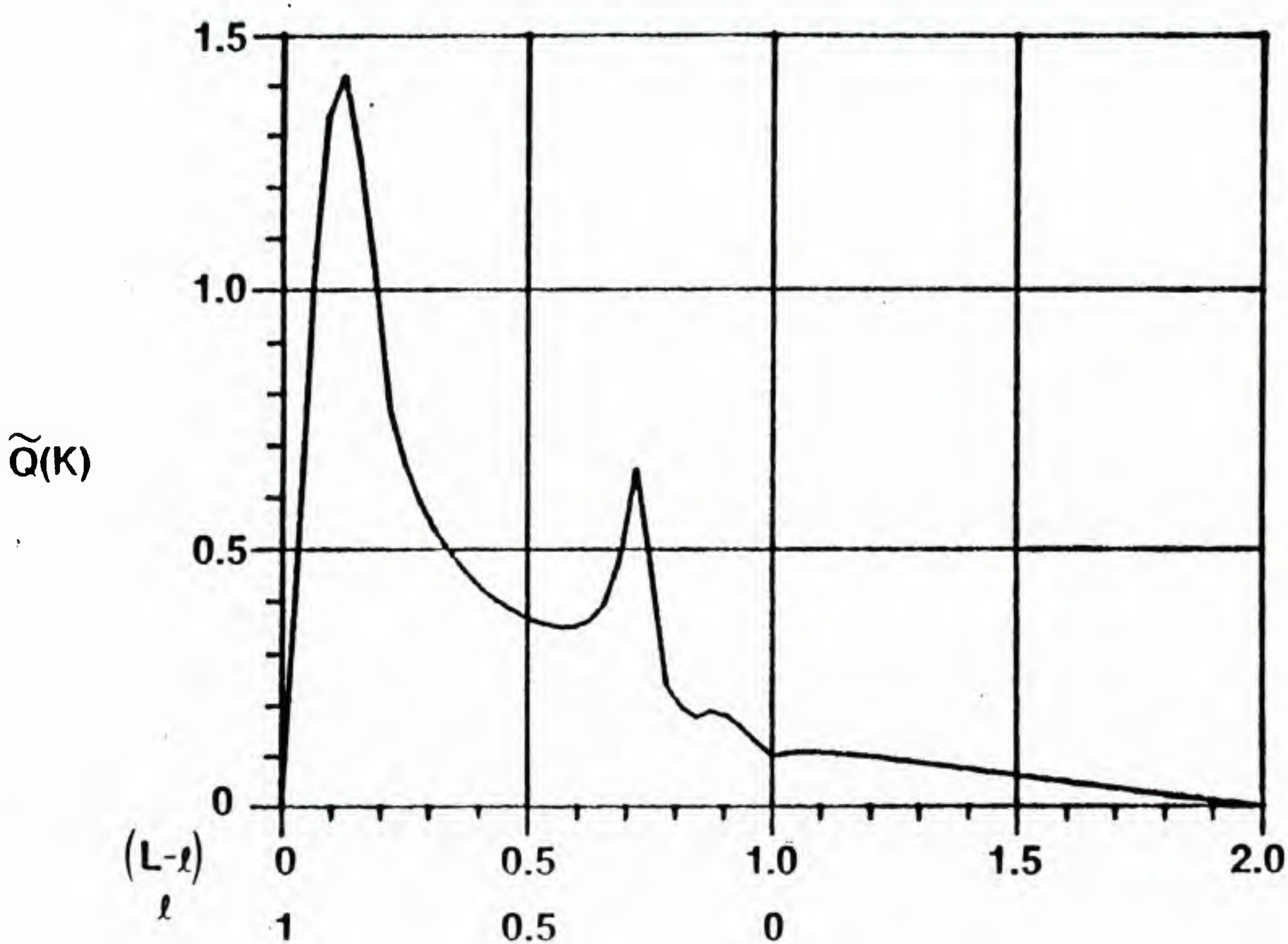

Figure 27. Sine Transform of Q(K)

Improved agreement between the inferred bending strain, as obtained from the core contrast spectrum, and the true distribution requires further processing. Only a portion of the spectrum is measured. This is equivalent to convolving the strain distribution with a sharply peaked weighting function which tends to smooth out some of the features. The relative height of the peaks in Figure 27 cannot be determined accurately since finer resolution is needed; i.e. a wider scan in K or λ. It is clear that the maximum height of the line at $\ell \simeq 0.9$ is underestimated. A number of steps can be taken to improve the accuracy of the computed strain distribution through known inverse filtering methods.

SECTION III

EXPERIMENTAL DEVELOPMENT

1. APPROACH

The fundamental measurement and signal processing requirements are shown schematically in Figure 28. The preferred implementation provides excitation of only the symmetric HE_{11} mode such that no crosstalk exists until the sensor is disturbed. However, due to the close proximity of the two cores and their intimate coupling, it is difficult to initiate this starting condition. Crosstalk is typically already in operation at the location of the bend perturbation. Conceptually, the bend perturbs a portion of the light contained in the symmetric mode and converts a large portion of the disturbed power into a wave with the propagation characteristics of the asymmetric mode. Subsequent to this interaction, crosstalk persists with a given beatlength and relative phase to the next perturbation and/or end of the sensor. Here, the normalized core contrast function is measured by collecting the power from each core, subtracting them and then dividing by the sum: (P1-P2)/(P1+P2). This parameter defines Q which is recorded as a function of the excitation wavelength. When the wavelength scans through a range of values, Q switches between +1 and -1 in reaction to a resulting change in beatlength and phase of the crosstalk function. This provides Q as a function of the beatlength. When this last function is transformed, it yields a power spectral density function for interpretation and comparison with the theoretical calculations. Facilities to implement this approach are reviewed next.

2. APPARATUS

The apparatus for the demonstration experiments is illustrated in Figure 29. A pulsed dye laser was configured as the variable wavelength excitation source. Its bandwidth is roughly 0.01 nm which is sufficiently narrow to alleviate averaging effects during experiments with long sensor lengths (on the order of one meter long). Typical monochrometers would not have provided sufficient signal to noise ratio, in addition to imposing a requirement for uselessly short sensor lengths. Light is transferred to the sensor via a modified microscope.

The twin-core sensor is mounted on a special platform used to impose various bending configurations. Holders with positioning adjustments were constructed to permit proper excitiation and constraint without imposing artifacts in the data. These holders represent the fiber termination points before and just after the bend interaction. The various perturbations, examples of which are identified in Figure 30, were arranged by placement of several forms and orientation of the detectors. Identical detectors with integral preamps were separately illuminated by images of the sensor output cores after dissection by a first-surface

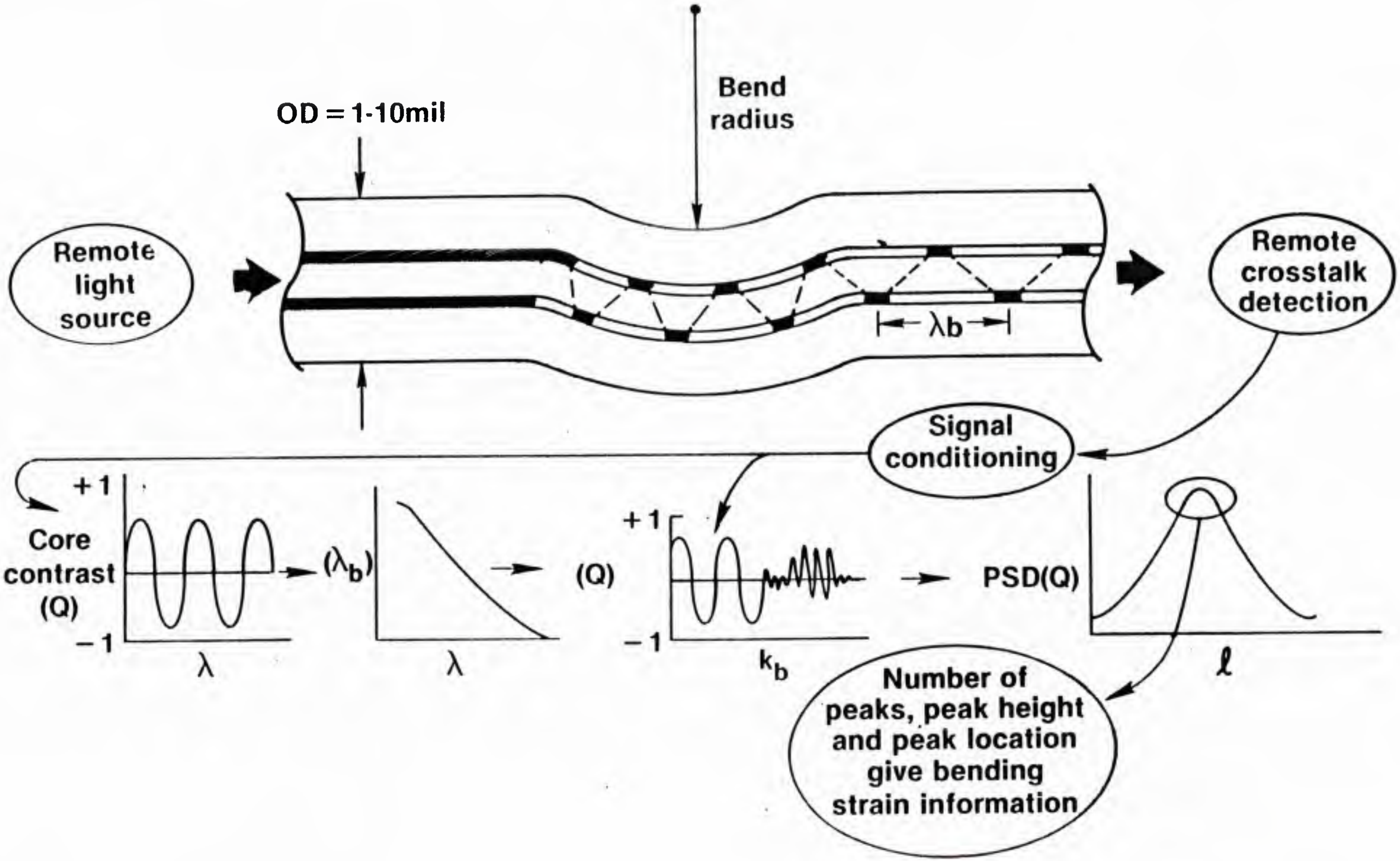

Figure 28. Measurement Concept

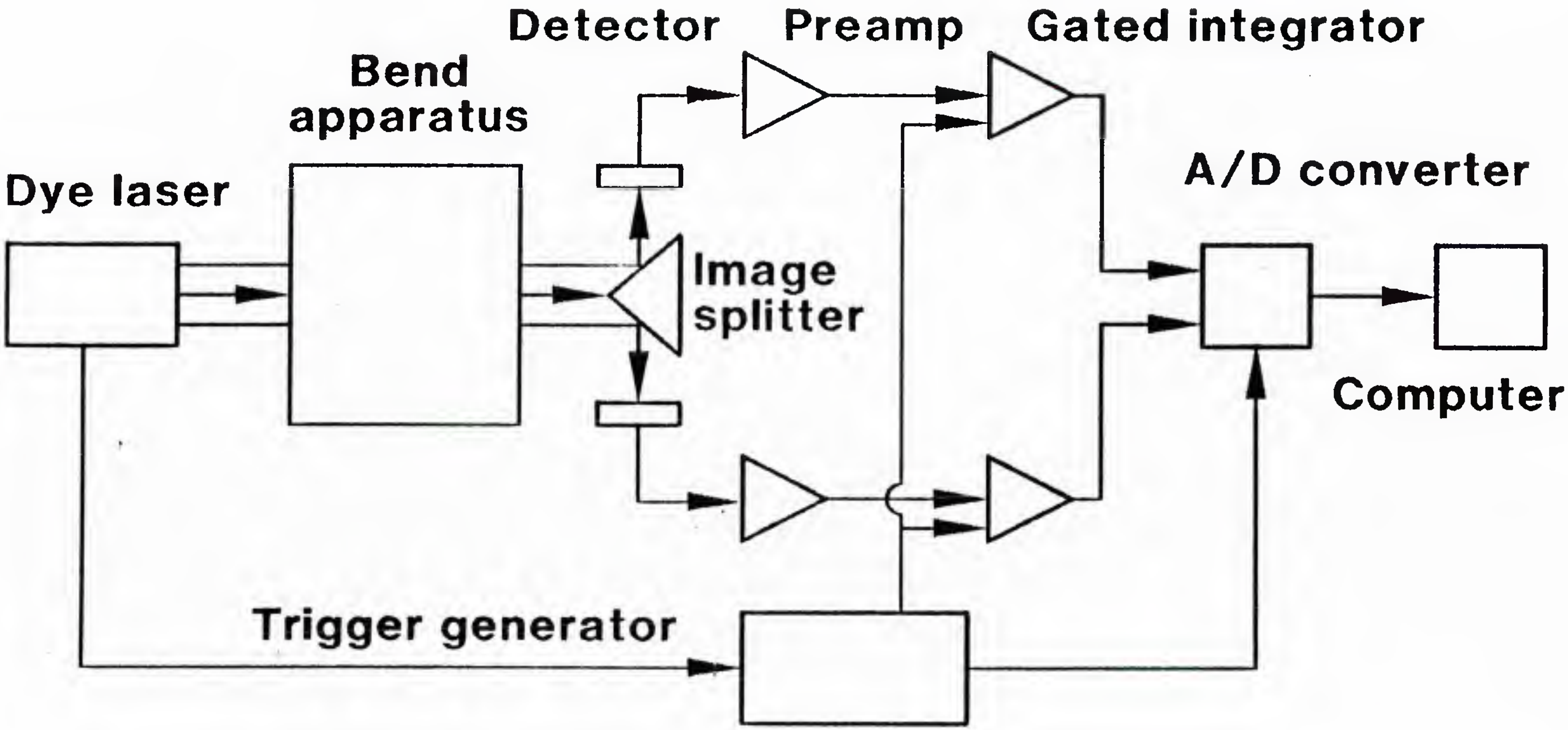

Figure 29. Demonstration Experiment: Data Acquisition System

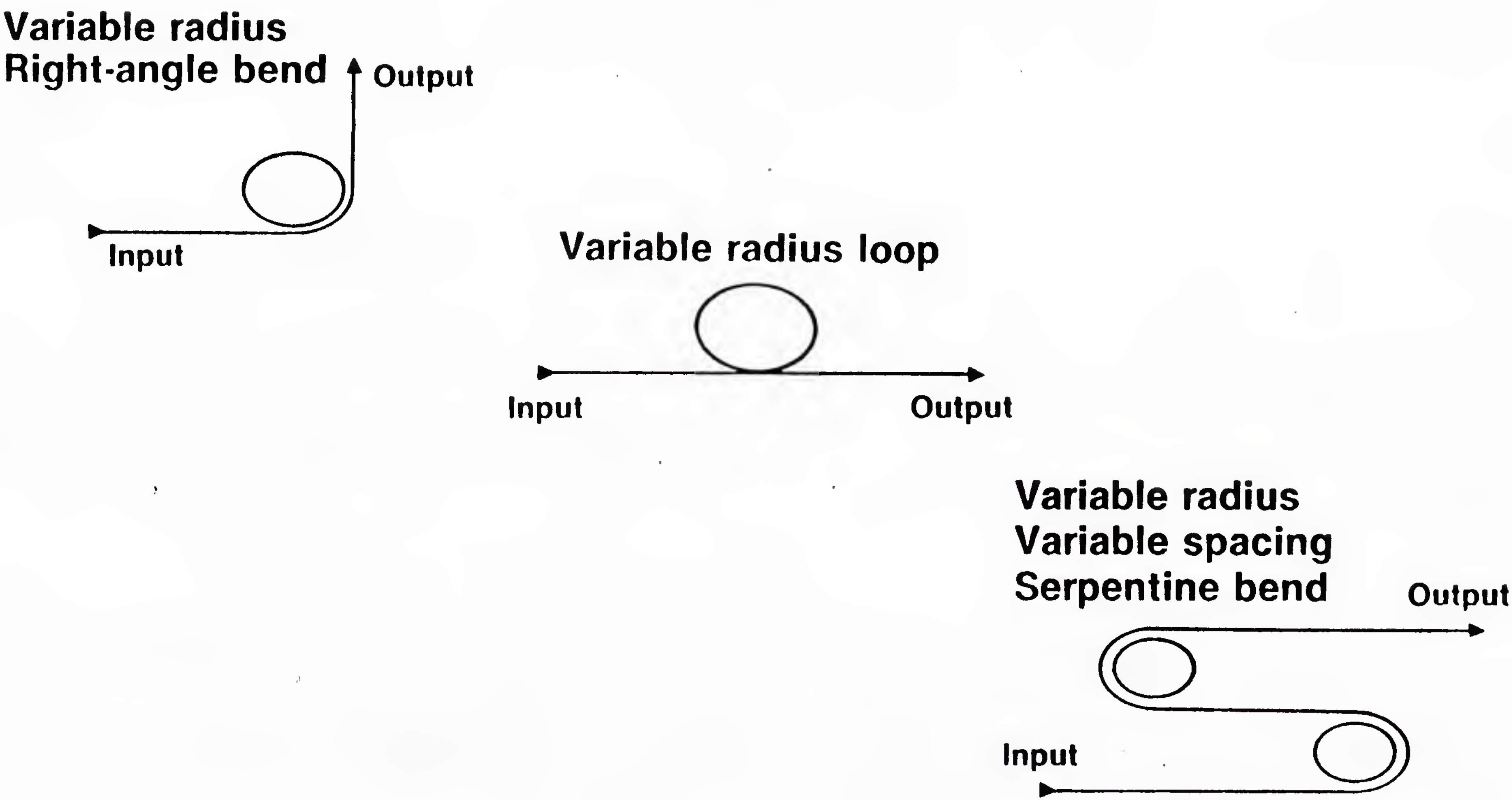

Figure 30. Demonstration Perturbations

splitting wedge. The total energy emitted from the individual cores was measured for each dye laser pulse by utilization of gated integrator circuits synchronously locked to the laser trigger generator. A Tektronix digital processing oscilloscope provided data previewing functions as well as analog-to-digital conversion for acquisition of the crosstalk signals by the PDP-11 computer. Representative measurements are discussed in the following sections.

3. PHASE-II DATA AND COMPARISON WITH THEORETICAL MODEL

a. Introduction

An initial set of measurements (Phase-I Data) was conducted with an original supply of fiber sensors. As work progressed, deficiencies were observed. Much of the data suffered from low signal-to-noise levels, making it difficult to detect predicted component peaks in the crosstalk spectrum which were to be imposed by the perturbations. In addition, many significant, unanticipated signals were recorded. Such problems made the data difficult to interpret and nearly impossible to compare directly with the theoretical model as it originally existed.

These difficulties are not seen as fundamental compromises of the sensor concept under development in this program. The physics used to formulate the predictions have a firm foundation. On the other hand, defects were hypothesized as being associated with the fiber sensor and/or the experimental implementation causing the measurements to differ from the assumptions used to develop the theory. In addition, the theory required generalization to yield a comprehensive representation of the predicted results. With these issues at hand, the earlier results are presented in Appendix A.

Theoretical and experimental improvements described in Appendix B were implemented to provide an enhanced set of measurements (Phase-II Data) with corresponding calculations. The tests were conducted on a variety of bends with geometries similar to those of Phase-I experiments. Every sensor was inspected to alleviate problems associated with control of dimensions or inclusions. Mounting procedures were given careful attention, and data was collected with the new sampling and range parameters. Finally, the calibrated, theoretical model (upgraded to include dispersion effects) was successfully compared with many of the measurements.

b. Right Angle Bend

Figure 31 illustrates the crosstalk spectrum measured for a relatively short sensor subjected to a right angle bend. The same figure compares the predictions from the new model. The theoretical predictions provide the proper, unperturbed

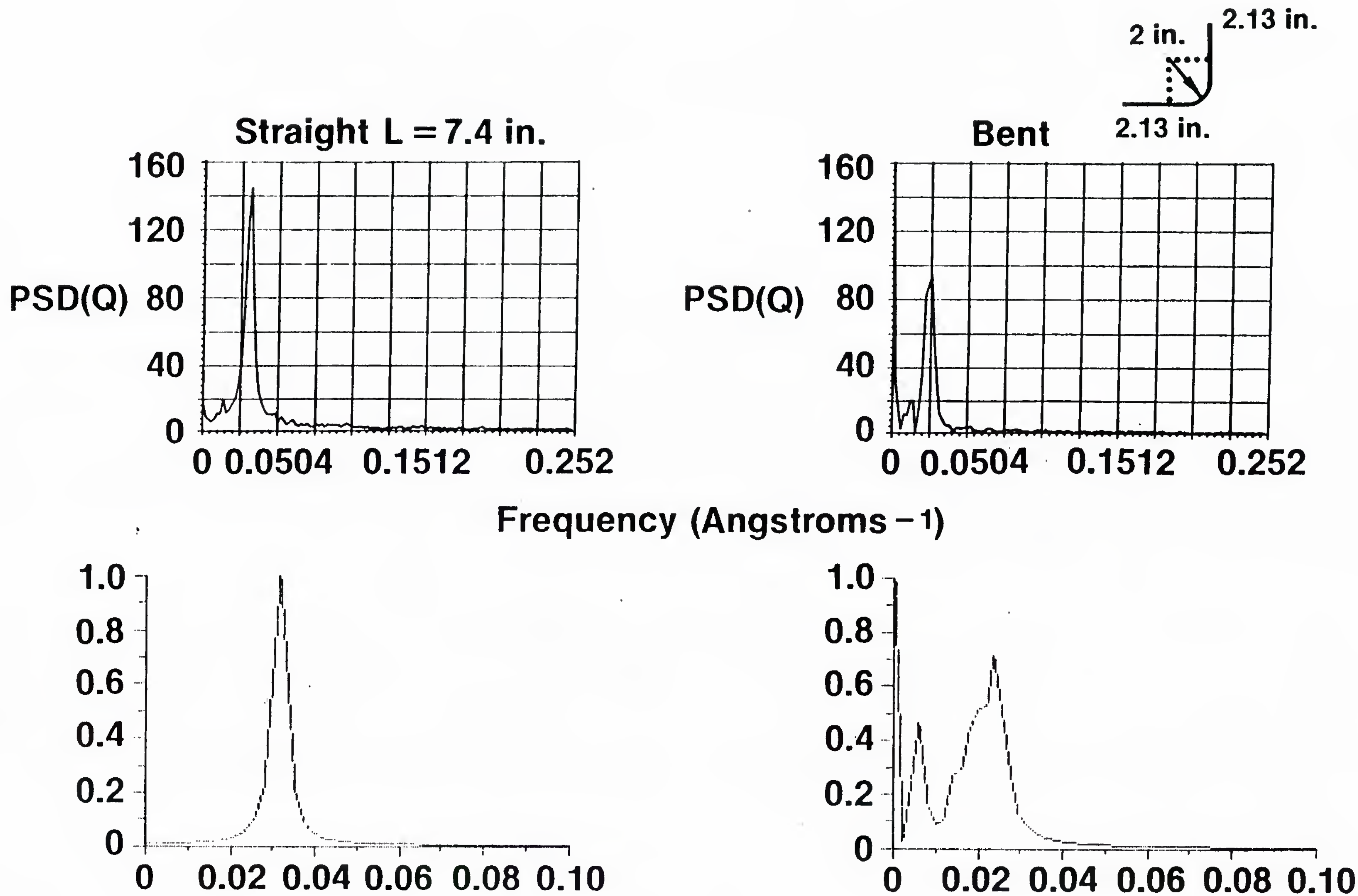

Figure 31. Phase II: Short Right Angle Bend. Sample A04.5SQC/ 11.27.29

sensor carrier frequency. The modified spectrum for the bent sensor is also replicated by the general form of the calculations.

To obtain examples depicting the comprehensive capabilities of the model, measurements were performed with a much longer sensor. These results are summarized in Figure 32 for a straight reference case and two bend conditions. The complexity of the experimentally derived signatures increased when compared to the measurements with a shorter device. As observed on the undisturbed carrier frequency, dispersion related effects became more dominant but were quite well represented in the calculations. Some adjustment of the input conditions for the calculations was required to obtain trends similar to the experimental results of the perturbed states. The range of adjustments, typically 10 percent, were reasonable for the current effort. For instance, an important issue arose with respect to Figure 32 which illustrates the sensitivity of the twin-core sensor to initial conditions. The center spectral feature could not be computed without hypothesizing some imbalance (1.2 percent) in the amount of power distributed between the symmetric and asymmetric modes. Such an imbalance could occur during the experiments if a small amount of excitation energy spilled from the Airy disk illuminating Core 1 and excited Core 2. This situation might arise if a small amount of mechanical drift should develop during the measurements or if a slight defocus of the excitation beam should exist. Standard procedures call for alignment and focusing checks prior to all measurements, however a slight error of this type obviously materialized and remained uncompensated. This aspect would have been difficult to diagnose in the laboratory, yet was easily tested with the model.

c. Single Loop

A bend configured into a complete loop yields a much more difficult test condition. The crosstalk perturbations become stronger and more complex. Figure 33 is an example which indicates that much fine structure becomes generated in the crosstalk spectrum. The detailed features appear sensitive to many secondary aspects of the experiment. This can be illustrated by referring to the theoretical predictions. The model calculations contain the important main components. For instance, dispersive broadening of the primary carrier is shown along with its shift to a lower frequency after bending. The main feature just below .05 (1/Å) in the measurements is also found in the model. However, the finer details of the laboratory data above and below this component are not provided with as much fidelity in the corresponding calculation. All of the important secondary features exist but not with the proper relative magnitudes. Finally, small changes in the model parameters yield small but important changes as typified by Figure 34. The distributed strain sensing scheme with a twin-core sensor requires further study to help immunize it from these sensitivities.

A change in core geometry, discussed in the next section, was investigated as a possible variable in this sensitivity issue.

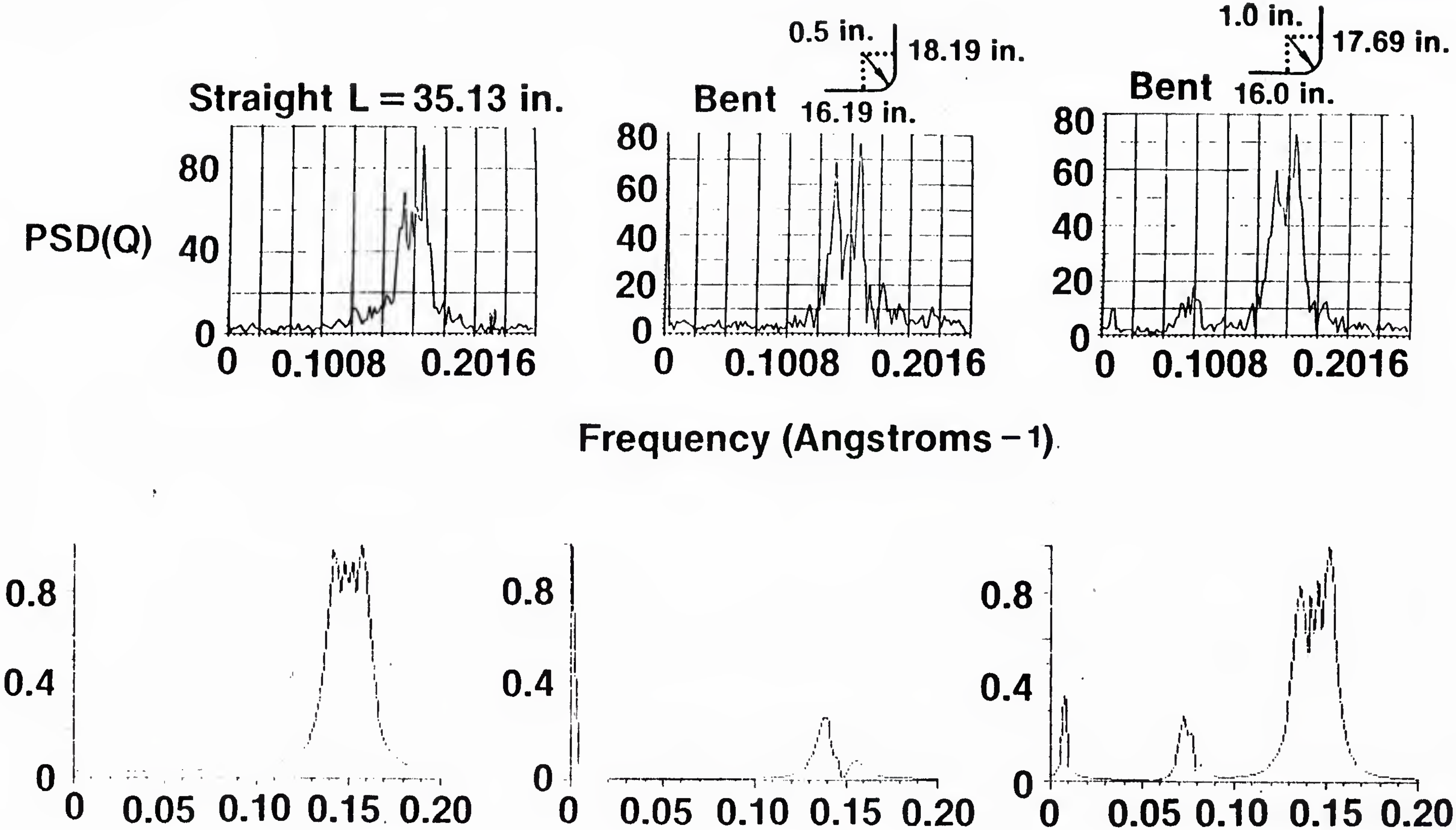

Figure 32. Phase-II: Long Right Angle Bend. Sample A04.5SQC/ 7.25.8.2

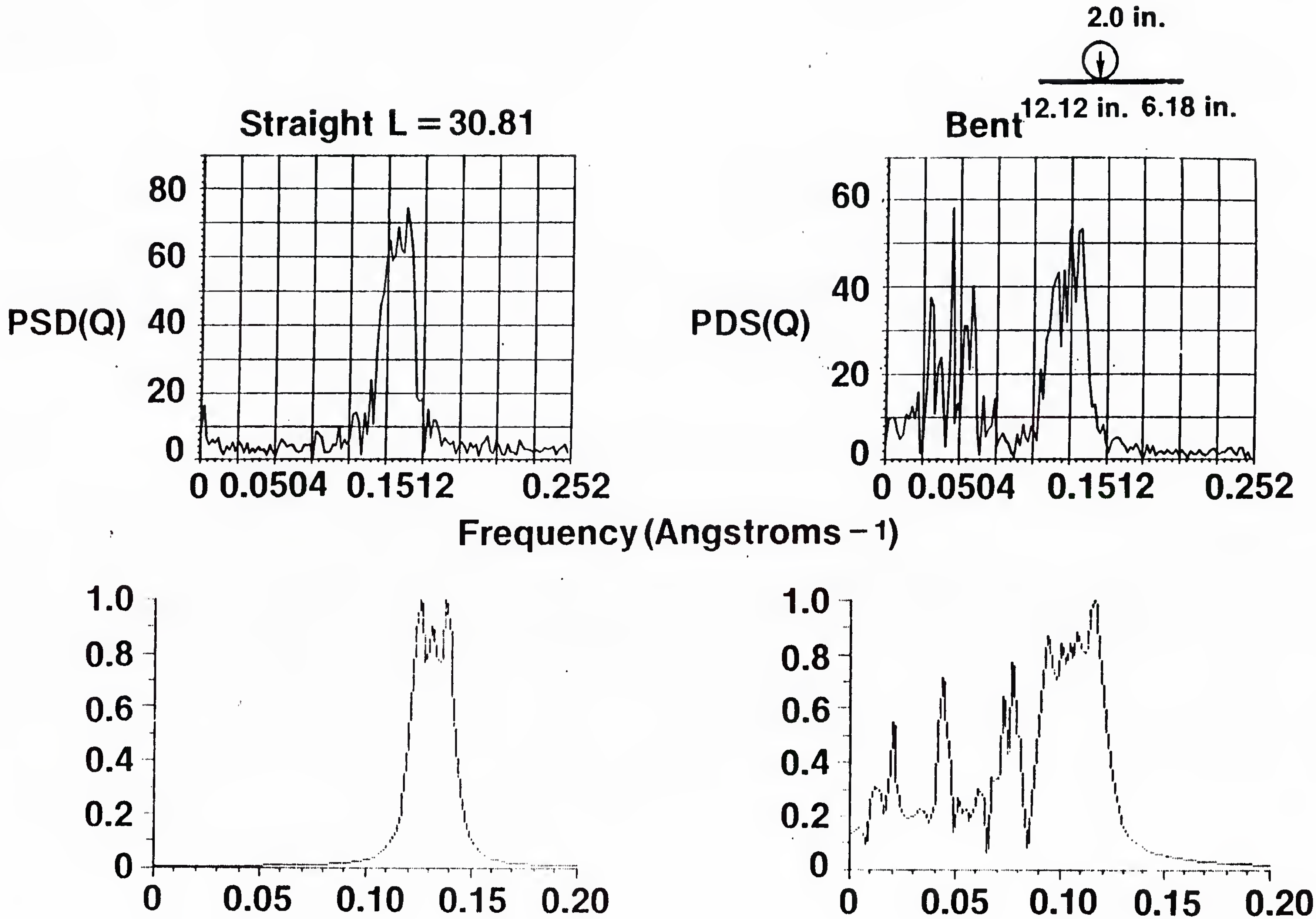

Figure 33. Phase—II: Single Loop. Sample A04.5SQC/12.18

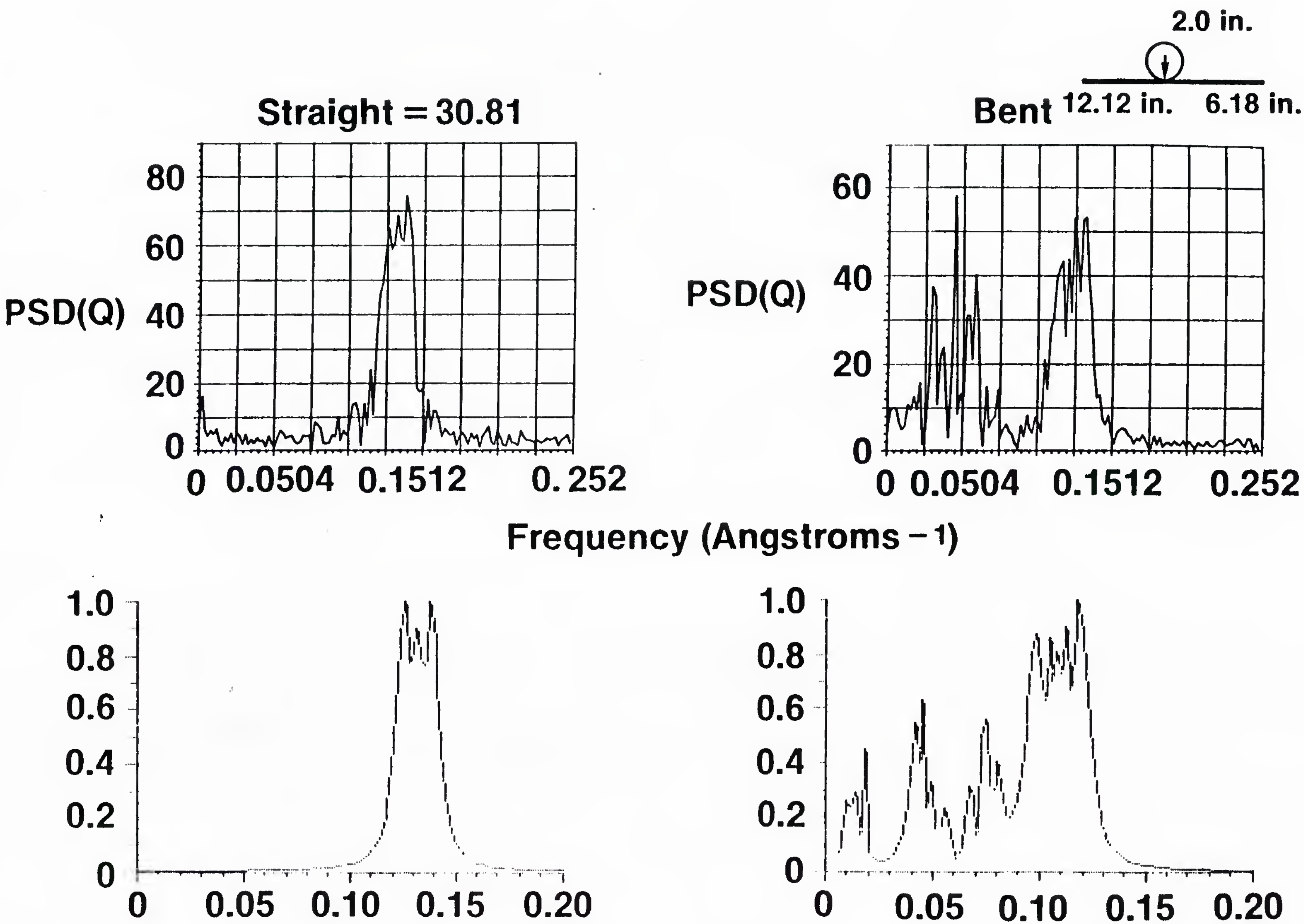

Figure 34. Phase-II: Single Loop. Sample A04.5SQC/12.18

d. Round-Core Sensor

The square-core sensor geometry has been used exclusively in the all major demonstrations discussed to this point. A square configuration was the primary subject of interest because of apparent high sensitivity to bending strain observed in early, qualitative tests. Now, we would like to reduce some of the sensitivity, so a round-core sensor alternative was investigated. Figure 35 illustrates performance of the round configuration during a right angle bend. Theoretical modelling of the experiments shows good correlation with the measurements. Furthermore, numerical tests showed no fundamental difference in the sensitivity of the round-core device when compared with the square geometry. Therefore, we conclude that other parameter changes must be implemented to alleviate the critical nature of the twin-core response to its operating conditions.

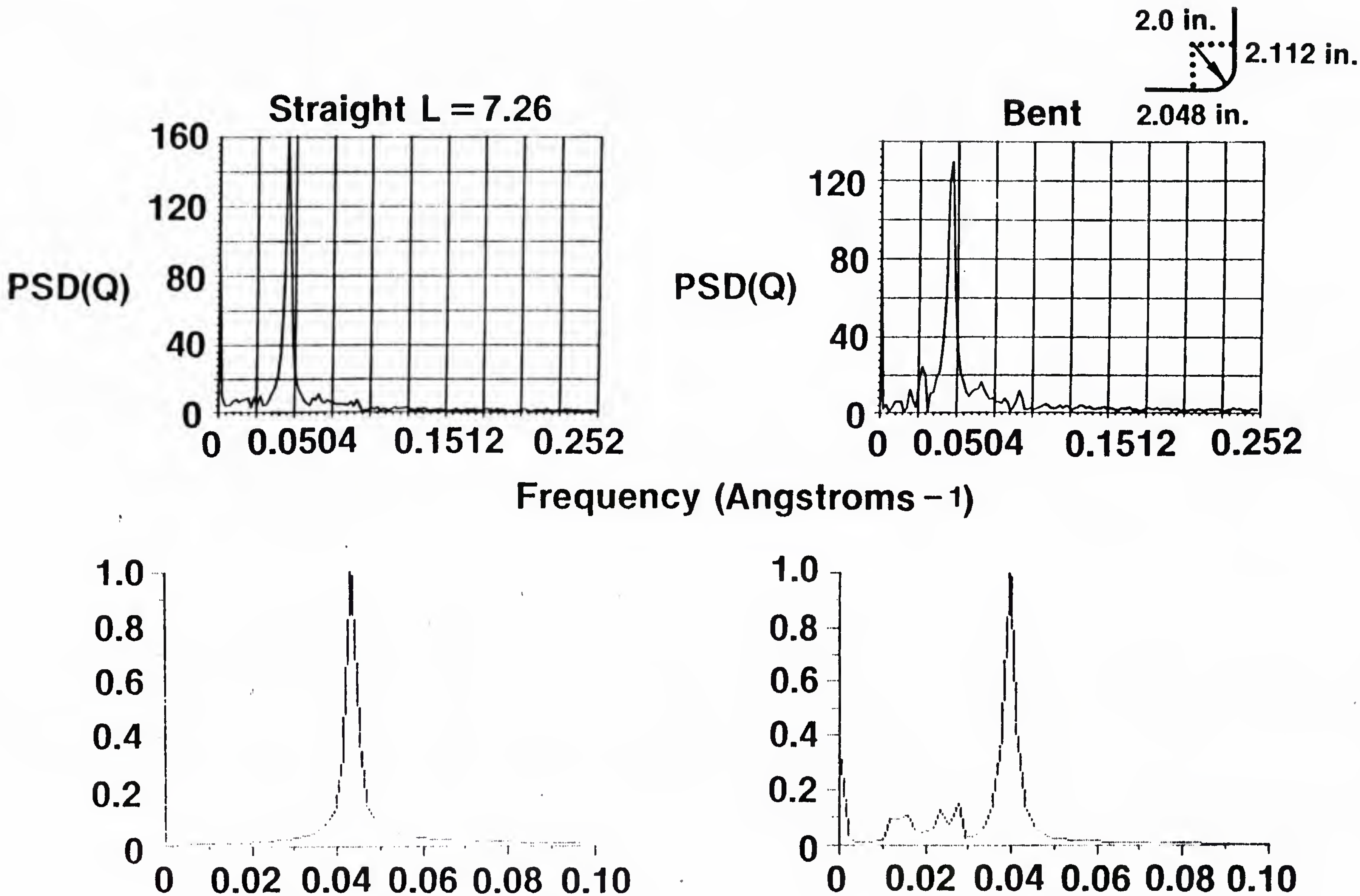

Figure 35. Phase–II: Right Angle Bend; Round Core. Sample AORDC/12.5.6

SECTION IV

SUMMARY AND RECOMMENDATIONS

This document discloses the investigation of a unique concept for measurement of distributed strain. Implementation of the technique utilizes a fiber optic device with twin, coupled cores, a single input and a single output. Multiple wavelength operation of the sensor yields a diagnosis of the waveguide coupling perturbations imposed by mechanical disturbances. A general theory for the device has been derived in the form of an integral equation that connects the sensor core contrast to an arbitrary bending strain or curvature. In many cases of interest the curvature is small and slowly varying. For these conditions theory shows that the crosstalk spectrum is directly related to the Fourier transform of the strain distribution on a cantilevered beam. This result pertains to a wing with gradual bends (radius of curvature large compared to arc length) while stipulating very practical requirements on potential sensor parameters (radius of curvature large compared to device beatlength). The experiments summarized in this report confirm the theoretical predictions.

Two computer models were developed from the theory. One model provides a rudimentary simulation of a wing (cantilevered beam). It was used to prove that the Fourier transformation of the simulated sensor output matched the bending moment distribution. The second model was created to calculate the sensor response for comparison with the demonstration experiments. Complete spectral distributions were provided. Another important feature of this second model was that it could be adjusted to match laboratory sensor calibration data for absolute beatlength and dispersion, thereby improving correlation between theory and experiment.

Fiber optic devices were designed and fabricated for laboratory-scale tests. Sensor performance was diagnosed by techniques established in direct support of these demonstrations. Verification experiments performed with simple bending perturbations in the laboratory apparatus exhibited complex spectra and low signal to noise results during Phase-I. In addition, the form of the theory provided only spectral feature designation, not a complete distribution with properly registered magnitudes. Both of these issues were resolved during Phase-II. Finally, the improved sensors and experimental conditions confirmed the general form of the sensor spectra predicted by the model.

Both the theory and the experiments indicate that the twin-core device is highly sensitive to its mechanical environment and its operating conditions. Small modifications to the relative power content for the symmetric and asymmetric modes at the input caused significant changes in the crosstalk spectrum. Similar results were observed for changes in the form of the beatlength versus

wavelength scanning function. The crosstalk spectrum responded in a sensitive way to changes in the absolute beatlength range and dispersion in the function. Under most experimental conditions the sensor response was so sensitive and the measured output so complex that interpretive support by the theoretical model was essential. We recommend that a new operating regime be identified for further laboratory investigation. The new conditions must be identified through analytic and numerical development directed toward desensitizing the experimental devices and reducing the complexity of their responses. Changes in both the device parameters and the experimental perturbations are anticipated. Polarization effects in twin-core sensors should also be investigated.

The basic results of this investigation indicate that the twin-core concept for measurement of distributed strain is valid. However, practical implementation with the present sensors is very complex. Further study may yield improved sensor operating regimes with corresponding simplification of its response. In conclusion, this fiber optic sensor concept requires additional investigation and development to optimize device parameters for application to distributed strain diagnostics for airframe structures.

APPENDIX A

PHASE-I DATA

1. INTRODUCTION

This initial set of measurements was conducted with an original supply of fiber sensors. As work progressed, deficiencies were observed. Much of the data suffered from low signal-to-noise levels, making it difficult to detect predicted component peaks in the crosstalk spectrum which were to be imposed by the perturbations. In addition, many significant, unanticipated signals were recorded. Such problems made the data difficult to interpret and nearly impossible to compare directly with the theoretical model as it existed at this point.

These difficulties are not seen as fundamental compromises of the sensor concept under development in this program. The physics used to formulate the predictions have a firm foundation. On the other hand, defects were hypothesized as being associated with the fiber sensor and/or the experimental implementation causing the measurements to differ from the assumptions used to develop the theory. In addition, the theory required generalization to yield a comprehensive representation of the predicted results. With these issues at hand, the earlier results are reviewed.

2. UNPERTURBED SENSOR SIGNATURE AND LENGTH SCALING

Figure A-1 provides a graph of the core contrast function which comes from measuring P1 and P2 at the sensor output as the excitation wavelength is scanned. The result is a sine-wave-like signal. Eventually, structural data will be interpreted by diagnosing the Fourier Transform of this signature. It is easy to see that when a spectral analysis (achieved by Fourier Transforming) is performed that it will consist of one primary frequency peak and miscellaneous other lower level noise signals. This insight is supported by Figure A-1, with further indication of the coexistence of a very low frequency signal. This low frequency feature was not anticipated for a benign sensor condition.

There was concern that the extra, low frequency signal resulted from sensor deflections imposed by misaligned termination units. Another sensor (Figure A-2) was tested for this effect. Evidence indicates that the sensor must exit the end mounts cleanly, without kinks in order to obtain a cleaner spectrum. To further test this aspect, another sensor, Figure A-3, was subjected to changes after the termination units were carefully adjusted.

To begin with, a very different signature was obtained for this third device. The low frequency component existed but so did a very complex structure

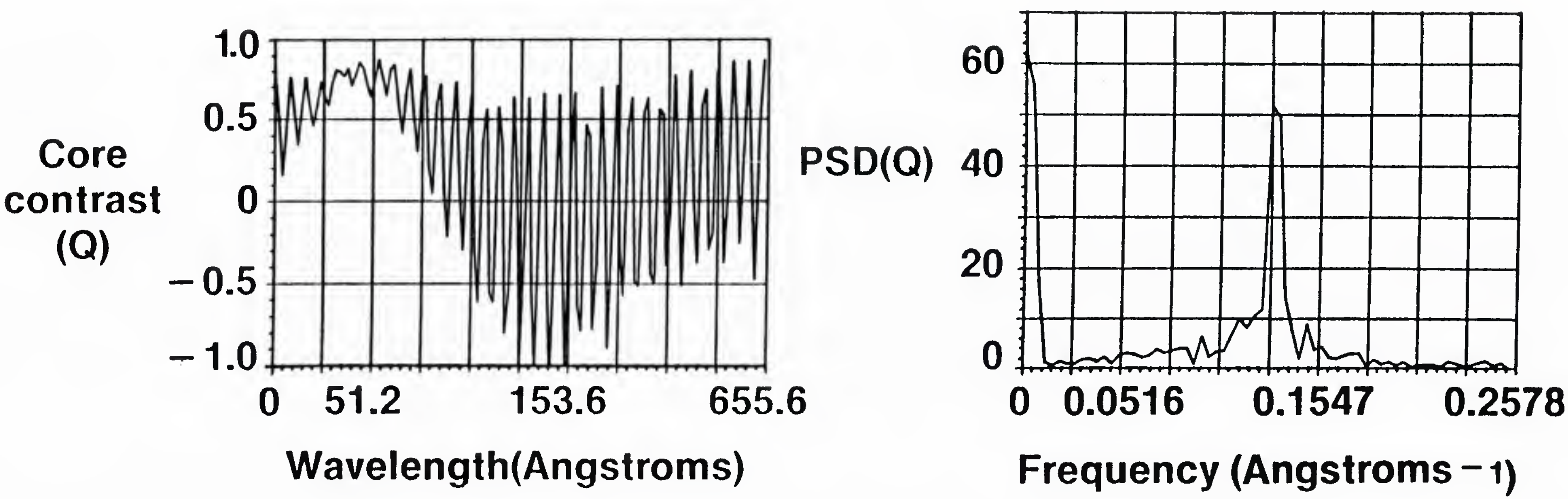

Figure A-1. Response of Straight Fiber. L=100 cm; Sample 4045QC/DSS3.141

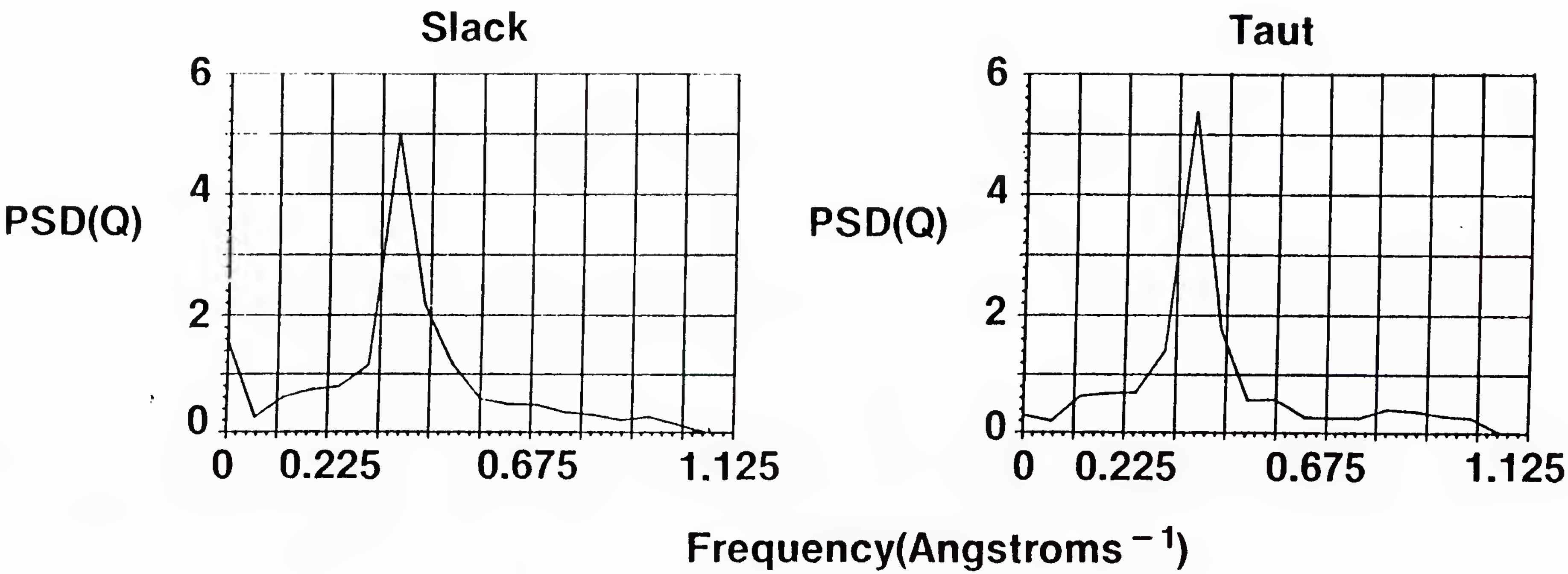

Figure A-2. Crosstalk Spectrum vs. Sensor Mounting. Sample A04SQC/0552.151/DSS1.152

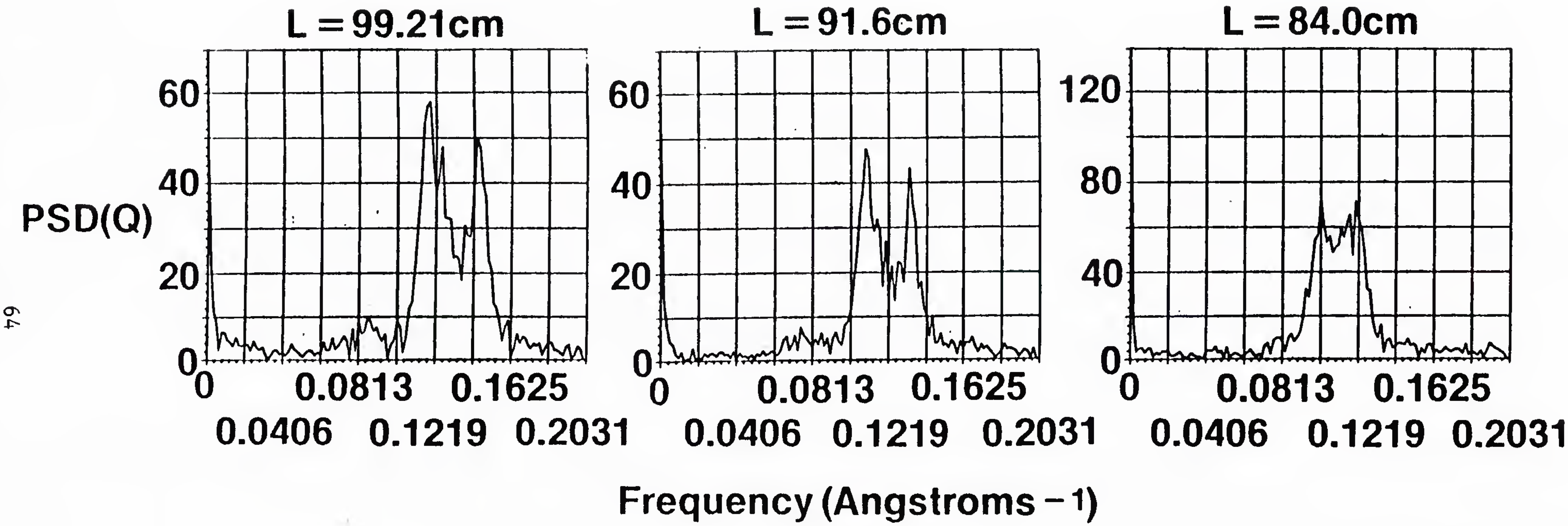

Figure A-3. Length Scaling in Crosstalk Spectrum. Sample AO4SQC/ DSS4.31/D8S4.51/DSS4.61

around the primary frequency. This type of signature variation could hinder proper interpretation during more complicated experiments, therefore we attempted to uncover the reasons behind the extra low frequency component and the appearance of complex features in the vicinity of the primary crosstalk carrier.

The scaling relations of Section II were used to guide the next test. The theory might lead one to interpret that the multiple peaks in the primary carrier of Figure A-3a are resulting from a sensor perturbation a few centimeters in from the sensor output termination. In an attempt to remove whatever type of inherent perturbation that might exist there (the termination units were well aligned), 7.6 cm were cut from the output end. Figure A-3b shows no substantial change in the general range of features in the spectrum after removal of the suspected piece of sensor. So an attempt was made to clip off 7.6 cm from the input end of the sensor in an attempt to eliminate the low frequency feature. It too would not disappear. The spectral changes from the earlier test case of Figure A-1 to the case of Figure A-3 appear to result from some inherent, nonideal characteristic associated with the sensor itself. The defect appears to be distributed over the entire fiber length and not isolated to the end regions.

Next, length scaling in the crosstalk spectrum was investigated. Section II predicts that the primary carrier signal, the dominant higher frequency feature of Figure A-1, should shift position in frequency space in direct proportion with sensor length. A test of this scaling is presented in Figure A-3. Several issues become apparent. Even though the quiescent, unperturbed crosstalk spectrum for this sensor was not identical to that of Figure A-1, the average location of the carrier peak does respond properly with length reduction. Hence, a scaling relationship appears verified, but a variability in the shape of the sensor signature has arisen.

3. RIGHT-ANGLE BEND

The effect of bends on propagation in a fiber can be quite complex. Three phenomona result for single core fibers: (1) resonant microbend conversion of energy from one mode to another, (2) nonresonant macrobend induced radiation losses for constant radii of curvature and (3) extra radiation effects associated with transitions between regions of constant curvature. For twin-core fibers a combination of the above could coexist with a fourth aspect: (4) relative phase shift between modes due to perturbations in core indices of refraction. During our experiments, we would like to eliminate or minimize the first three aspects. This is accomplised by limiting the range of perturbations placed on the sensor. For instance, no significant bend disturbances with short spatial wavelengths will be applied, therefore no microbend loses will be induced. From Reference 1 we find that if all of our experimental disturbances are associated with radii of curvature greater than 2 cm, then radiation induced coupling will be minimized. Finally, Reference 2 indicates that transition effects are of most concern, but with care these are minimized by not crimping the sensor. In short,

we would like to limit the crosstalk inducing aspect of bends to only the interactions described by Section II, which are to be of dominant importance to full-scale monitoring problems.

Reference data (straight sensor) of Figure A-4 is compared with data from a twin-core sensor after bending 90 degrees around a form, Figure A-5. The bend did not appear to impose large signals, so the logarithm(ln) was computed to help increase the general visibility of potentially important signals. Superposition of the signal locations predicted for the geometry of the bend (Figure A-5) indicates the occurrence of information consistent with the theory. But the results are short of conclusive. Therefore additional measurements were conducted.

4. SERPENTINE BEND

Two circular forms were used to define a serpentine path for the twin-core sensor as shown in Figure A-6. Crosstalk spectra were measured as a function of increasing separation, Δ, and compared with the straight reference condition. Figure A-7 supplies logarithmic plots of the PSD. Each case shows a superposition of the spectral components predicted by the theory in its early form. Once again, signals in the perturbed state are consistent with the model, but they are not as strong and definite as expected.

5. SINGLE LOOP

The complexity of signals in Section A-2 and the weakness of others in Sections A-3 and A-4 led us to another experiment. This time, the measurements were conducted at a single wavelength while the radius of a single loop was changed. Such an experiment should verify sensor response to this kind of perturbation. Figure A-8 illustrates strong crosstalk changes when the radius of the loop changes. In addition, the period of the crosstalk cycle rate versus radius appears to be monotonically changing. These results lead us to believe that significant signals should result for fixed perturbations, but with variable wavelength excitation. Hence further experimental conditions required investigated. Prior to such an extension of the effort, exploratory work was conducted to facilitate improved signals.

6. DISCUSSION

Measurements reviewed in Sections A-2 through A-5 were investigated during the first phase of this program. Several problems were discovered. The sensor response was generally weak, yet very complex and difficult to interpret. Simple comparison with predicted spectral line locations is insufficient. A more comprehensive interpretation must be made available. In addition, sensor deficiencies should be investigated in support of more reliable, cleaner and stronger signatures.

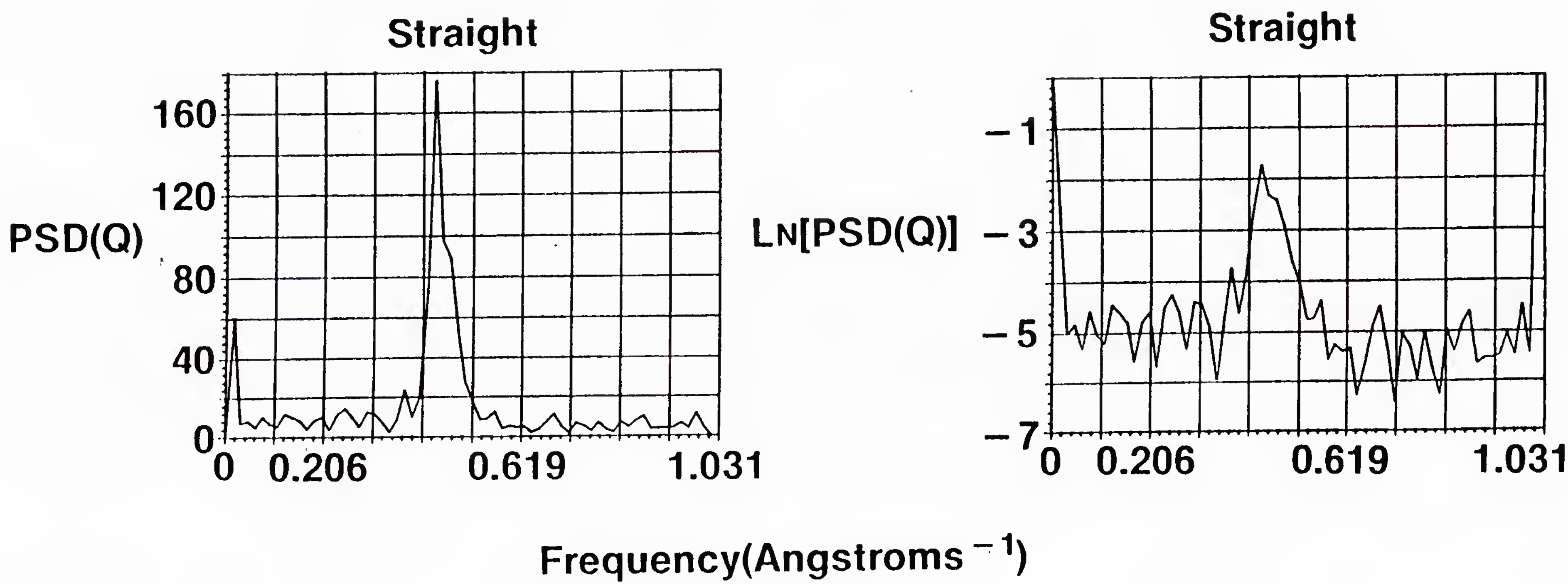

Figure A-4. Crosstalk Spectra: Right-angle Bend (straight reference case). Sample A04SQC/DSS2.101

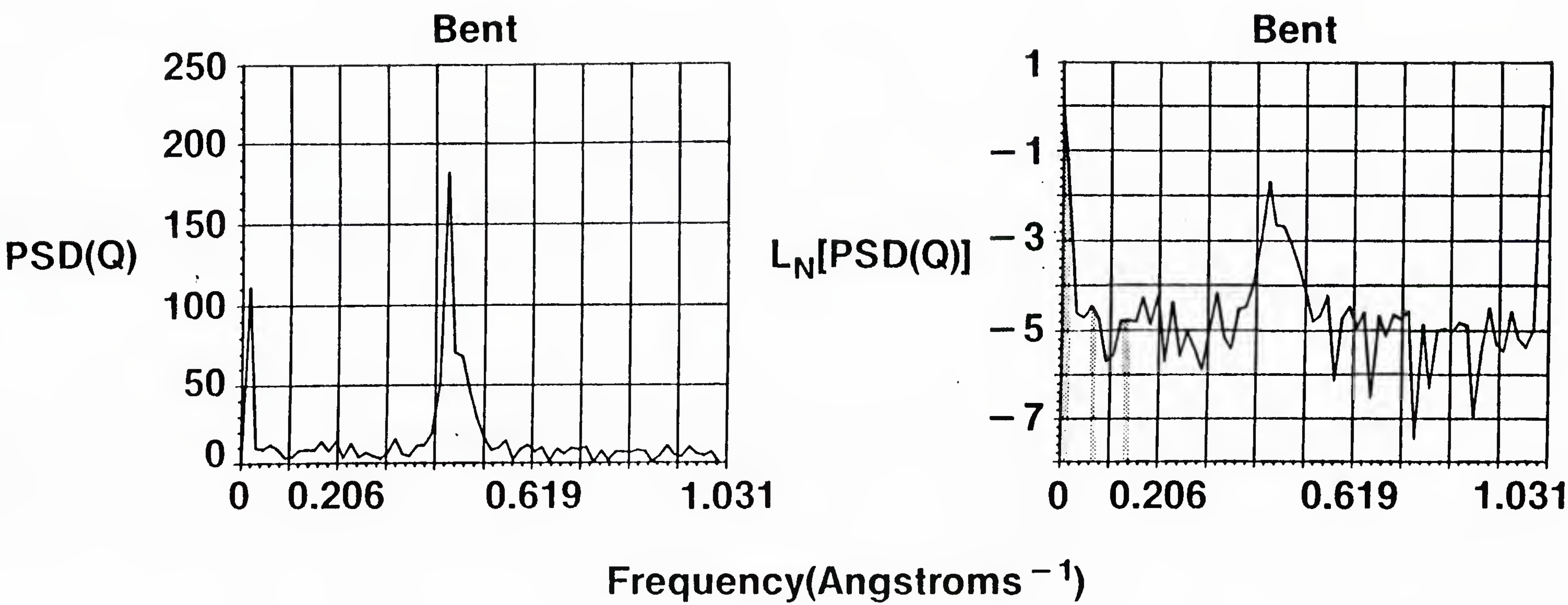

Figure A-5. Crosstalk Spectra: Right-angle Bend (perturbed case). Sample A04SQ/DSS2.81

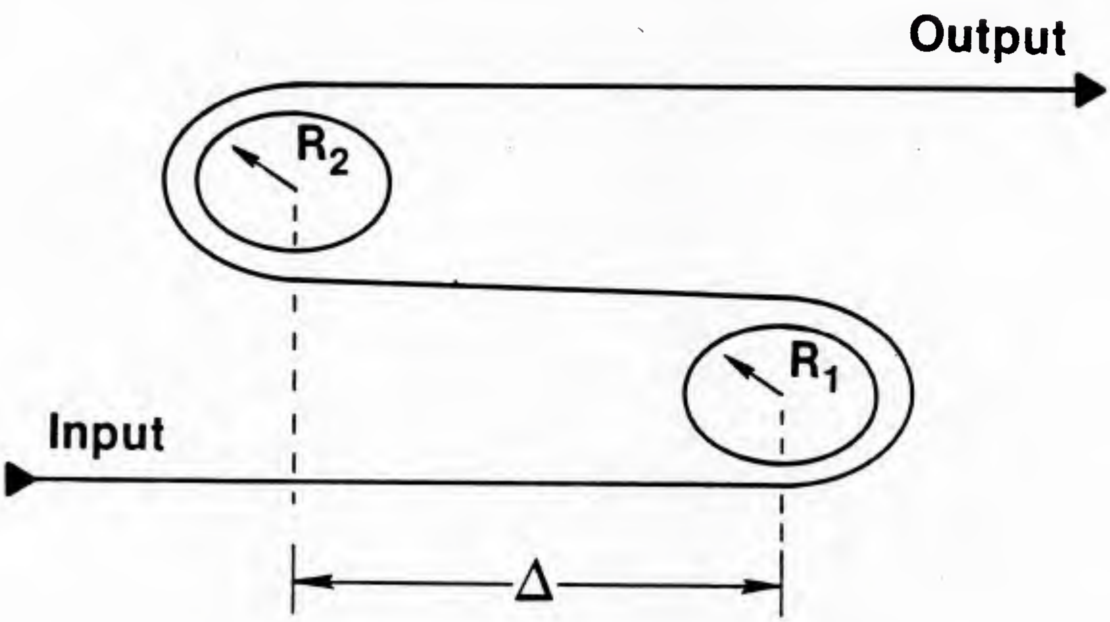

Figure A-6. Serpentine Demonstration

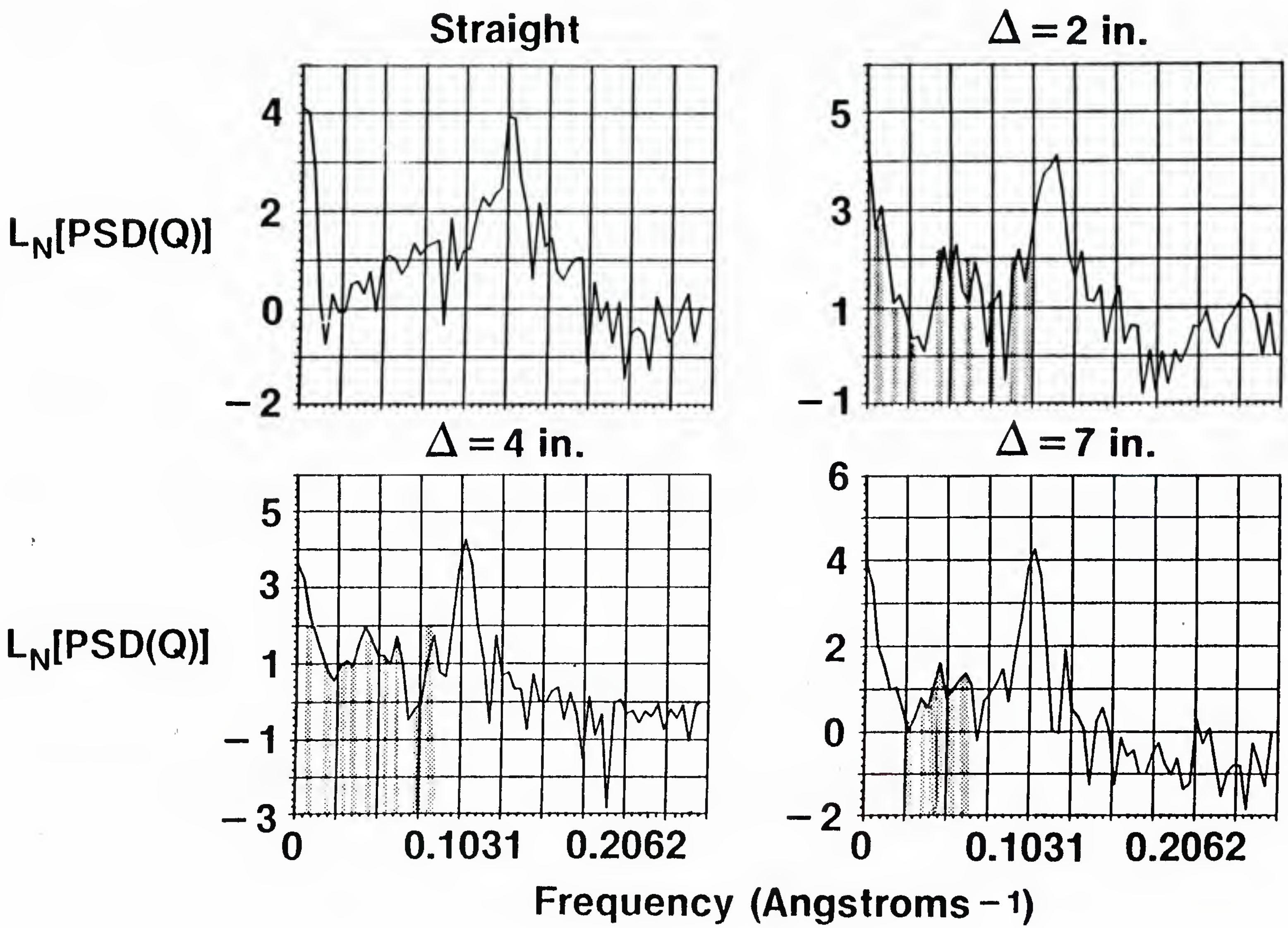

Figure A-7. Crosswalk Spectra: Serpentine Bend. Samples A04SQC/ DSS3.141/DSS3.15/DSS3.201

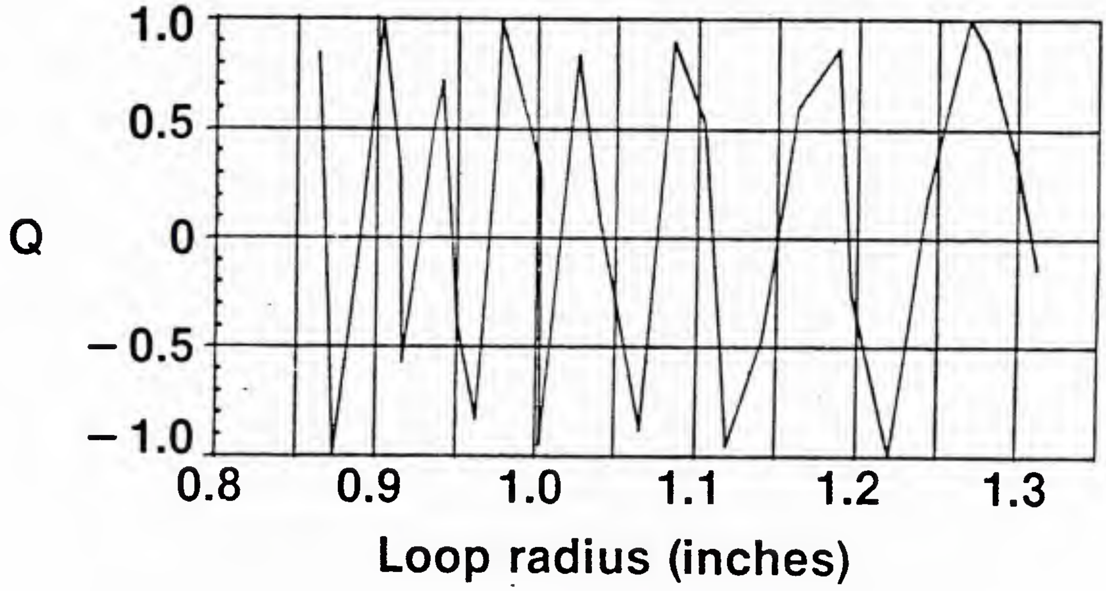

Figure A-8. Crosstalk vs. Loop Radius. Fixed Wavelength = 6328Å. Sample A04SQC/DSS7.00

Problems were discovered in many facets of this initial effort. There were some manufacturing defects which caused a variation in the sensor diameter as a function of length, as well as bubble inclusions. These issues induced deviation of the sensor signals from predicted response. Finally, changes in the sampling range and intervals along with special signal processing were expected to improve matters significantly. Investigation of these issues is presented in Appendix B.

APPENDIX B

IMPROVEMENTS

1. INTRODUCTION

The complexity and indecisive character of the preceding data compared with the simplicity of the theoretical predictions led us to re-evaluate our experimental apparatus, sensors and our modelling approach. This section describes improvements which were tested, in addition to discussing some deficiencies which were uncovered and rectified.

2. SENSOR QUALITY

The issue at hand is why does the theoretical description of a somewhat limited sensor, yet perfect within its assumptions, not match the response of the sensors used in the measurements. It is possible that the quality of the real sensor was insufficient for replication of the predicted signals. Since this investigation is concerned with a totally new concept, parameters concerned with intrinsic sensor quality must be interpreted from experimental difficulties or derived from theoretical descriptions. For instance, if the two sensor cores are not perfect mirror images of one another, then coupling diminishes rapidly. Such a geometric mismatch could lead to major discrepancies between the experimental and theoretical results. On the other hand, this problem is not of major importance in our case. The scanning electron micrographs of Figure B-1 show excellent core-to-core symmetry. However, another problem could develop. Practical crosstalk coupling coefficients could differ from the theoretical model if the outside diameter is not consistent from sensor beginning to end; even though at each point along the sensor, the cores are twinned. Such a problem would lead to individual sensor sections interacting with distributed bends while exhibiting a variable beatlength. The original theoretical model does not allow for such a sensor variation, assuming that only one geometrical operating condition of Figure B-2 is effective for the entire length. Review of sensor material utilized during the demonstrations of Sections A-2 and A-5 indicate a peak to peak size fluctuation of 22 percent--very significant, depending on the excitation wavelength. This level of variation could lead to major discrepancies between the measurements and the predictions. Under the improved form of the experiments, new sensors were procured, yielding signficantly improved dimensional control, only 7 percent peak-to-peak fluctuation. The quality of the sensor crosstalk response demonstrated a corresponding improvement (Figure B-3). Most significantly, the basic crosstalk signal-to-noise ratio appears improved by at least a factor of 50 and under special conditions as much as 200.

Any characteristic which might disturb the crosstalk function in magnitude, phase or frequency was considered suspect. The older sensor material showed

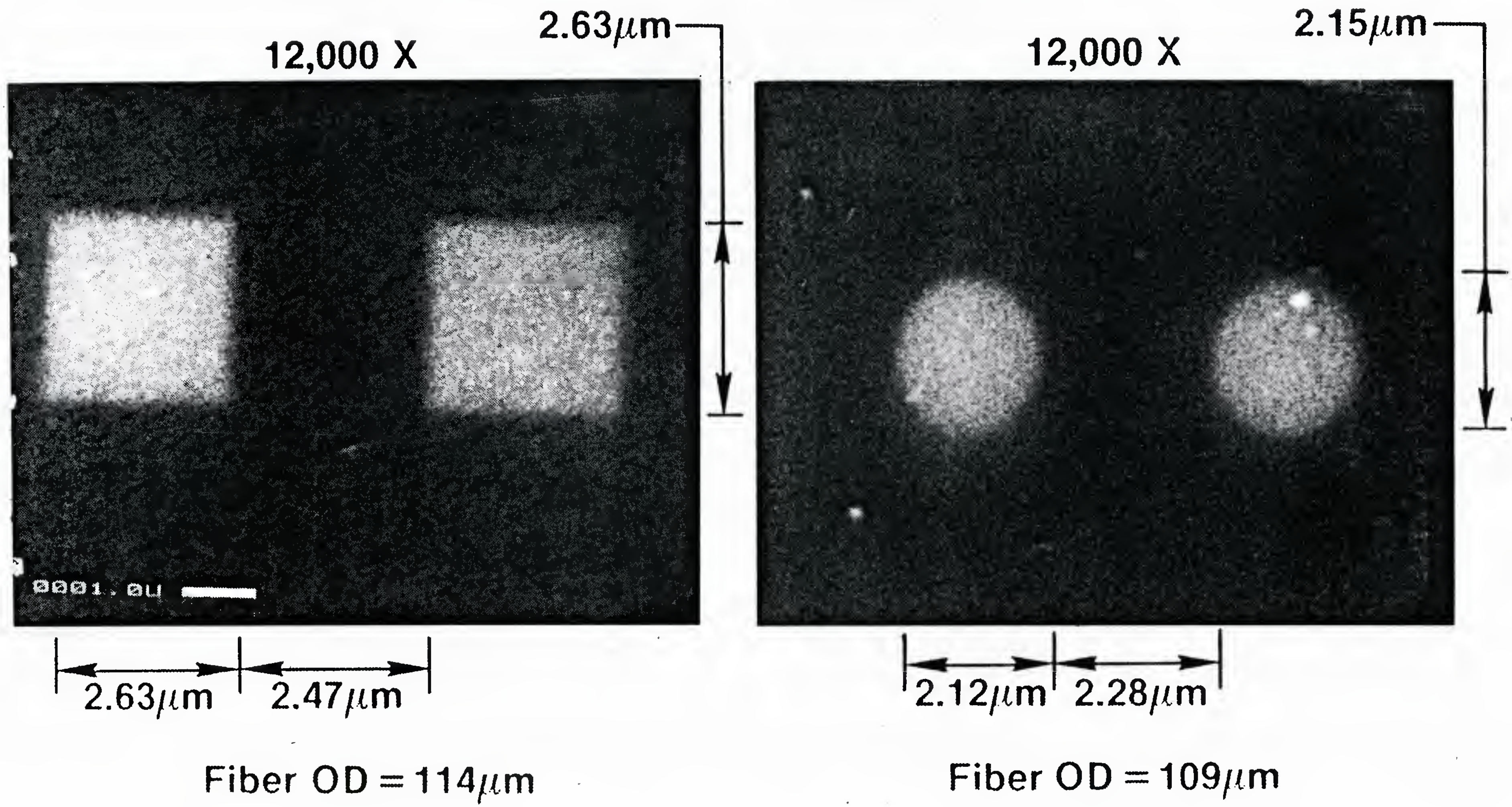

Figure B-1. Twin-Core Geometry

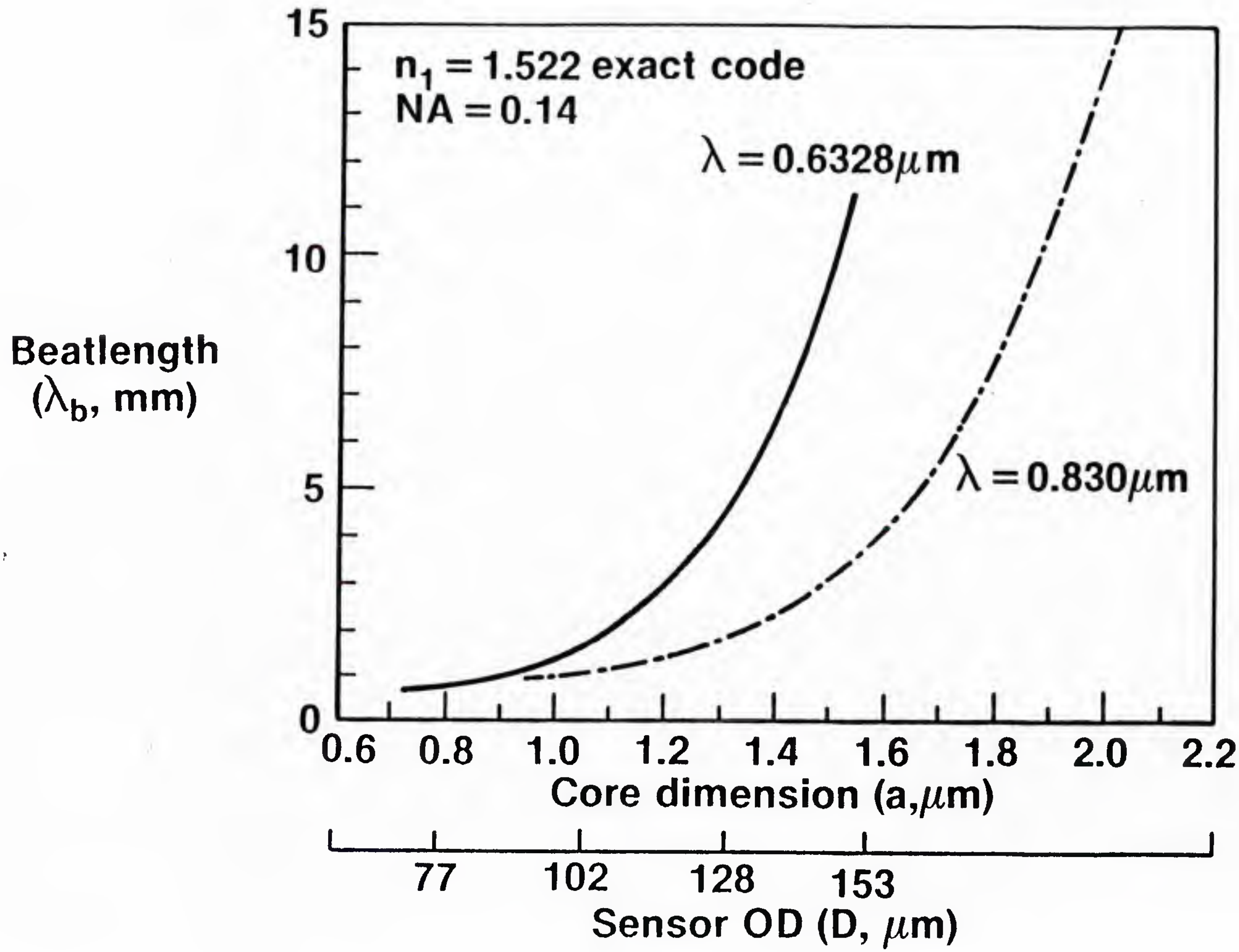

Figure B-2. Beat Length of Original Square Core

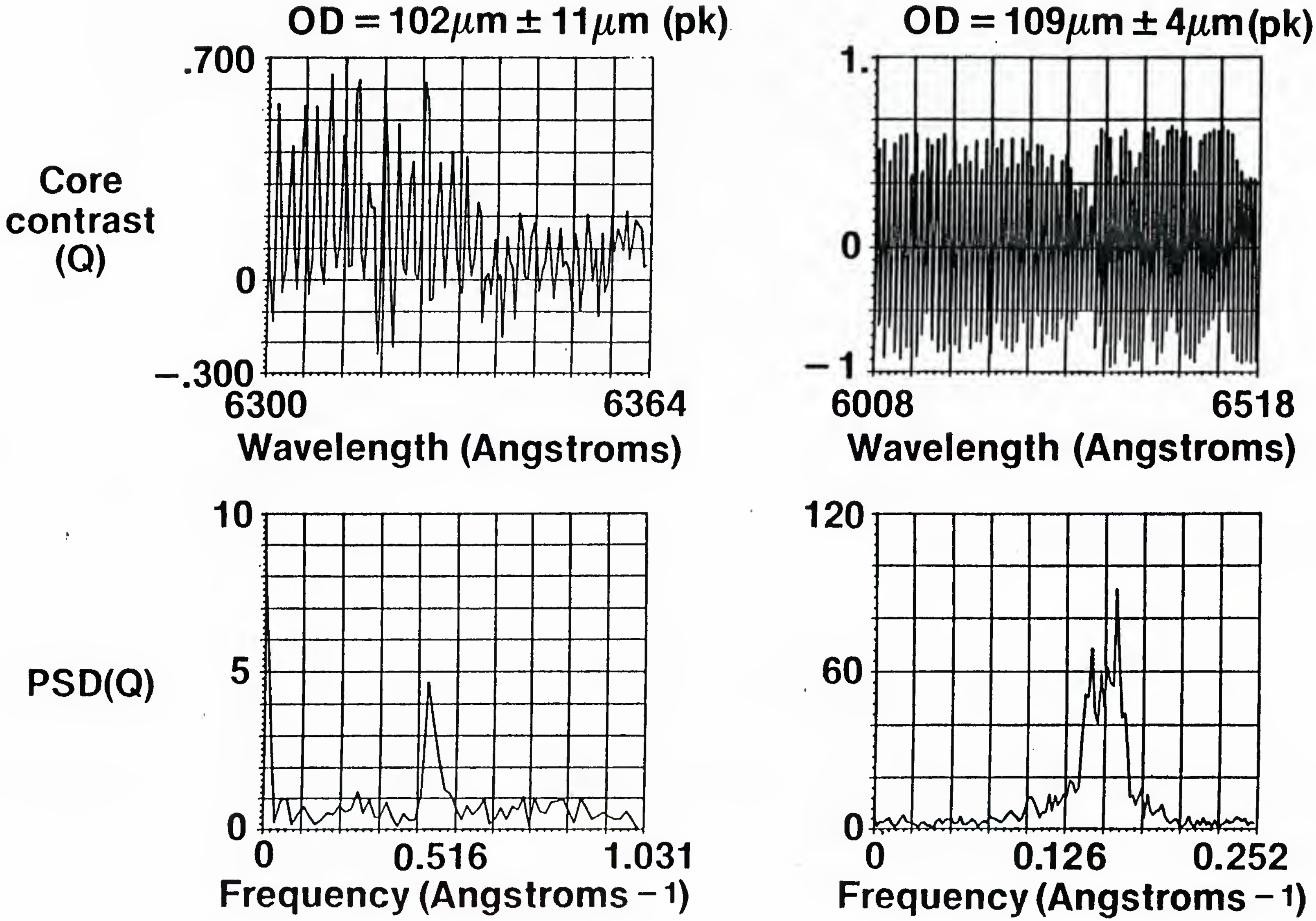

Figure B-3. Crosstalk vs. Dimensional Control

many strong scattering centers when illuminated by the dye laser. These inclusions could scatter light from the normally crosstalking cores, causing two possible side effects: a wavelength dependent reduction in core contrast and an initiation of extraneous crosstalking uncorrelated with the primary bend function. In either case the sensor output could be significantly disturbed from predictions. This type of internal defect existed in some of the new sensors procured for the extended program, but pretest inspection enabled selection of material visually free of scattering problems. Signal improvements such as those demonstrated in Figure B-4 resulted from the inspection/control effort.

Finally, the model was based on a specific core orientation relative to the plane of the bending perturbations. A twist of a few degrees per cm in the core orientation was discovered in the original material. For long devices utilized for these experiments this defect is significant. The issue was corrected in the new sensors by taking more care in preform fabrication and fiber drawing methods.

3. APPARATUS MODIFICATION

The previous section dealt with sensor associated problems. However, we observed the need for improvements in the experimental apparatus (Figure B-4). More specifically, the sensor end fixturing was of most concern. The original termination approach provided a short section of capillary tubing in which the sensor ends were secured. These tubing sections were then placed in differential positioners. Each piece of termination tubing was from 2 to 4 inches long. If the axis of the input and output mounting tubes were not properly aligned, then a kink would develop near the ends of the sensor route. Measurements indicated that this degraded the data. The problem was cured for the extended program by fabricating special tubing fixtures which held the sensor by the very first and last 1/8th inch of material, mitigating interfering responses.

4. SINGLE MODE EXCITATION

Section II predicts that the sensor output signals will become simplified and will increase in strength when operation is initiated through excitation of the symmetric mode, exclusively. We attempted to utilize this advantage during the improved experiments. There are two obvious methods to achieve this launch condition: (a) excite with illumination which initiates only the symmetric mode, or (b) taper the fiber input to fabricate a filter against the asymmetric mode while utilizing the normal illumination. Both have been tried. To begin with we attempted to start propagation with strictly the symmetric mode without size modification to the sensor. Expanded beams were used to provide good approximations to the required equal-amplitude/equal-phase illumination. Some rejection of the asymmetric mode was noted, but crosstalk in the quiescent sensor was still dominant. Since this approach did not adquately discriminate against the asymmetric mode, we tested the mode filtering ability of a tapered input section on the sensor.

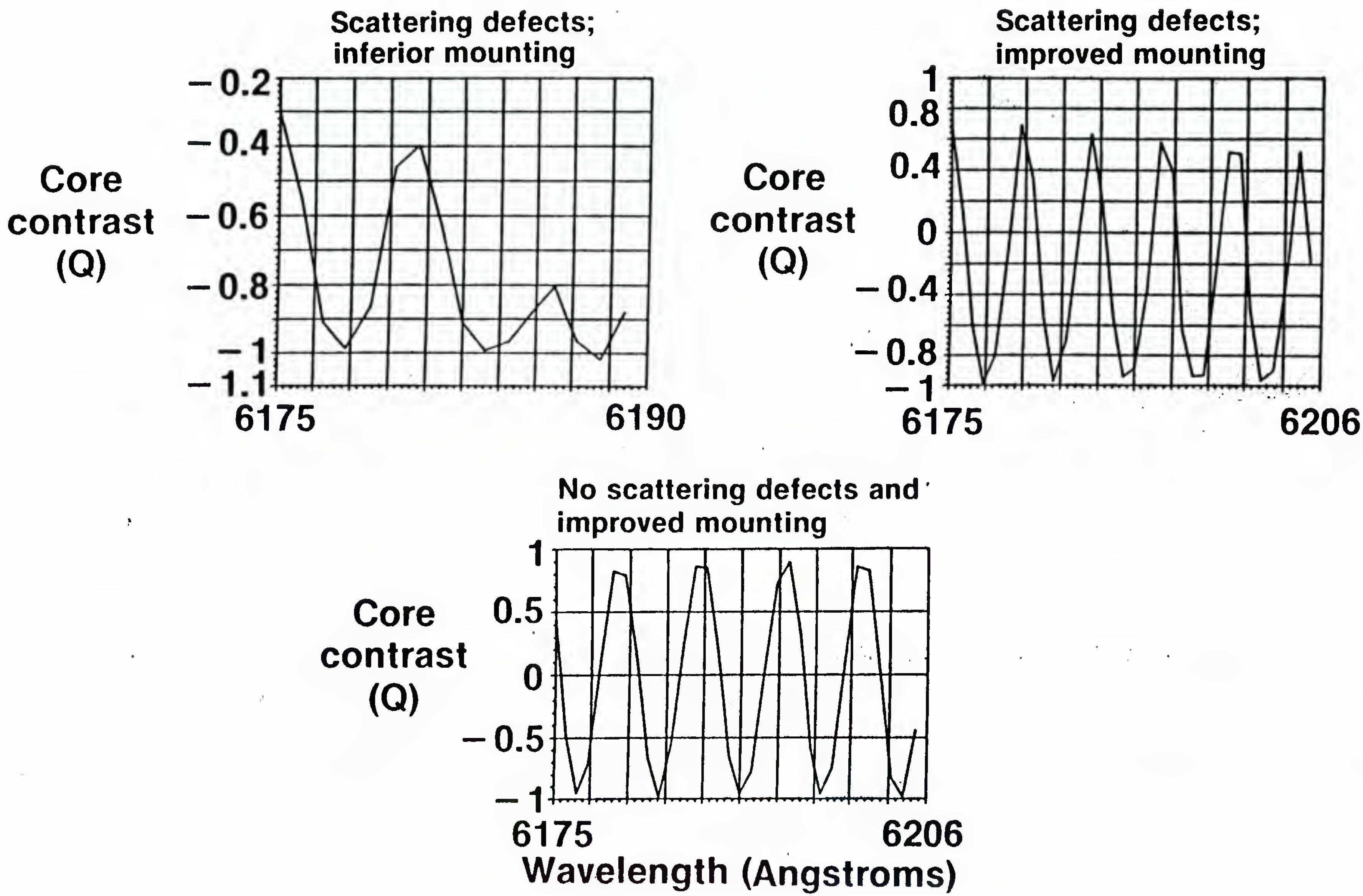

Figure B-4. Crosstalk Improvement Comparison

Initially, it was necessary to document the approximate size and operating wavelength at which the filtering condition becomes active. The effect is clearly shown in Figure B-5 for a sensor of uniform diameter: at a sufficiently long wavelength, the asymmetric mode is discriminated against, and crosstalk cannot exist. A more comprehensive picture of the onset of the filtering action is provided by Figure B-6 which plots the relative magnitude of the crosstalk function versus excitation wavelength. To test full implementation of this concept, the input end of a twin-core sensor was tapered to a size smaller than the remaining fiber. For wavelengths longer than the cutoff value, this reduced sensor section should not allow propagation of the asymmetric mode. Therefore, only the pure symmetric mode should enter the active section of the sensor. The test consisted of measuring core contrast at the device output as a function of wavelength. If the asymmetric mode was effectively suppressed by the input filter section, then crosstalk would cease beyond some critical wavelength. This type of response could not be detected. To check the performance of the filter section, the sensor was reversed; the taper at the output. With this orientation, filtering action was observed as shown in Figure B-7. Therefore, the filtering concept appears valid but the implementation requires more investigation. We believe that the taper must be slower, in fact, sufficiently slow to be classified as adiabatic. This condition can exist only for tapers which are many beatlengths long. The example of Figure B-7 appears to suggest a taper longer than 5-10 beatlengths is required. When this is achieved, the new excitation method may work and yield improved signals.

5. MEASUREMENT PARAMETERS AND SIGNAL PROCESSING

The wavelength range and sampling interval used during data acquisition are important for this research because of the characteristics of the sensor reliance on a Fourier transform interpretation of the signals. The total wavelength range for sensor operation exists from the asymmetric mode cutoff wavelength (V=1.2) to the wavelength at which the cores allow higher-order mode propagation (V=2.4). On the other hand, the number of samples is ultimately determined by the bandwidth of the dye laser (0.01 nm), defining the number of unique samples which can be made within the total range. From a practical point of view, however, computer storage and data processing time set the limits during these experiments. The laboratory computer could not efficiently handle data arrays larger than 256, therefore all measurements consisted of sample sets smaller than this. While experimenting with the actual number of samples per measurement array, it was discovered that the twin-core sensors exhibited a dispersive effect, that is, the beatlength was not a linear function of the operating wavelength. This fact affects the appearance of the data and imposes a coordinate transformation on the Fourier analyzed data, somewhat complicating the signatures interpretation. The dispersion is illustrated by making measurements with a fixed interval but with increasing range (Figure B-8). The dispersion problem is addressed later in Section A-5.

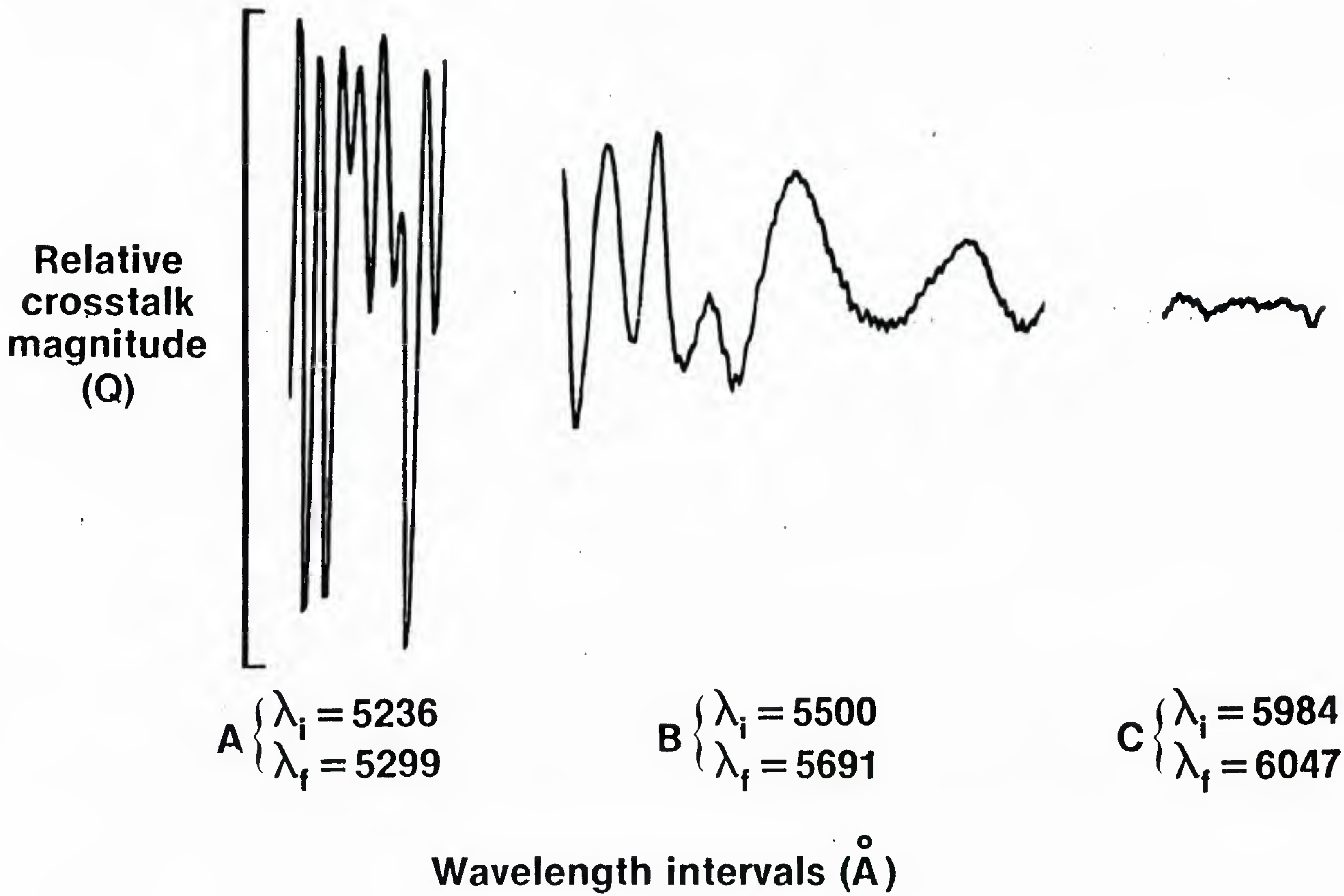

Figure B-5. Crosstalk Near Asymmetric Mode Cut Off

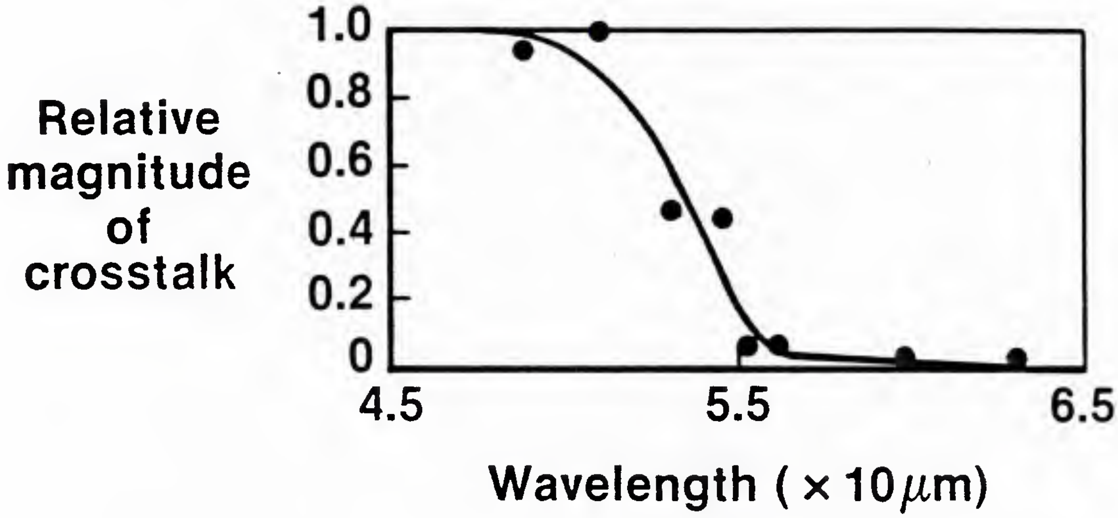

Figure B-6. Asymmetric Mode Filter. L = 30.8 inches; O.D. = 61 μm.
Sample A02.4SQC/8.29

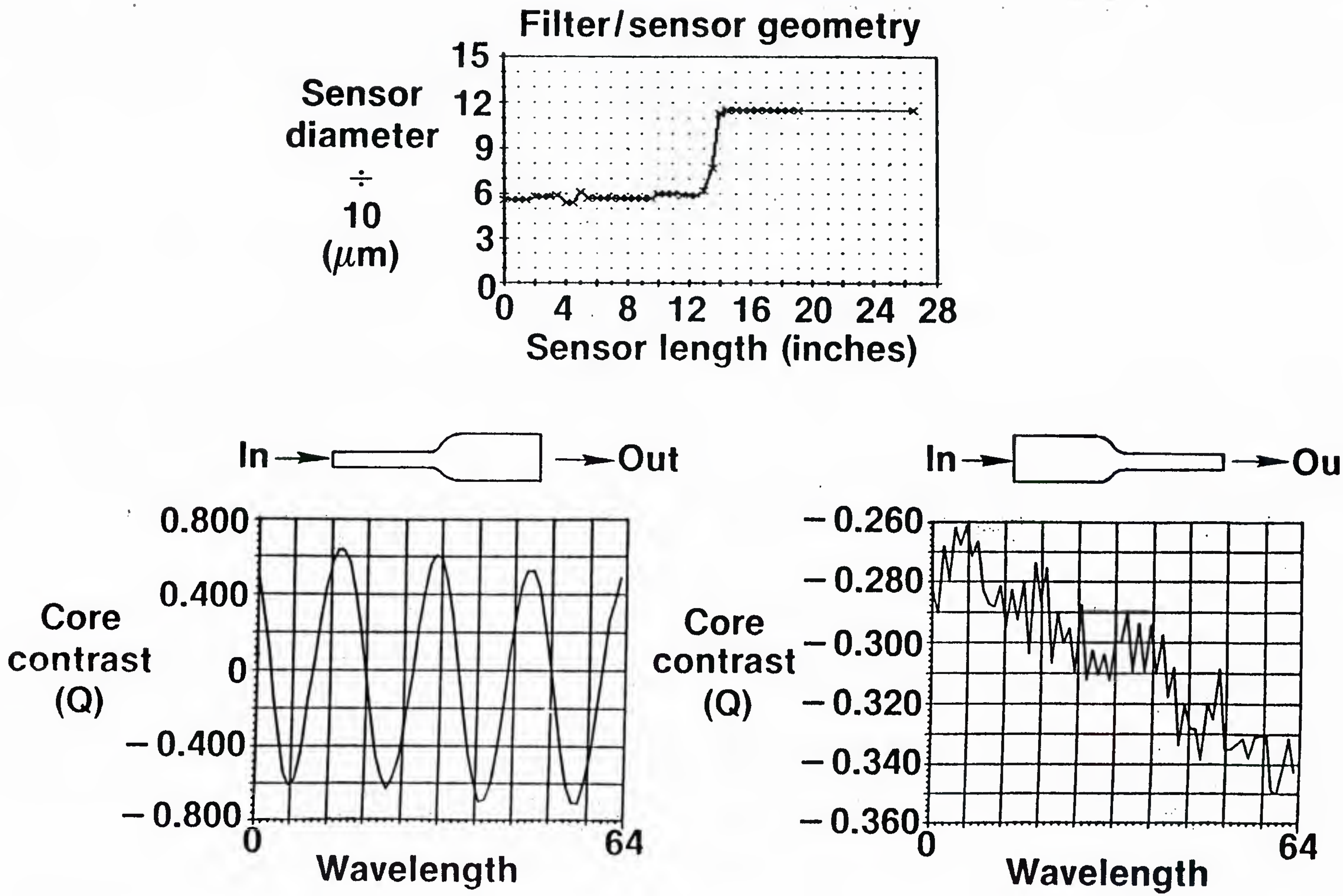

Figure B-7. Asymmetric Mode Filter

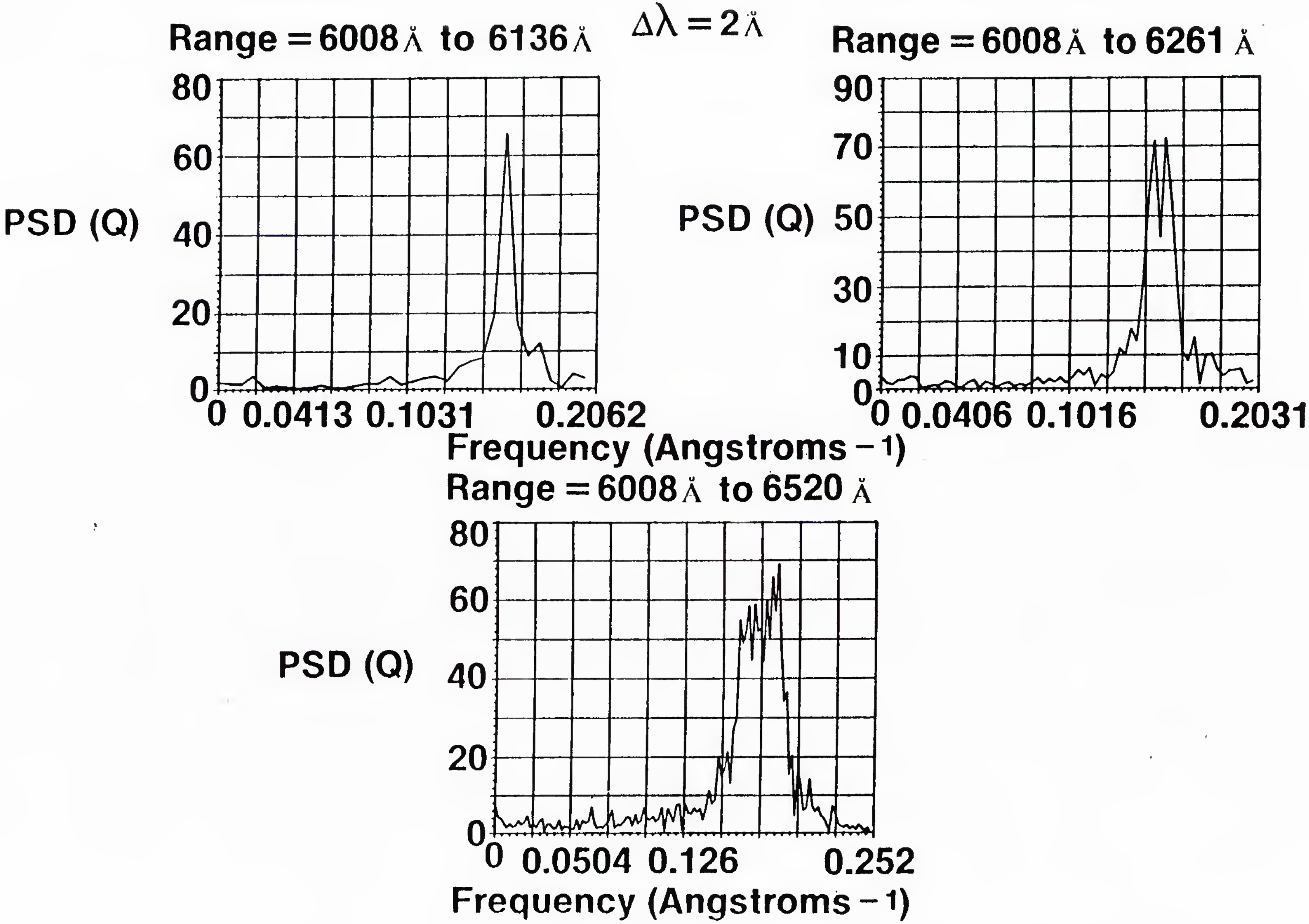

Figure B-8. Parameter Assessment: Straight fiber. Sample A045SQ/DSS7.191

After improving the data collection parameters (range and sampling period) and acquiring new information, there are numerous methods which can be applied for interpretative post-processing. In order to define a processing sequence, one must select a specific parameter in the signatures to be optimized and identify whether or not decision-making processes must be implemented. For example, one immediate improvement incorporated for each measurement was subtraction of the mean array value from measured crosstalk signals. This step reduces the appearance of somewhat useless DC offsets which can show up in baseband region of the spectra. The next problem pertains to clarifying the existence of important spectral signals. In the case at hand, low level bend-induced signals must be detected. These signals should appear in the crosstalk spectrum with various magnitudes and locations indicative of the perturbations placed on the sensor. In addition, the primary carrier component is expected to be significant in all of the demonstrations. If the weaker bend-induced signals result from geometries causing them to fall adjacent the sensor total-length signal, then interferences may exist. Sidelobes associated with the stronger signal may overlap or obscure bend-induced signals. Signal processing methods which might reduce some of this interaction could enhance our basic spectral interpretations.

Sidelobes exist as artifacts of the discrete sampling process utilized over the fixed bandwidth of the finite Fourier Transform. The parameters of sampling period and total sample array width are represented by the dye laser measurements at fixed wavelength intervals over the selected operating range. In the Phase-I data, the spectrum was calculated by taking the Fourier transform of the crosstalk array as sampled. In such a situation the spectrum consists of a signal array with many individual elements. Some features contained in this signal array are not related to the crosstalk data but are related to the parameters of the Fourier transform. Manipulation of the ancillary features may improve the clarity with which signals can be detected. For instance, Figure B-9 shows the ideal spectral form that a single, perfect crosstalk cosine function would exhibit when the finite Fourier transform is performed over a crosstalk array of unity magnitude. The original array was greatly padded. The term padding refers to the addition of many zero-magnitude array elements to the crosstalk data before it is transformed (see Figure B-10). This process provides optimized interpolation in transform plane, allowing the signal sidebands to be plotted with great detail. If the transform is performed strictly over the data array without padding, then the spectrum will yield only an outline of Figure B-9 by approximately connecting the peaks of the sidelobes and dissolving the detailed features. In either case, it is obvious that a second signal feature falling adjacent the original would cause a complicated interaction which might leave both indistinguishable. To combat this problem, a method can be utilized to reduce the strength of the sidelobes and therefore reduce their potential interfences. This can be accomplished by applying carefully tailored windows to the crosstalk data array prior to tranformation. The implementation of this windowing process is conceptualized in Figure B-11. Several candidate window functions

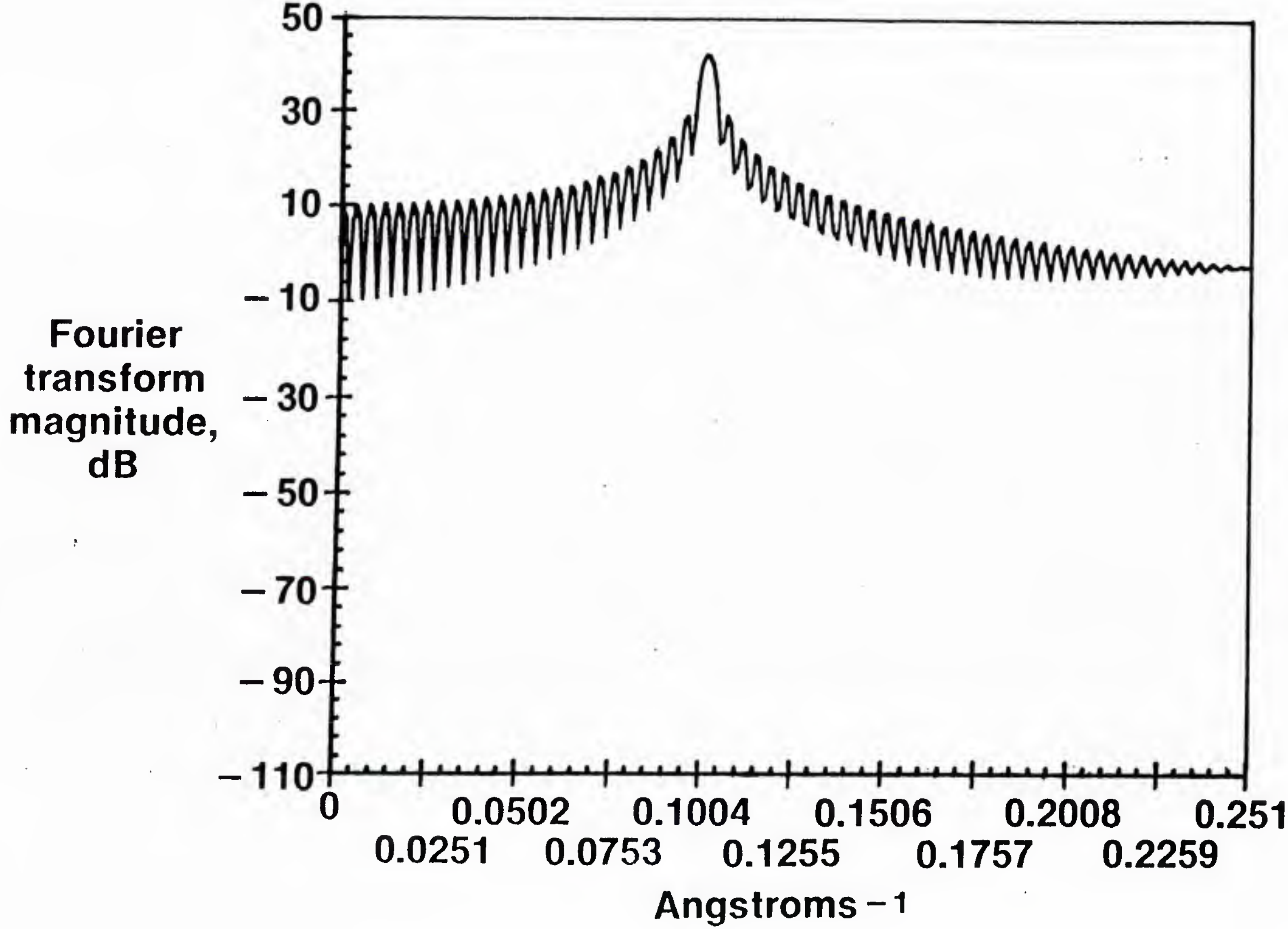

Figure B-9. Signal Processing: Rectangular Window Response

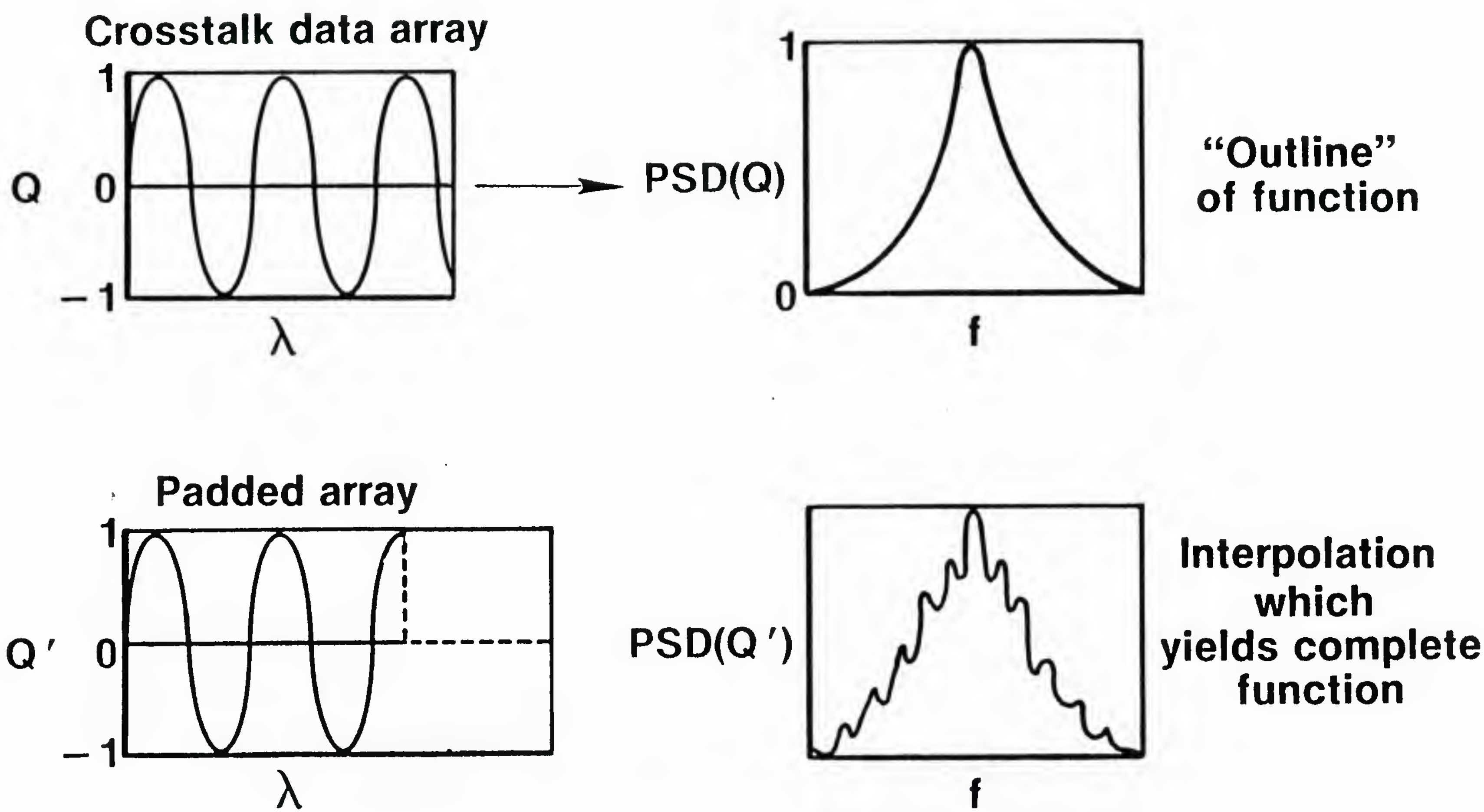

Figure B-10. Signal Processing: Concept of Padding Crosstalk Array

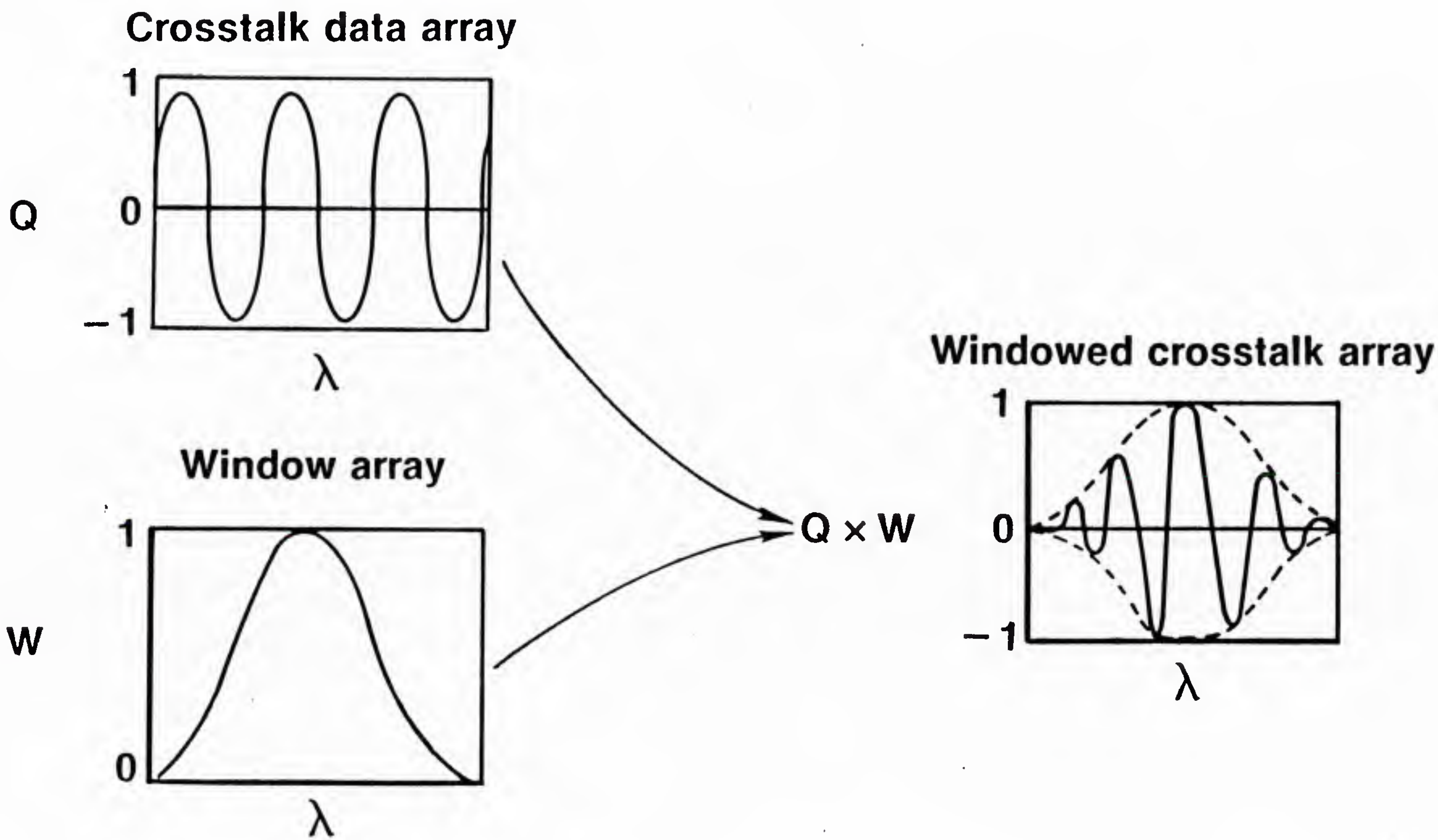

Figure B-11. Signal Processing: Concept of Windowed Crosstalk Array

are shown in Figure B-12 and their effects on a single frequency cosine signal plotted in Figures B-13 through B-16. The performance of these window functions is defined by their relative ability to reject sidelobe effects while not spreading the main signal lobe. If the window broadens the primary signal feature too much, then resolution becomes compromised. A performance comparison is provided by Table B-1 where the sidelobe rejection levels and resolution widths are summarized (interpreted directly from graphs rather than detailed calculations). We have selected use of the Kaiser-Bessel window as the best combination of good sidelobe rejection while maintaining high resolution. Application examples will be presented later in this section.

We tested other signal processing steps which were related to making a comparison or decision about the perturbed sensor relative to the straight reference case. Such processes will aide our evaluation of the distributed sensing technique and the complexity of its application. The steps appear in Figure B-17, which highlights normalization, ratioing and thresholding operations. To develop several test cases, we subjected some of the Phase-I data to the processing philosophy.

Excellent qualitative improvements were demonstrated through the implementation of the extra data manipulation. Linear signal presentation becomes less cluttered and easier to interpret. In fact, as seen in Figure B-18, it might be preferred over the logarithmic plots when signal levels are strong enough. But if weak and strong signals must be compared on the same graph (Figures B-19 and B-20), the logarithmic presentation helps greatly. The threshold process, as a yes/no detection indicator of spectral features, shows good potential even though more development is required. Thresholds other than unity must be developed, based on the statistical characteristics of the signals and the type of decision-making desired. Unfortunately, there are still unclear situations in which either signals are missing or unexpected signals have appeared. From a decision-making point of view, this type of error leads to some misses and false-alarms. Furthermore, the model does not provide the relative magnitude of signals--only location. Therefore, one cannot develop a complete predicted picture of the crosstalk spectrum. This deficiency has been rectified during the improvement phase of our work and is demonstrated with the Phase-II data.

After reviewing the raw and the processed signal comparisons, it appears that some other problem remains. Correlation between the model and the experiments requires improvement in order to provide more definitive results. One important issue which addresses this problem is discussed in the next section: calibration of the model to the laboratory sensors.

6. SENSOR CALIBRATION MEASUREMENTS

In preceding discussions, we demonstrated improved techniques for interpreting the experimental measurements. Discrepancies still exist. In an attempt

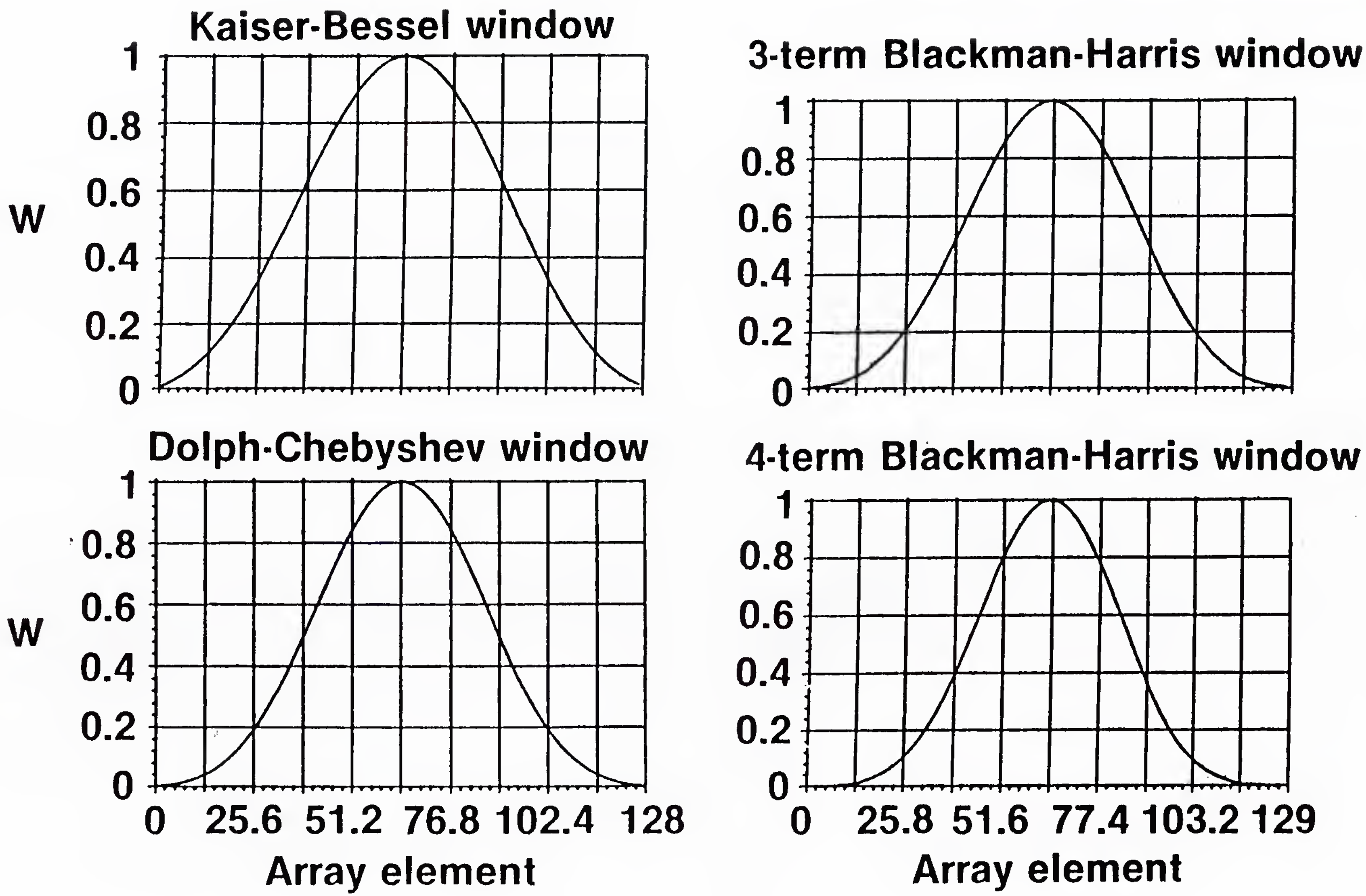

Figure B-12. Signal Processing: Candidate Window Functions

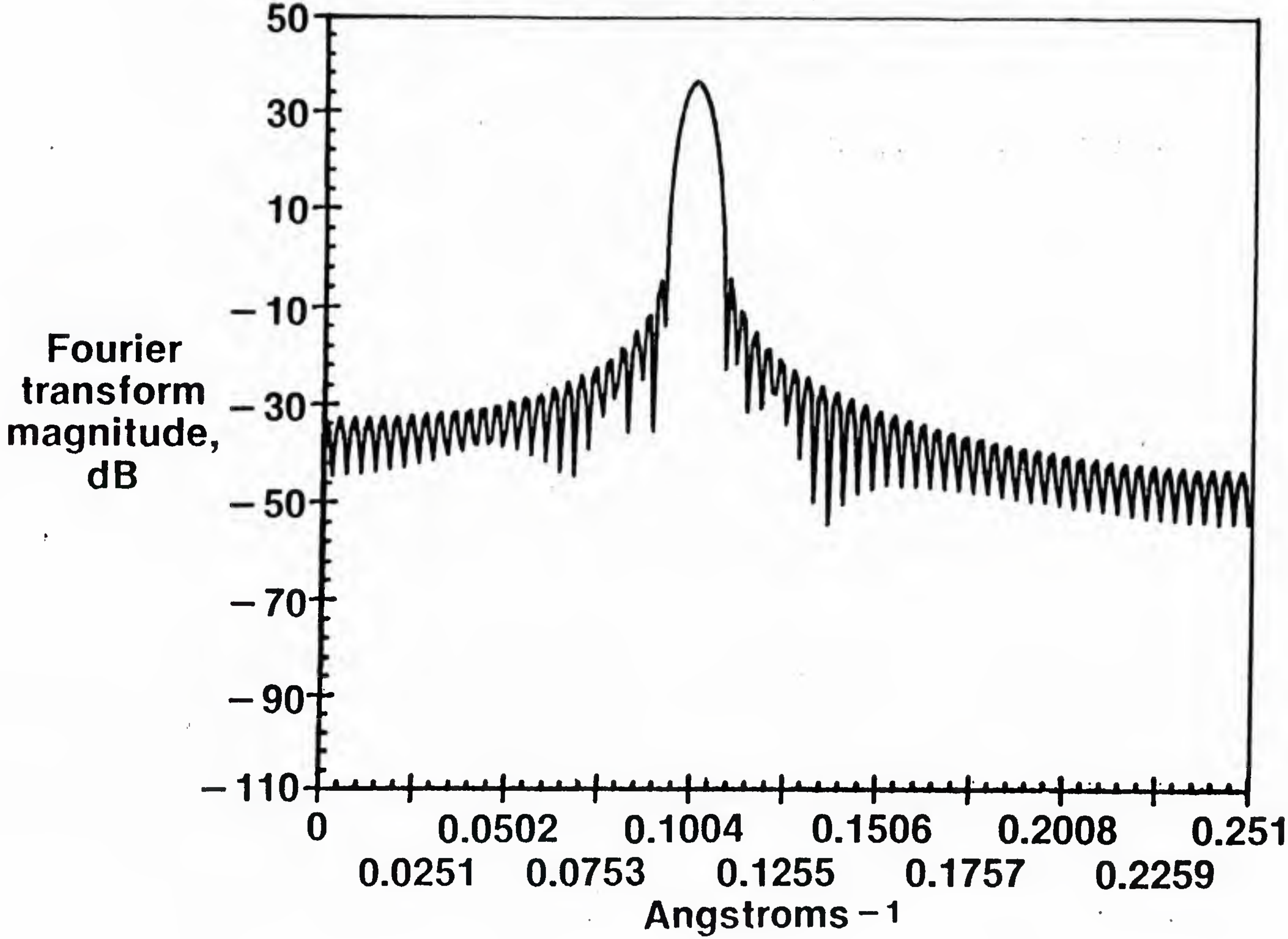

Figure B-13. Signal Processing: Kaiser-Bessel Window Response

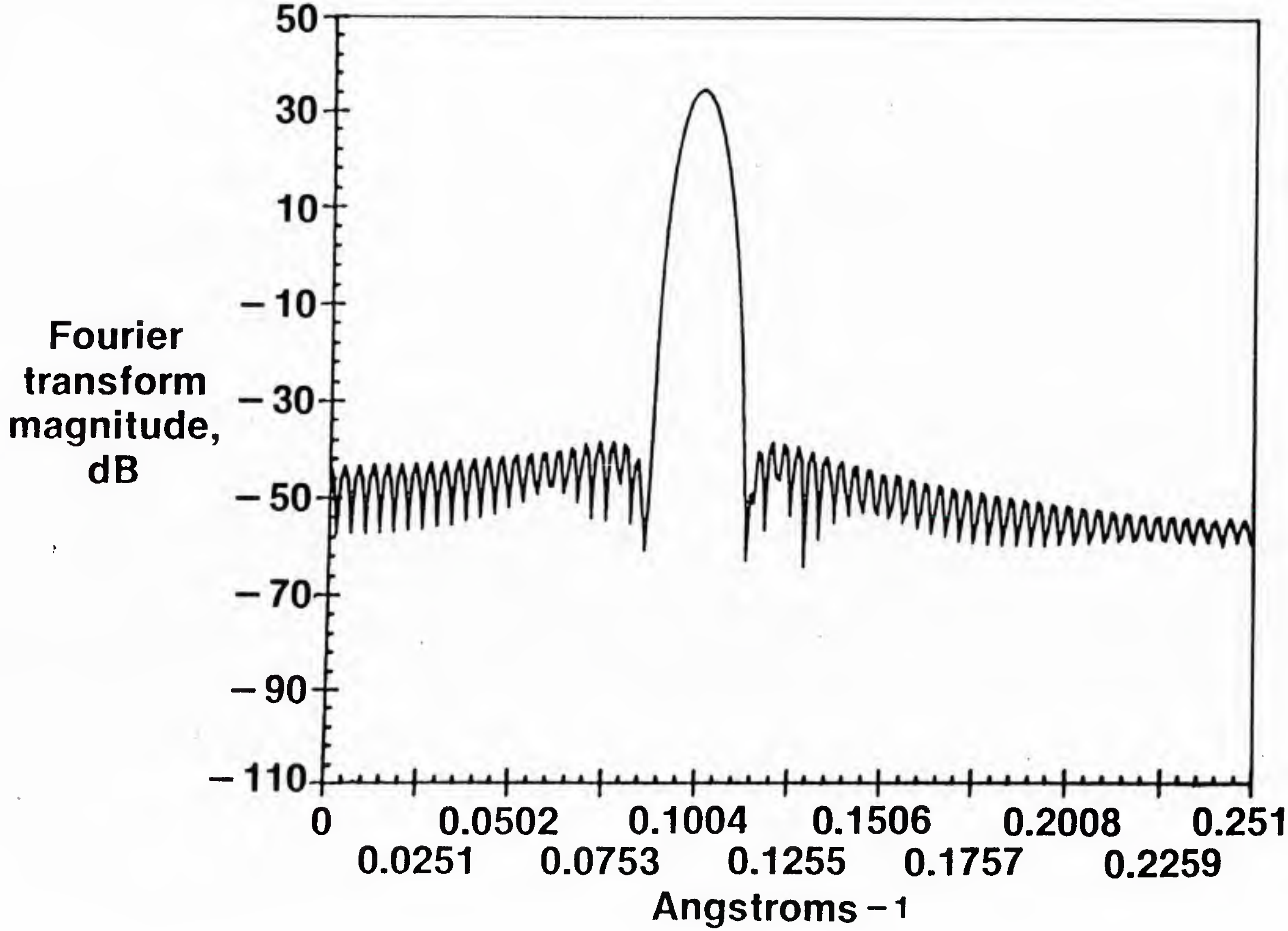

Figure B-14. Signal Processing: Dolph-Chebyshev Window Response

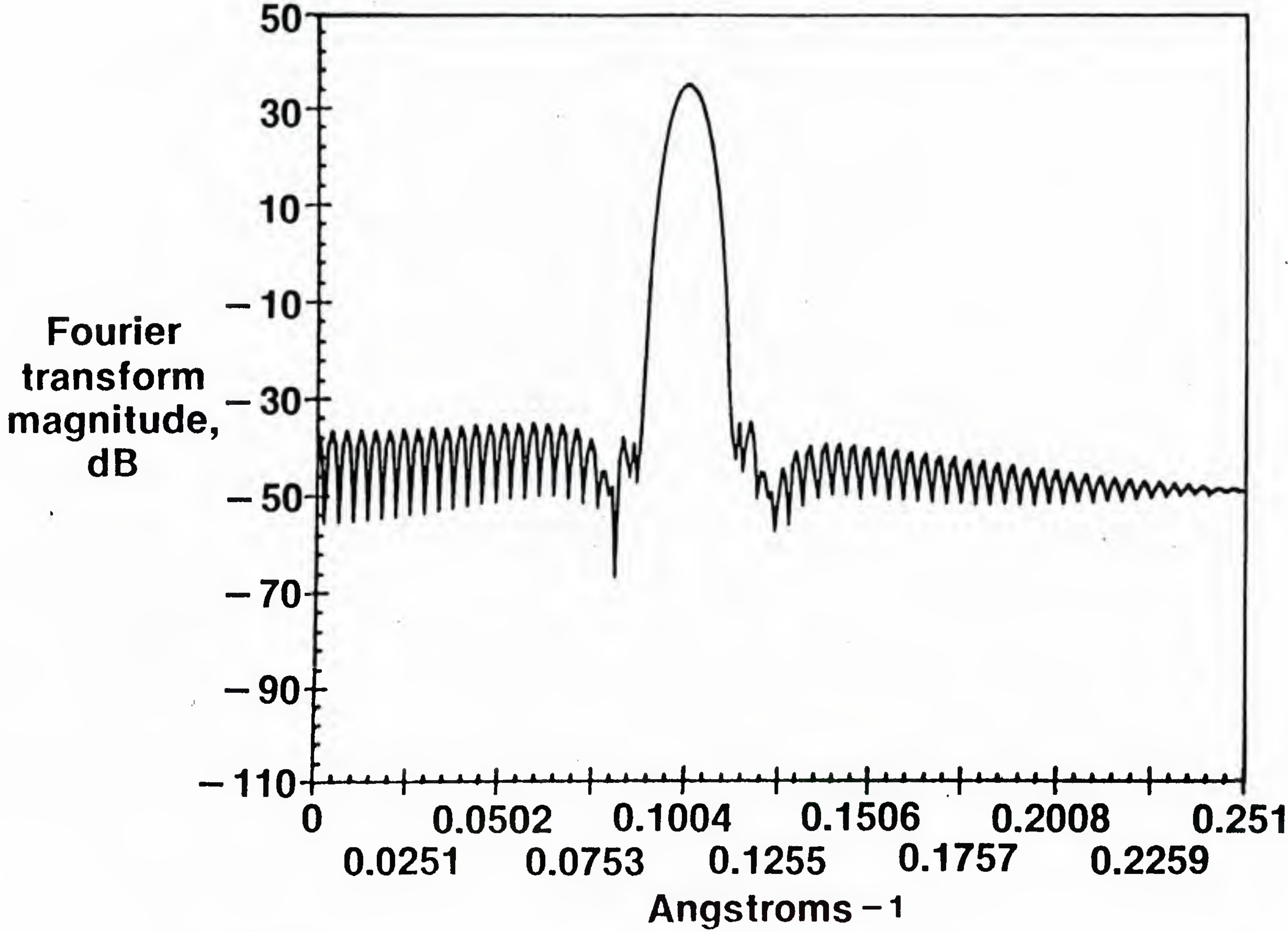

Figure B-15. Signal Processing: 3-Term Blackman-Harris Window Response

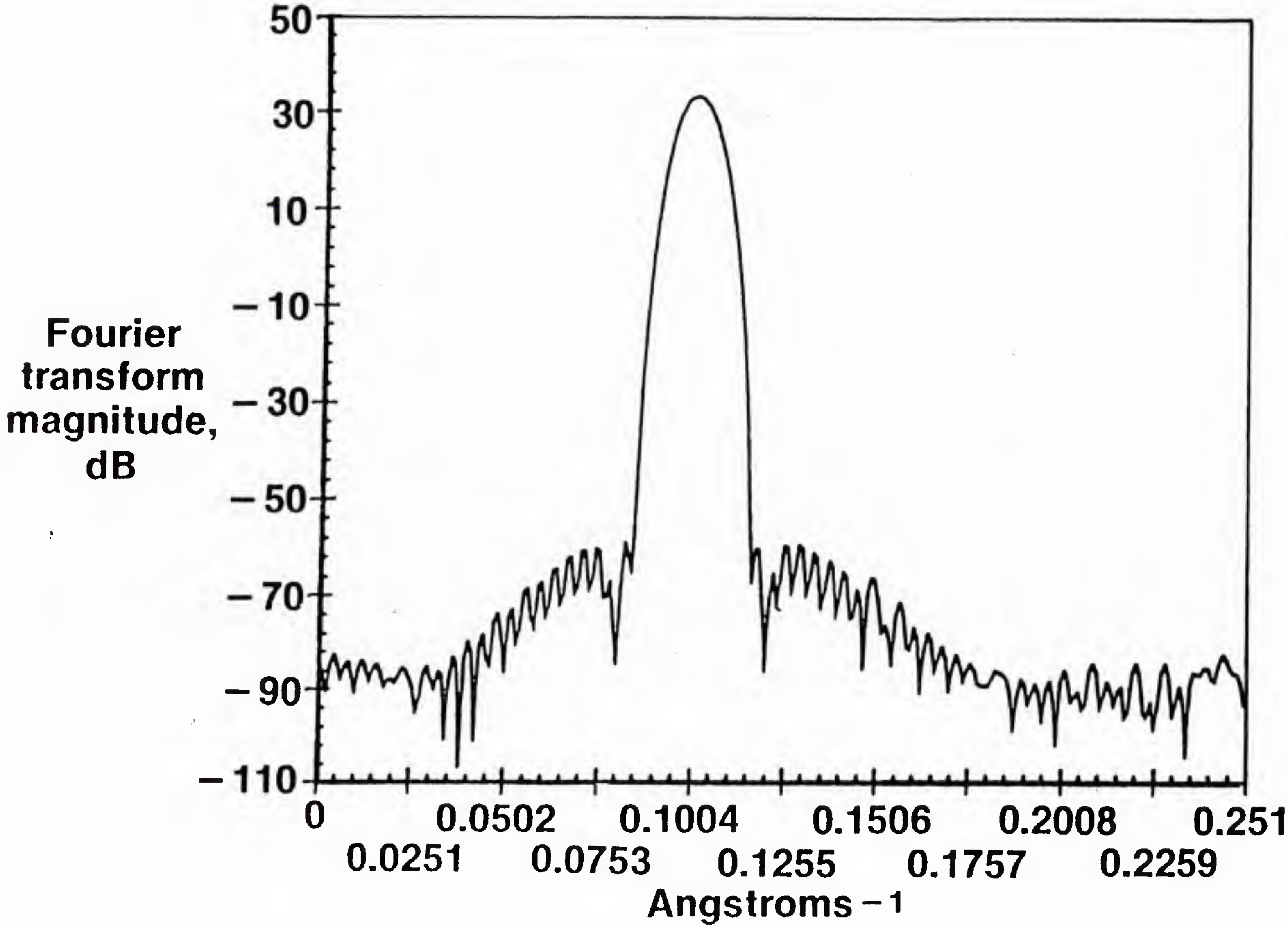

Figure B-16. Signal Processing: 4-Term Blackman-Harris Window Response

TABLE B-1. RELATIVE WINDOW PERFORMANCE

Sinewave Results

Window	Sidelobe Level (-dB)	6 dB Width
Blackman-Harris		$x10^{-3}$ Å
4 Term	93	
3 Term	70	9.2
Kaiser-Bessel		
$\alpha = 3.5$	63	7.0
Dolph - Chebyshev		
$\alpha = 4.0$	72	7.7
Rectangle	14	6.4

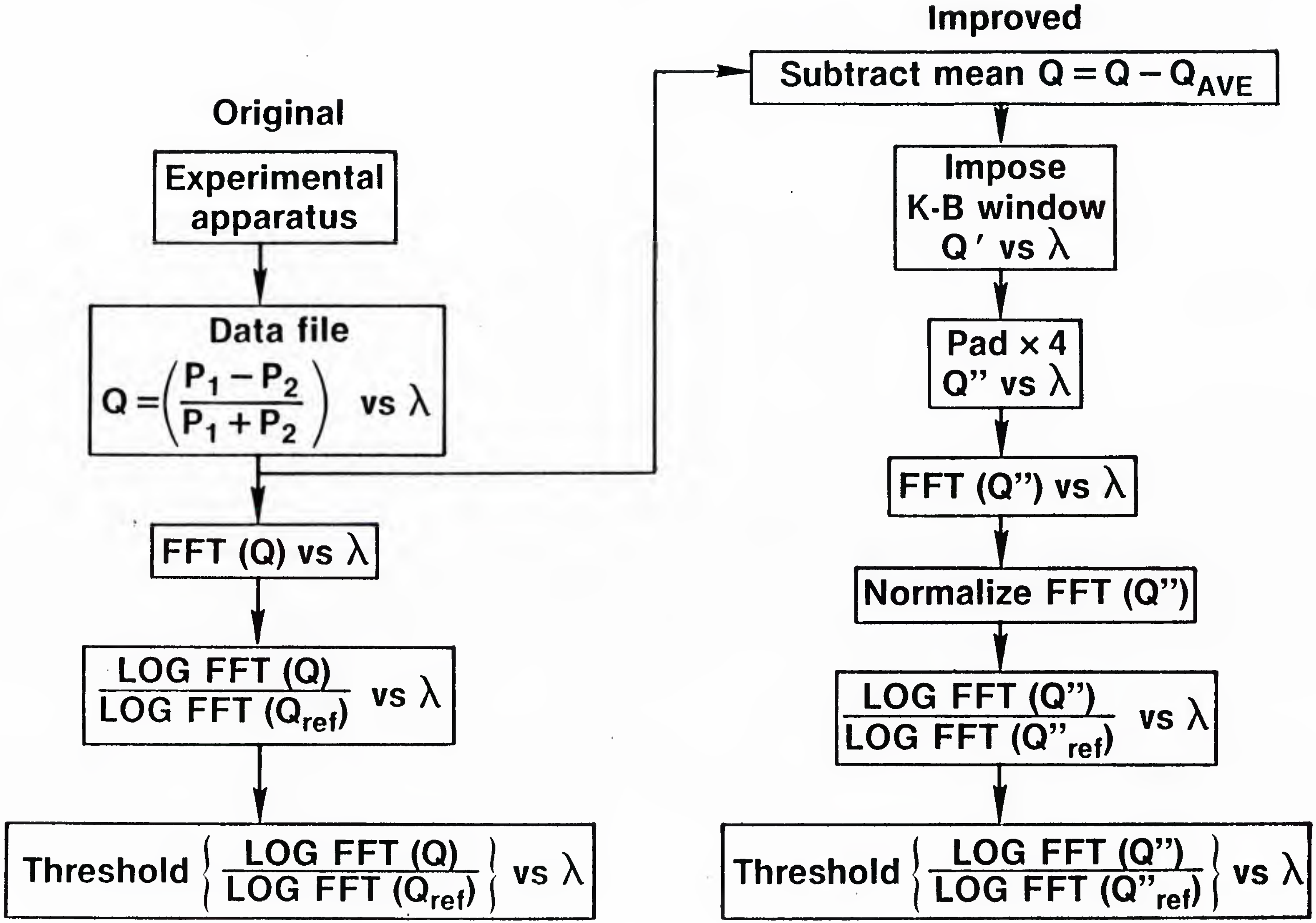

Figure B-17. Signal Processing Application

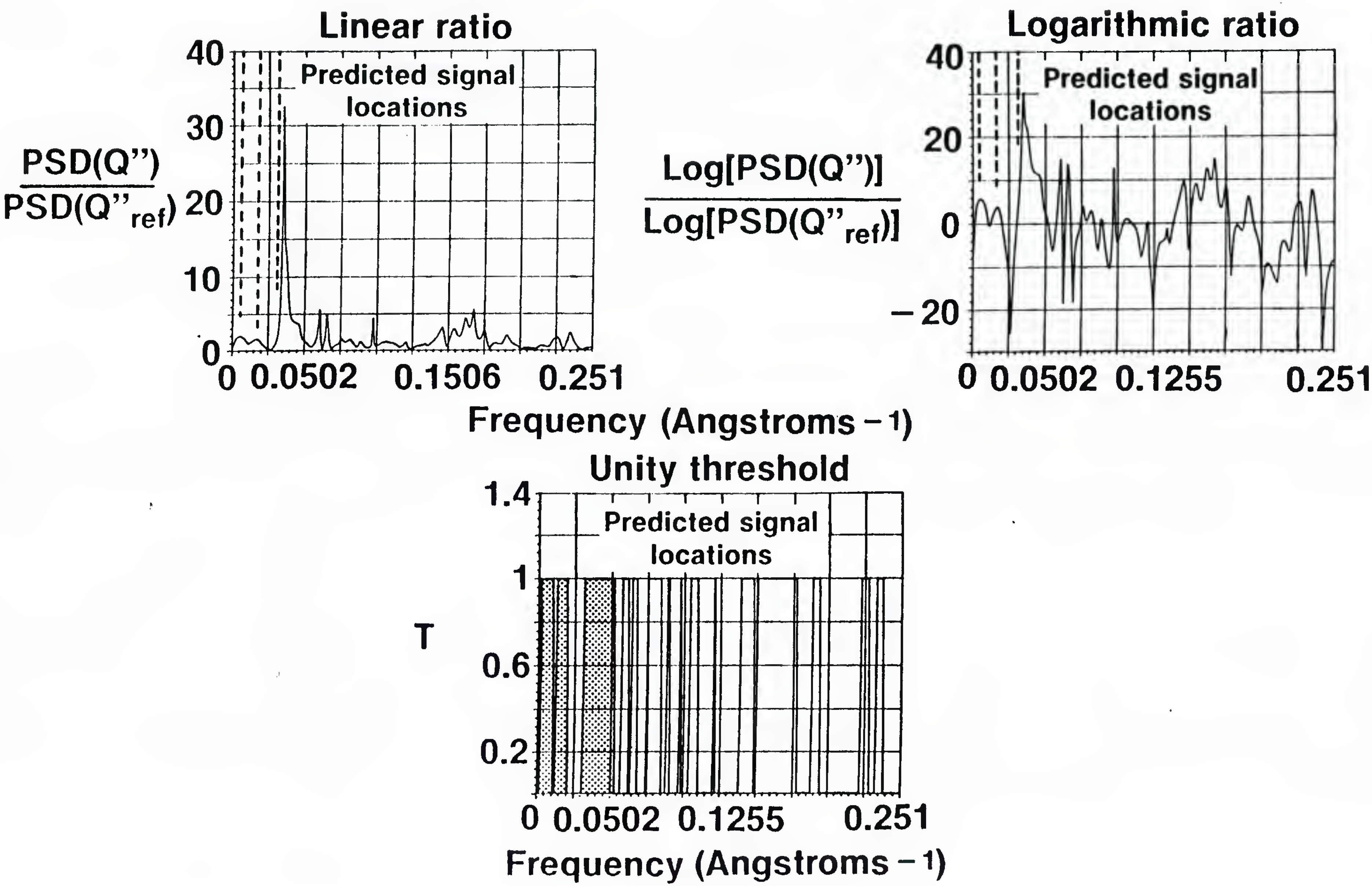

Figure B-18. Right-Angle Bend Data (Fig. A-5). Processed

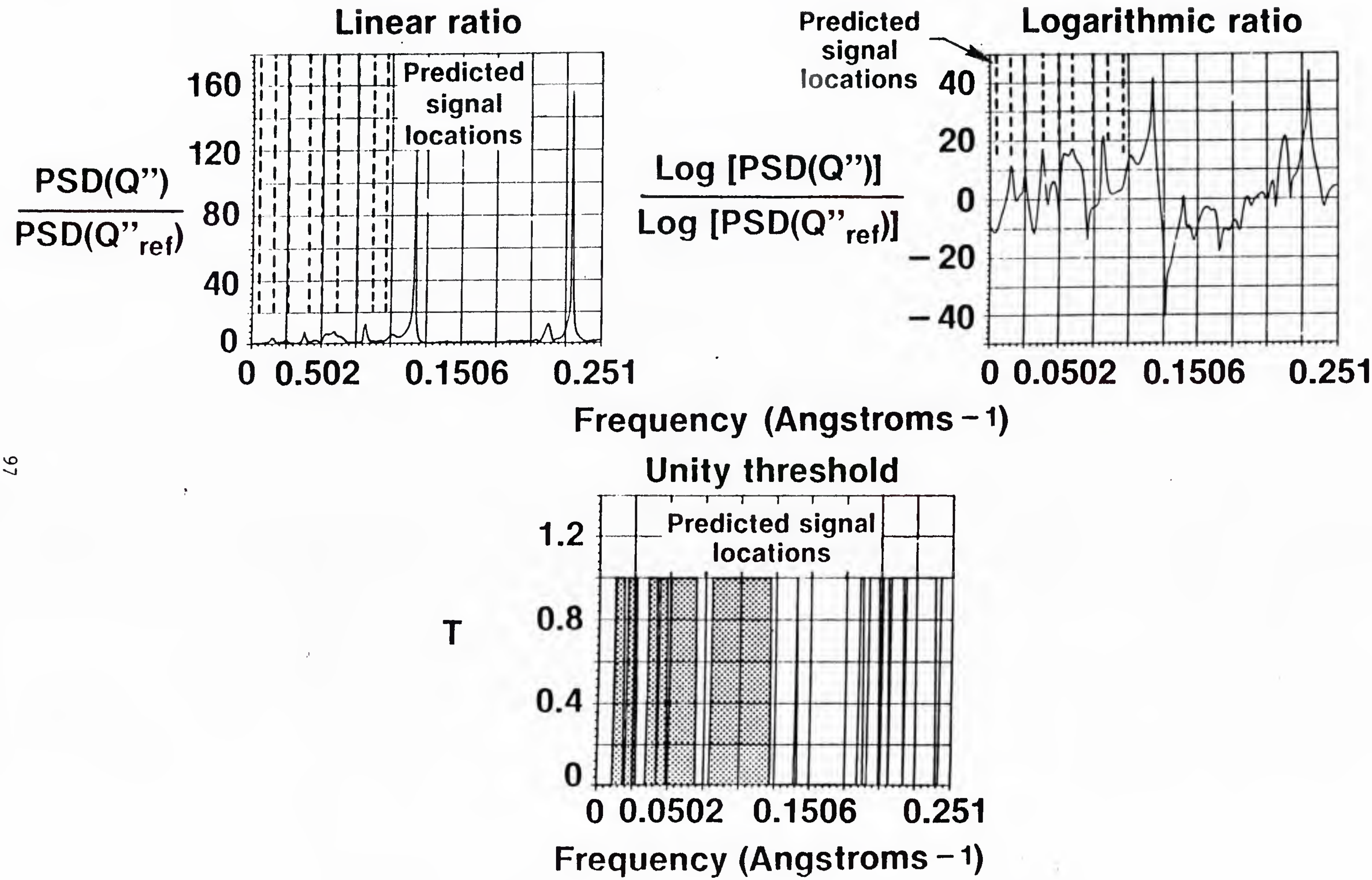

Figure B-19. Serpentine Bend Data (Δ=2 in.; Fig. A-7). Processed

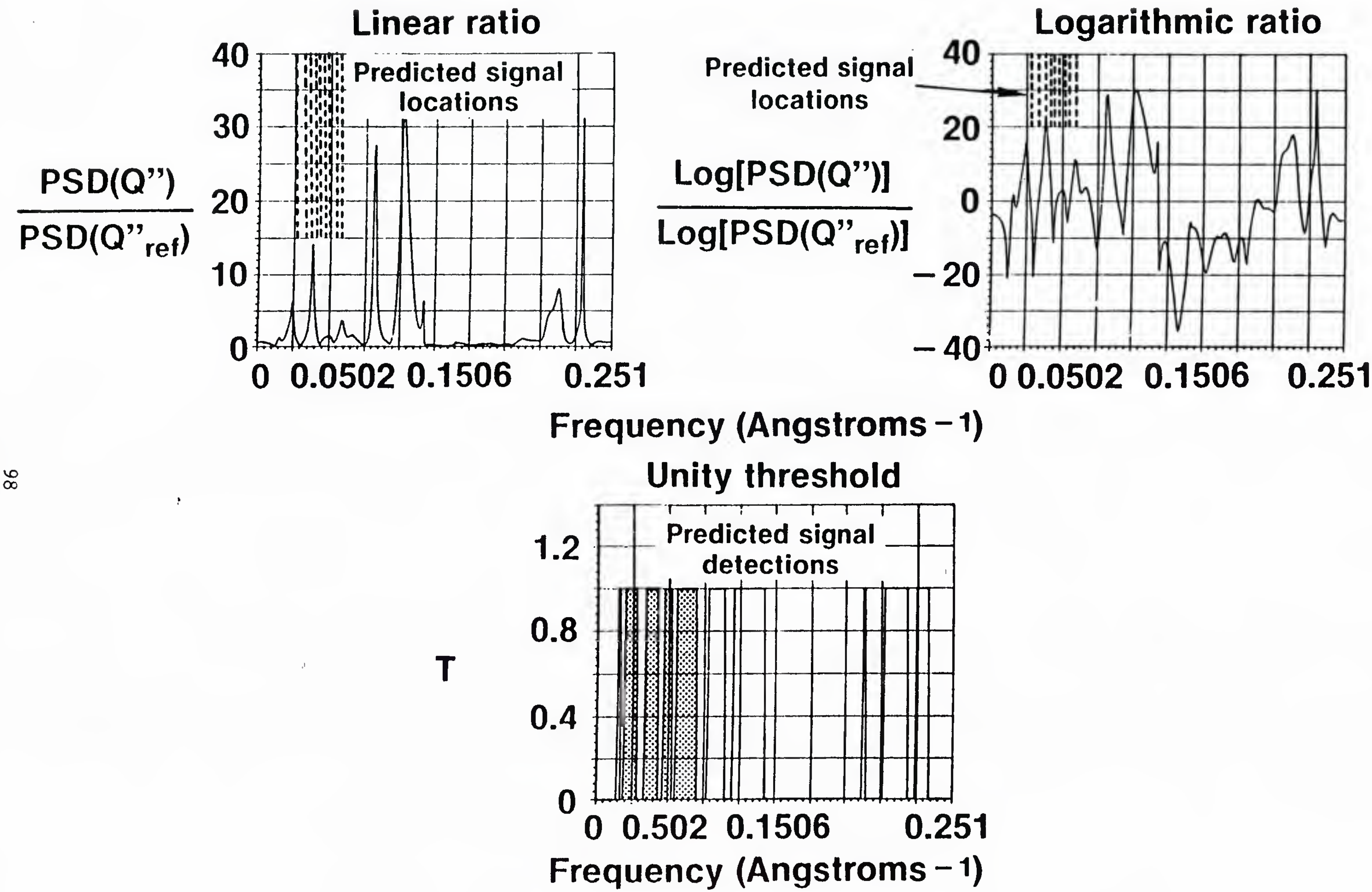

Figure B-20. Serpentine Bend Data (Δ=7 in.; Fig. A-7). Processed

to resolve this condition, sensor calibration data was collected. Such information can have two major effects on the comparison between theory and experiment. The first pertains directly to the interaction of the sensor with bend-type perturbations. When the dye laser is used to provide crosstalk measurements as the wavelength is scanned, it is assumed that we are in effect scanning the twin-core beatlength over a corresponding range. In the earlier calculations the exact beatlengths were predicted for the given wavelength ranges. If the code did not predict the same beatlength exhibited by the laboratory sensor, the resulting crosstalk spectra may not correlate well with that derived from the actual measurements. The theory of Section II suggests significant mismatches could result from such a situation. In previous investigations, good agreement was obtained between predicted and measured beatlengths, but the sensitivity of the current bend-interaction problem with long sensors appears to be more critical. Therefore, a fundamental beatlength documentation was required for use in the model predictions. The second issue concerns the appearance of the predicted spectra. The initial form of the improved model generated the entire spectrum assuming that the beatlength was a linear function of the excitation wavelength. On the other hand, the multiple-peak characteristic of the primary crosstalk signal with the improved measurement parameters seems to suggest a distortion away from a simple linear scan of the crosstalk function. For example, a dispersive effect (beatlength a nonlinear function of wavelength) could account for the new form of this feature. Such a dispersion in the beatlength scanning function would modify every peak in the spectrum. To correct the predicted spectra for this aspect of the sensor, the frequency axis must be transformed by an experimentally derived function before comparison with the laboratory generated spectra. The remainer of this section presents data required to help resolve these issues: dispersion and absolute beatlength.

Two indirect methods and one direct method have been used to diagnose the sensor beatlength. One indirect technique utilizes a measurement of crosstalk as a function of wavelength and then a fitting parameter is inferred from the theory to yield the beatlength. But this specific parameter fitting problem is just the one we are trying to rectify, hence an independent approach is desired. The second indirect method procedes similarly except with measurements of crosstalk as a function of longitudinally applied force (Figure B-21). Again, this data is justified in relation to the theory by a fitting to yield an effective beatlength. But the most direct approach is to observe the sensor output at a fixed wavelength while clipping off small sections. In this manner, the output signal will sweep unambiguously through a beatperiod. No interpretive arguments are necessary to provide the important result. Figure B-22 summarizes just such a measurement sequence for the square-core sensor and indicates an observed beatlength was 6.05 mm (114 μm outside diameter). Similar measurements on a 112 micron O.D. sensor with round cores demonstrated a beatlength of 3.56 mm at 600.8 nm. The new multi-bend sensor model has been adjusted to take this correction into account.

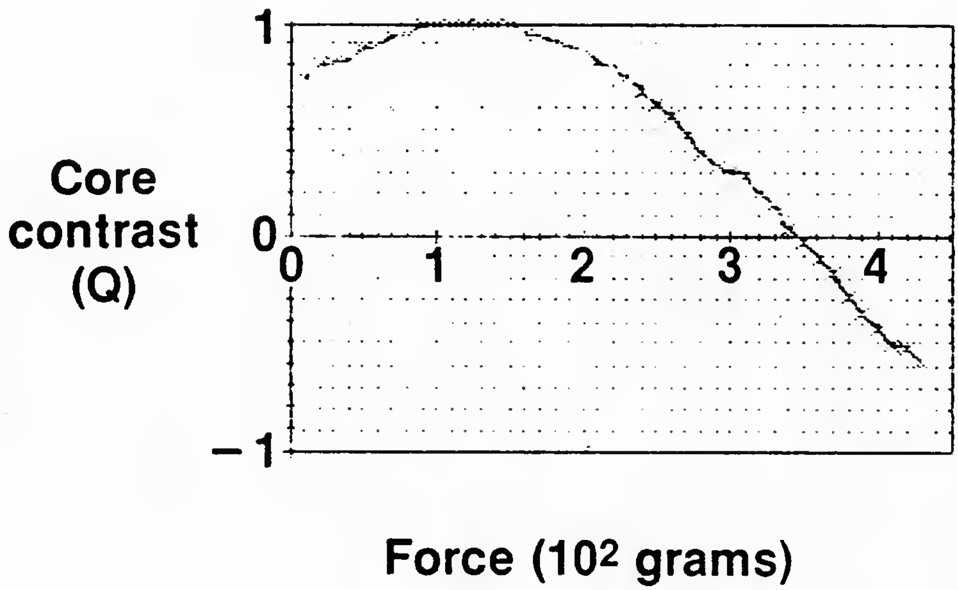

Figure B-21. Sensor Calibration: Force Response. Sample A04.55Q, λ=633 nm, O.D. = 0.0045 inch, L_{ST}=34.204, L_T = 46.3 cm

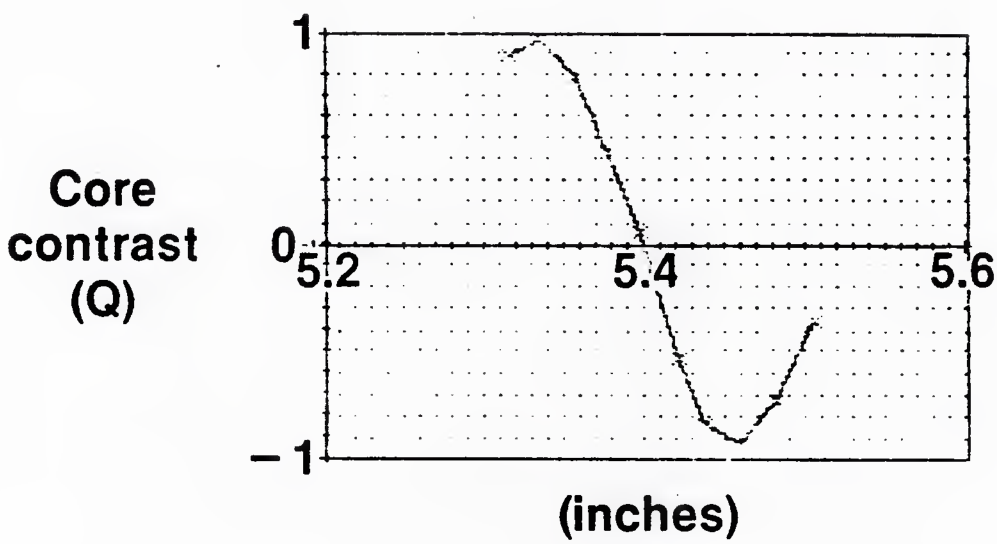

Figure B-22. Sensor Calibration: Length Change Response: Sample A04.55Q, λ=600.8 nm, O.D.=0.0045 inch

Characterizing the dispersion, or nonlinearity, in wavelength dependence of the beatlength requires extensive analysis of the crosstalk data. The nonlinearity is expected to be small but significant to our sensor interpretation so adequate care must be used in the processing. To begin with, crosstalk is measured as a function of wavelength for the sensor in a neutral, straight state (Figure B-23). Two hundred and fifty-six (256) samples were acquired at equal intervals between 600.8 nm and 651.8 nm. This data array provides samples of a more complete function. To create our best guess of this function, we utilize an interpolation technique with a cubic spline fitting routine to provide 12 times as many array elements. Then, the maxima and minima are detected as a function of wavelength change. This yields the curve of Figure B-23, crosstalk phase versus wavelength, which must be diagnosed for nonlinearity. Table B-2 indicates only small deviation from linear, but as evidenced in Section III, this correction significantly modifies the shape of spectral features for long sensors or for broad sample ranges.

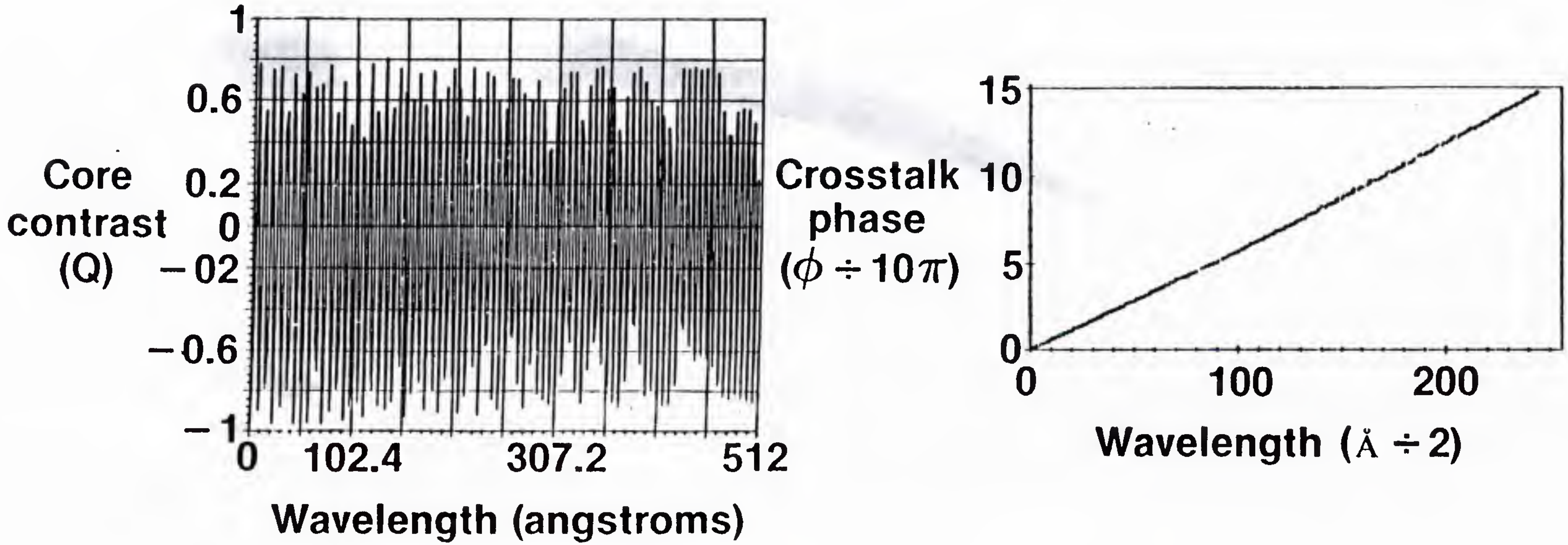

Figure B-23. λ_B vs λ Dispersion: Straight Sensor. Sample A04.55Q, L=35.5 inches

TABLE B-2. EXPERIMENTAL DISPERSION EQUATION

Quadratic Fit Parameters

$Y = A + B x + C x^2$

$A = -3.62 \times 10^{-3}$

$B = 5.47 \times 10^{-2}$

$C = 2.18 \times 10^{-5}$

Coefficient of Determination = 0.999996122

Coefficient of Correlation = 0.999998061

Linear Fit Parameters

$Y = A + Bx$

$A = -2.35 \times 10^{-1}$

$B = 6.01 \times 10^{-2}$

C of D = 0.999473001

C of C = 0.999736466

REFERENCES

1. Synder, A. W. and J. D. Love: Optical Waveguide Theory. Chapman and Hall, New York, p. 392 (1983).

2. Meltz, G., J. R. Dunphy, W. W. Morey and E. Snitzer: Cross-Talk Fiber-Optic Temperature Sensor. Appl. Optics 22: 464 (February 1983).

3. Murakami, Y.: Appl. Optics, 19: 398 (1980).

4. Murakami, Y. and S. Sudo: Coupling Characteristics Measurements Between Curved Waveguide Using a Two-Core Fiber Coupler. Appl. Optics 20: 417 (1981).

5. Keller, H. B. and J. B. Keller: Exponential-Like Solutions of Systems of Liner Ordinary Differential Equations. J. Soc. Induced Appl. Math, 10: 246 (1962).

6. Ganthmacher, F. R.: Theory of Matrices, Vol. 2, Chelsea, New York, pp. 125-141 (1954).

7. Smith, R. B.: Analytical Solutions for Linearly Tapered Directional Couplers. J. Opt. Soc. Am. 66:892 (1976).

8. Chen, Y. S. and A. Ishimaru: Proc. IEEE (Lett.) 54, 1071 (1966).